A Measurement of Direct CP Violation with the NA48 Detector

With special emphasis on
$K^0 \to \pi^+\pi^-$ **decays**

Dissertation
zur Erlangung des Grades
„Doktor der Naturwissenschaften“
am Fachbereich Physik der
Johannes-Gutenberg Universität
in Mainz

Harald Fox
geboren in Lindlar

Mainz 2000

Tag der Prüfung: 11. Mai 2000

Contents

Zusammenfassung

Die Verletzung der CP-Invarianz wurde zuerst in dem Zerfall der schwachen Wechselwirkung $K_\mathrm{L} \rightarrow \pi\pi$ entdeckt. Neben der bekannten indirekten CP-Verletzung, die durch Mischung zwischen K^0 und $\overline{K^0}$ hervorgerufen wird und durch den Parameter ε beschrieben wird, sagt das Standard Modell auch eine direkte CP-Verletzung voraus, die in der Zerfallsamplitude der Kaonen selbst in Erscheinung tritt und durch ε' parametrisiert wird. Es ist das Ziel des Experiments NA48, $\mathcal{R}e(\varepsilon'/\varepsilon)$ mit einer Genauigkeit von $\sim 2 \times 10^{-4}$ zu messen.

Die erste Datennahmeperiode für die Messung von $\mathcal{R}e(\varepsilon'/\varepsilon)$ war 1997, in der 24 TByte an Daten aufgezeichnet wurden. NA48 mißt gleichzeitig die Zerfälle von K_S und K_L in den geladenen Endzustand $\pi^+\pi^-$ und in den neutralen Endzustand $\pi^0\pi^0$. $\mathcal{R}e(\varepsilon'/\varepsilon)$ ergibt sich dabei als:

$$\mathcal{R}e(\varepsilon'/\varepsilon) = \frac{1}{6}\left(1 - \frac{\frac{\Gamma(K_\mathrm{L}\rightarrow\pi^0\pi^0)}{\Gamma(K_\mathrm{S}\rightarrow\pi^0\pi^0)}}{\frac{\Gamma(K_\mathrm{L}\rightarrow\pi^+\pi^-)}{\Gamma(K_\mathrm{S}\rightarrow\pi^+\pi^-)}}\right) .$$

Das Experiment und die Analyse sind so gestaltet, daß sich systematische Effekte im Doppelverhältnis prinzipiell aufheben. Die Bestimmung von unvermeidlichen systematischen Abweichungen nimmt einen Hauptteil der Dissertation ein. Das gemessene Doppelverhältnis wird auf eine Mißidentifizierung von K_S und K_L, auf die Triggerineffizienz, auf verbleibenden Untergrund, auf zufällige Aktivität im Detektor, und auf Akzeptanzunterschiede zwischen den Zerfallsarten hin korrigiert.

Das Ergebnis der hier vorgestellten Analyse ist:

$$\mathcal{R}e(\varepsilon'/\varepsilon) \ = (18.3 \pm \ 4.6(\mathrm{stat}) \ \pm \ 5.8(\mathrm{sys})) \times 10^{-4} \ .$$

Der statistische Fehler wird durch die Anzahl der $K_\mathrm{L} \rightarrow \pi^0\pi^0$ Zerfälle dominiert. Inzwischen liegt die 7-fache Datenmenge aus den Datennahmeperioden 1998 und 1999 vor.

Kombiniert man diese Messung mit früheren Messungen, so ergibt sich ein neuer Mittelwert von $(21.2 \pm 4.7) \times 10^{-4}$. Damit ist die Existenz direkter CP-Verletzung bestätigt.

1 Introduction

Symmetries play a very important role in physics. They govern the most basic physical laws that we know: conservation laws and the interactions of particles in quantum field theory. Conservation laws are intimately related to symmetries via Noether's theorem. The homogeneity of space and time, reflected by the invariance of physical laws under translations in space and time, has the conservation of momentum and energy as consequence. In the same way the invariance under rotation is linked to the conservation of angular momentum. In quantum field theory the invariance under a global phase shift of the particle fields $\Psi(x)$ (global gauge invariance)

$$\Psi(x) \to \mathrm{e}^{ig\Phi} \cdot \Psi(x),$$

implies the conservation of charge.

In order to make a field theory invariant under local gauge transformations

$$\Psi(x) \to \mathrm{e}^{ig\Phi(x)} \cdot \Psi(x),$$

where the phase shift $\Phi(x)$ is now dependent on the position x, the usual derivative has to be replaced (minimal coupling):

$$\partial_\mu \to \partial_\mu - igA_\mu.$$

This theory describes the interaction of fields $\Psi(x)$ via the gauge field A_μ, which means via the exchange of mediating bosons, which transfer momentum.

	electro-magnetic	weak	strong	gravity
boson	photon	$W^\pm$, Z^0	8 gluons	graviton
spin	1	1	1	2
mass	0	80.4 GeV, 91.19 GeV	0	0

Table 1: The bosons of the Standard Model and of gravity. The hypothetical graviton is the supposed quantum of the gravitational field.

The Standard Model (SM) of the electro-magnetic, weak, and strong interactions imposes different local gauge symmetries on the Lagrange density. The Lagrange density satisfies symmetry relations given by the gauge group

$$\mathrm{SU}(3)_c \times \mathrm{SU}(2)_L \times \mathrm{U}(1)_Y.$$

The $SU(3)_c$ gauge invariance describes gluons, the gauge field of the strong interaction. The electro-weak interaction is described by the $SU(2)_L \times U(1)_Y$ gauge invariance, leading to a unified description of the weak and electromagnetic interactions. These gauge fields (see Table 1) interact with the fermions of the theory, which are grouped in 3 generations, as shown in Table 2.

charge			
0	ν_e	ν_μ	ν_τ
-1	e^-	μ^-	τ^-
$+2/3$	u	c	t
$-1/3$	d	s	b

Table 2: The fermions of the Standard Model. For each particle a corresponding antiparticle exists.

The fourth known force, gravity, is also described by symmetry principles. The laws of motion are invariant under Lorentz transformations. The General Theory of Relativity can be expressed in the formalism of a gauge theory. The Lorentz transformations $\Lambda^\mu{}_\nu(x)$ are equivalent to gauge transformations, which act on a vector V^μ:

$$V^\mu(x) \to \Lambda^\mu{}_\nu(x) V^\nu(x).$$

The invariance is ensured by introducing the covariant derivative of vector V:

$$V^\mu_{;\nu} = \partial_\nu V^\mu + \Gamma^\mu{}_{\alpha\nu} V^\alpha.$$

The Christoffel symbols $\Gamma^\mu{}_{\alpha\nu}$ are thus the equivalent of the gauge fields A_μ of a usual gauge theory.

In addition to the continuous symmetries described above, also discrete symmetries play an important role in field theory. In field theories the most important discrete transformations are:

C	Charge conjugation	Particles are exchanged with antiparticles and vice versa.
P	Parity	The coordinate system is reversed, a vector $\vec{r}$ becomes $-\vec{r}$.
T	Time reversal	The direction of time is reversed.

Lüders and Pauli [Lüd57, Pau55] have shown that any relativistic local field theory must be invariant under the combined operation CPT. However, this is not necessarily the case for a single operator C, P, or T. While the electro-magnetic and the strong interaction are invariant under all 3 transformations, the weak interaction violates P, as suggested by Lee and Yang [LY56] and shown by Wu and collaborators [WAH+57]. The weak interaction also violates C invariance. Christenson, Cronin, Fitch and Turlay [CCFT64] have shown that the combined transformation CP is aswell violated by the weak interaction. Given that the CPT theorem holds, CP violation implies that also T symmetry is broken.

CP violation is important in order to explain the observed baryon asymmetry of the universe. Why is there an obvious preference of matter over antimatter? Sakharov found 3 conditions for the baryon asymmetry to occur [Sak67]:

- Baryon number violation (*e.g.* proton decay)
- Departure from thermal equilibrium
- CP violation

The study of CP violation and its explanation by a theoretical model is therefore linked to the baryogenesis in the early universe.

The Standard Model contains CP violation in the Yukawa interactions, manifest by a phase in the quark mixing matrix (CKM-matrix). It predicts two different kind of CP violation in the neutral kaon system (see Section 2.2): indirect CP violation, caused by $K^0 - \overline{K^0}$ mixing and parameterized by ε, and direct CP violation, occuring in the K^0 decay and parameterized by ε'. An alternative model, the Superweak Model [Wol64], predicts that direct CP violation does not exist ($\varepsilon' = 0$).

Due to the smallness of ε'/ε experimental measurements are challenging. The first evidence for direct CP violation was found by the NA31 experiment in 1988 with $\mathcal{R}e(\varepsilon'/\varepsilon) = (33 \pm 11) \times 10^{-4}$ [B+88]. In 1992/93 the experiments NA31 at CERN and E731 at FNAL presented final results. The CERN result [B+93] of $\mathcal{R}e(\varepsilon'/\varepsilon) = (23.0 \pm 6.5) \times 10^{-4}$ is more than 3 standard deviations above zero and thus shows clear evidence for direct CP violation, while the

Fermilab result [G+93] of $\mathcal{R}e(\varepsilon'/\varepsilon) = (7.4 \pm 5.9) \times 10^{-4}$ is consistent with zero. This situation has been clarified only at the beginning of 1999, when two new experiments announced their first results. KTeV at FNAL measures $\mathcal{R}e(\varepsilon'/\varepsilon) = (28.0 \pm 4.1) \times 10^{-4}$ [AH+99], while NA48 at CERN measures $\mathcal{R}e(\varepsilon'/\varepsilon) = (18.5 \pm 7.3) \times 10^{-4}$ [F+99]. Now there is general agreement that $\mathcal{R}e(\varepsilon'/\varepsilon)$ is above zero and direct CP violation exists.

Since 1996 I have been a member of the NA48 collaboration. My first involvement consisted of designing and writing the major part of the Level 3/ Real Time Reconstruction software. I was responsible for the online data processing during the running periods in 1997 and 1998. I was also responsible for the re-processing of the 1997 data after the final calibration of the detector.

This work is one of the analyses of $\mathcal{R}e(\varepsilon'/\varepsilon)$ on which the published result is based. My involvement was concentrated on analyzing the charged decay mode. I have been mainly concerned with event selection, determination of the charged trigger efficiency and optimization of the event tagging. I also carried out a large number of systematic checks of the result.

The final result of this measurement is:

$$\mathcal{R}e(\varepsilon'/\varepsilon) \ = \ (18.3 \ \pm \ 4.6 \ (\mathrm{stat}) \ \pm \ 5.8 \ (\mathrm{sys})) \times 10^{-4} \ . \tag{1.1}$$

2 Theory

2.1 CP Violation in the Standard Model

Quarks, as eigenstates of the strong interaction, are not simultaneously the eigenstates of the weak interaction. The two bases are related by the unitary Cabibbo-Kobayashi-Maskawa matrix V_{CKM} [KM73, GKR99]:

$$\begin{pmatrix} d' \\ s' \\ b' \end{pmatrix} = V_{\mathrm{CKM}} \begin{pmatrix} d \\ s \\ b \end{pmatrix} = \begin{pmatrix} V_{ud} & V_{us} & V_{ub} \\ V_{cd} & V_{cs} & V_{cb} \\ V_{td} & V_{ts} & V_{tb} \end{pmatrix} \begin{pmatrix} d \\ s \\ b \end{pmatrix}. \tag{2.1}$$

A unitary $(n \times n)$ matrix has n^2 free parameters, of which $2n - 1$ can be absorbed in the quark fields. For the case of the SM, with $n = 3$, this leaves 4 parameters: 3 mixing angles and 1 phase. As a consequence of this phase, the weak interaction is not invariant under CP transformation.

V_{CKM} can be approximated as [Wol83]:

$$V_{\mathrm{CKM}} \approx \begin{pmatrix} 1 - \frac{1}{2}\lambda^2 & \lambda & A\lambda^3[\rho - i\eta] \\ -\lambda & 1 - \frac{1}{2}\lambda^2 & A\lambda^2 \\ A\lambda^3[1 - \rho - i\eta] & -A\lambda^2 & 1 \end{pmatrix}, \tag{2.2}$$

where $\lambda = 0.22$ refers to the sine of the Cabibbo angle. Of the 6 off-diagonal equations that follow from the unitarity of V_{CKM}, the most widely referred to is:

$$V_{ud}V_{ub}^* + V_{cd}V_{cb}^* + V_{td}V_{tb}^* = 0. \tag{2.3}$$

This equation can be interpreted geometrically as a triangle, the so-called unitarity triangle. The triangle and its experimental constraints are shown in Figure 1. If the triangle is rescaled with $|\lambda V_{cb}|^{-1}$, so that the base is of unit length, the point A corresponds to $A = (\rho, \eta)$ in the Wolfenstein approximation (equation (2.2)), where η is the CP violating phase. The area of the triangle is a measure of the amount of CP violation in the Standard Model.

2.2 Kaon Phenomenology

As the weak interaction violates strangeness S, the eigenstates $|K^0\rangle$ and $|\overline{K^0}\rangle$ of the strong interaction may mix. We can define CP eigenstates as

$$|K_1\rangle = \frac{1}{\sqrt{2}}(|K^0\rangle + |\overline{K^0}\rangle) \qquad \mathrm{CP} = +1, \tag{2.4}$$

$$|K_2\rangle = \frac{1}{\sqrt{2}}(|K^0\rangle - |\overline{K^0}\rangle) \qquad \mathrm{CP} = -1. \tag{2.5}$$

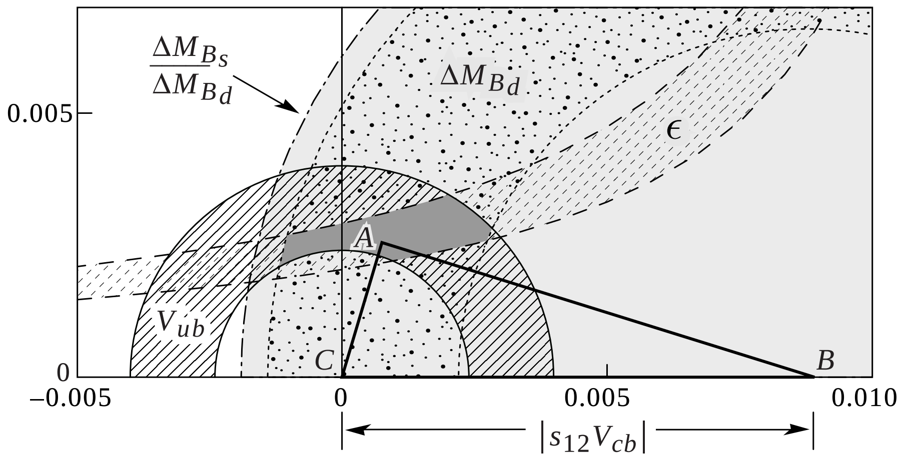

Figure 1: Graphical illustration of the unitarity relation (2.3) with experimental constraints [GKR99]. Here $s_{12} = \lambda$ is used.

As the $\pi^+\pi^-$ and $\pi^0\pi^0$ final states coming from K^0 decays have a CP eigenvalue of $+1$, the decay $\mathrm{K}_2 \rightarrow \pi\pi$ is forbidden if CP symmetry holds.

Due to the CP violating phase in second order weak transitions with $\Delta S = 2$ (box diagrams Figure 2(a)) the physical eigenstates with defined mass and lifetime differ from the CP eigenstates:

$$|K_{\mathrm{S}}\rangle = \frac{1}{\sqrt{1+|\bar{\varepsilon}|^2}}\left(|K_1\rangle + \bar{\varepsilon}\,|K_2\rangle\right), \tag{2.6}$$

$$|K_{\mathrm{L}}\rangle = \frac{1}{\sqrt{1+|\bar{\varepsilon}|^2}}\left(|K_2\rangle + \bar{\varepsilon}\,|K_1\rangle\right). \tag{2.7}$$

In the $|K^0\rangle$ -$|\overline{K^0}\rangle$ basis we find, with $N_K = \sqrt{2(1+|\bar{\varepsilon}|^2)}$:

$$|K_{\mathrm{S}}\rangle = \frac{1}{N_K}[(1+\bar{\varepsilon})|K^0\rangle + (1-\bar{\varepsilon})|\overline{K^0}\rangle], \tag{2.8}$$

$$|K_{\mathrm{L}}\rangle = \frac{1}{N_K}[(1+\bar{\varepsilon})|K^0\rangle - (1-\bar{\varepsilon})|\overline{K^0}\rangle]. \tag{2.9}$$

The states $|K_{\mathrm{S}}\rangle$ and $|K_{\mathrm{L}}\rangle$ are the eigenstates of the equation of motion for a wave function $\Phi(t) = a_K(t)|K^0\rangle + a_{\bar{K}}(t)|\overline{K^0}\rangle$

$$i\frac{\mathrm{d}\Phi(t)}{\mathrm{d}t} = H\Phi(t) = (M - \frac{i}{2}\Gamma)\Phi(t), \tag{2.10}$$

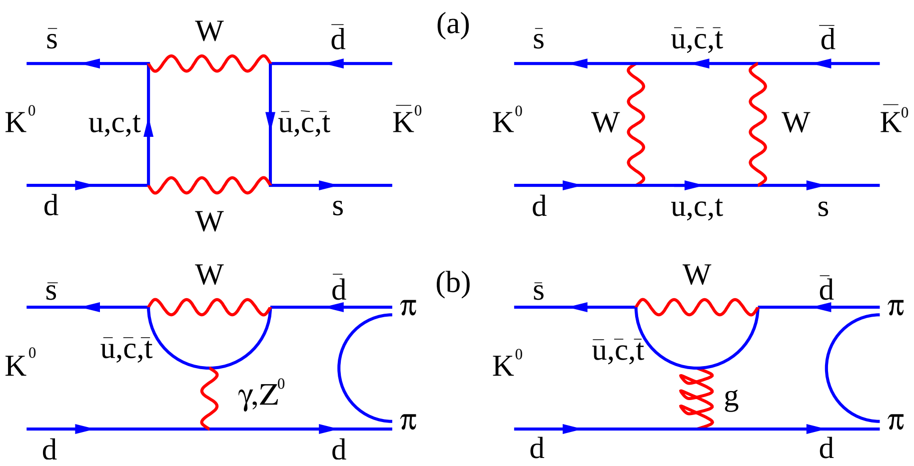

Figure 2: (a) Box diagrams illustrating the $\Delta\mathbf{S} = 2$ mixing between $K^0 \leftrightarrow \overline{K^0}$. (b) Electroweak and gluonic penguin diagrams with $\Delta\mathbf{S} = 1$, which dominate ε'.

where, using the CPT theorem and hermiticity,

$$M = \begin{pmatrix} M_0 & M_{12} \\ M_{12}^* & M_0 \end{pmatrix}, \qquad \Gamma = \begin{pmatrix} \Gamma_0 & \Gamma_{12} \\ \Gamma_{12}^* & \Gamma_0 \end{pmatrix}. \tag{2.11}$$

The value of $\bar{\varepsilon}$ is related to the matrix H via

$$\frac{1-\bar{\varepsilon}}{1+\bar{\varepsilon}} = \frac{M_{12}^* - i/2\Gamma_{12}^*}{(\Delta M + i/2\Delta\Gamma)/2}, \tag{2.12}$$

where ΔM and $\Delta\Gamma$ are the differences of the masses and widths of the eigenvalues

$$\Delta M = M_S - M_L, \qquad \Delta\Gamma = \Gamma_S - \Gamma_L. \tag{2.13}$$

The contribution of $\bar{\varepsilon}\,|K_2\rangle$ to $|K_{\mathrm{S}}\rangle$ and $\bar{\varepsilon}\,|K_1\rangle$ to $|K_{\mathrm{L}}\rangle$ via mixing (matrix elements M_{12} and Γ_{12}) is called *indirect CP violation*. The decay of a K_2 or K_1 into a final state of opposite CP via a weak $\Delta S = 1$ transition (penguin diagrams Figure 2(b)) is called *direct CP violation* in the decay.

Due to the strong interaction between the final state pions additional phases are acquired. The magnitudes of these phases depend on the isospin I of the final state. In order to relate CP violation to measurable quantities, we thus have to separate the decays into final states with $I = 0$ and $I = 2$. For further discussions we restrict ourselves to final states with two pions. A pion is a boson with isospin $I = 1$, $I_3 = +1, 0, -1$ for π^+, π^0, π^-.

The Clebsch-Gordan coefficients [PDG98] for a $\pi\pi$ final state with isospin $|I\ I_3\rangle$ are given in Table 3.

final state $\|I\ I_3\rangle$	π_1 $\|I\ I_3\rangle$	π_2 $\|I\ I_3\rangle$	Clebsch-Gordan coefficient	
	$\|1\ 1\rangle$	$\|1\ {-1}\rangle$	$\sqrt{1/3}$	$\pi^+\pi^-$
$\|0\ 0\rangle$	$\|1\ 0\rangle$	$\|1\ 0\rangle$	$-\sqrt{1/3}$	$\pi^0\pi^0$
	$\|1\ {-1}\rangle$	$\|1\ 1\rangle$	$\sqrt{1/3}$	$\pi^-\pi^+$
	$\|1\ 1\rangle$	$\|1\ {-1}\rangle$	$\sqrt{1/6}$	$\pi^+\pi^-$
$\|2\ 0\rangle$	$\|1\ 0\rangle$	$\|1\ 0\rangle$	$\sqrt{2/3}$	$\pi^0\pi^0$
	$\|1\ {-1}\rangle$	$\|1\ 1\rangle$	$\sqrt{1/6}$	$\pi^-\pi^+$
	$\|1\ 1\rangle$	$\|1\ {-1}\rangle$	$\sqrt{1/2}$	$\pi^+\pi^-$
$\|1\ 0\rangle$	$\|1\ 0\rangle$	$\|1\ 0\rangle$	0	$\pi^0\pi^0$
	$\|1\ {-1}\rangle$	$\|1\ 1\rangle$	$-\sqrt{1/2}$	$\pi^-\pi^+$

Table 3: Clebsch-Gordan coefficients for a composition of two $|I\ I_3\rangle$ states with $I = 1$ and $I_3 = +1, 0, -1$ [PDG98, Kle76].

The Clebsch-Gordan coefficients for the final state $|1\ 0\rangle$ sum up to 0, which reflects the fact that this state is forbidden by Bose symmetry. Therefore the contributions of $I = 0, 2$ to the charged and neutral final state are:

$$|\pi^+\pi^-\rangle = \sqrt{\tfrac{2}{3}}|(\pi\pi)_{I=0}\rangle + \sqrt{\tfrac{1}{3}}|(\pi\pi)_{I=2}\rangle, \tag{2.14}$$

$$|\pi^0\pi^0\rangle = -\sqrt{\tfrac{1}{3}}|(\pi\pi)_{I=0}\rangle + \sqrt{\tfrac{2}{3}}|(\pi\pi)_{I=2}\rangle. \tag{2.15}$$

We can write the decay amplitudes into isospin $I = 0, 2$ final states as:

$$\langle(\pi\pi)_{I=0}|H|K^0\rangle = A_0 \mathrm{e}^{i\delta_0}, \qquad \langle(\pi\pi)_{I=0}|H|\overline{K^0}\rangle = A_0^* \mathrm{e}^{i\delta_0}, \qquad \Delta I = 1/2, \tag{2.16}$$

$$\langle(\pi\pi)_{I=2}|H|K^0\rangle = A_2 \mathrm{e}^{i\delta_2}, \qquad \langle(\pi\pi)_{I=2}|H|\overline{K^0}\rangle = A_2^* \mathrm{e}^{i\delta_2}, \qquad \Delta I = 3/2. \tag{2.17}$$

Here the strong phases $\delta_{0,2}$ are factored out explicitly so that the phases of the amplitudes $A_{0,2}$ are purely weak. Note that the strong phases do not change sign when going from K^0 to $\overline{K^0}$, whereas the weak phases do.

Now we can express the decay amplitudes A_{+-} and A_{00} of the physical states $K_{\mathrm{S,L}}$ into two pions in terms of isospin:

$$\begin{aligned}
A_{+-\,;\mathrm{S,L}} &\equiv \langle\pi^+\pi^-|H|K_{\mathrm{S,L}}\rangle \\
&= \sqrt{\frac{2}{3}}\langle(\pi^+\pi^-)_{I=0}|H|K_{\mathrm{S,L}}\rangle + \sqrt{\frac{1}{3}}\langle(\pi^+\pi^-)_{I=2}|H|K_{\mathrm{S,L}}\rangle, \qquad (2.18)\\
A_{00\,;\mathrm{S,L}} &\equiv \langle\pi^+\pi^-|H|K_{\mathrm{S,L}}\rangle \\
&= -\sqrt{\frac{1}{3}}\langle(\pi^0\pi^0)_{I=0}|H|K_{\mathrm{S,L}}\rangle + \sqrt{\frac{2}{3}}\langle(\pi^0\pi^0)_{I=2}|H|K_{\mathrm{S,L}}\rangle. \qquad (2.19)
\end{aligned}$$

Using equations (2.8) and (2.9) one obtains:

$$\begin{aligned}
A_{+-\,;\mathrm{S}} &= \frac{1}{N_K\sqrt{3}}\Big[\sqrt{2}(1+\bar{\varepsilon})A_0\mathrm{e}^{i\delta_0} + \sqrt{2}(1-\bar{\varepsilon})A_0^*\mathrm{e}^{i\delta_0} + \\
&\quad (1+\bar{\varepsilon})A_2\mathrm{e}^{i\delta_2} + (1-\bar{\varepsilon})A_2^*\mathrm{e}^{i\delta_2}\Big] \\
&= \frac{1}{N_K\sqrt{3}}\Big[\sqrt{2}\mathrm{e}^{i\delta_0}(\mathcal{R}eA_0 + i\bar{\varepsilon}\,\mathcal{I}mA_0) + \mathrm{e}^{i\delta_2}(\mathcal{R}eA_2 + i\bar{\varepsilon}\,\mathcal{I}mA_2)\Big].
\end{aligned}$$

Therefore we can write the measurable quantities $\eta_{+-} = \frac{\langle\pi^+\pi^-|H|K_{\mathrm{L}}\rangle}{\langle\pi^+\pi^-|H|K_{\mathrm{S}}\rangle}$ and $\eta_{00} = \frac{\langle\pi^0\pi^0|H|K_{\mathrm{L}}\rangle}{\langle\pi^0\pi^0|H|K_{\mathrm{S}}\rangle}$ as follows:

$$\begin{aligned}
\eta_{+-} &= \frac{\sqrt{2}\mathrm{e}^{i\delta_0}(\bar{\varepsilon}\,\mathcal{R}eA_0 + i\,\mathcal{I}mA_0) - \mathrm{e}^{i\delta_2}(\bar{\varepsilon}\,\mathcal{R}eA_2 + i\,\mathcal{I}mA_2)}{\sqrt{2}\mathrm{e}^{i\delta_0}(\mathcal{R}eA_0 + i\bar{\varepsilon}\mathcal{I}mA_0) + \mathrm{e}^{i\delta_2}(\mathcal{R}eA_2 + i\bar{\varepsilon}\mathcal{I}mA_2)}, \qquad (2.20)\\
\eta_{00} &= \frac{-\mathrm{e}^{i\delta_0}(\bar{\varepsilon}\mathcal{R}eA_0 + i\,\mathcal{I}mA_0) + \sqrt{2}\mathrm{e}^{i\delta_2}(\bar{\varepsilon}\,\mathcal{R}eA_2 + i\,\mathcal{I}mA_2)}{-\mathrm{e}^{i\delta_0}(\mathcal{R}eA_0 + i\bar{\varepsilon}\mathcal{I}mA_0) - \sqrt{2}\mathrm{e}^{i\delta_2}(\mathcal{R}eA_2 + i\bar{\varepsilon}\mathcal{I}mA_2)}. \qquad (2.21)
\end{aligned}$$

We can now define ε, ε' and ω as

$$\begin{aligned}
\varepsilon &= \frac{\bar{\varepsilon}\mathcal{R}eA_0 + i\,\mathcal{I}mA_0}{\mathcal{R}eA_0 + i\bar{\varepsilon}\mathcal{I}mA_0} \approx \bar{\varepsilon} + i\,\frac{\mathcal{I}mA_0}{\mathcal{R}eA_0}, \qquad (2.22)\\
\varepsilon' &= \frac{1}{\sqrt{2}}\frac{\mathcal{R}eA_2}{\mathcal{R}eA_0}\left(\frac{\mathcal{I}mA_2}{\mathcal{R}eA_2} - \frac{\mathcal{I}mA_0}{\mathcal{R}eA_0}\right)\mathrm{e}^{i(\delta_2-\delta_0)}, \qquad (2.23)\\
\omega &= \frac{\mathcal{R}eA_2}{\mathcal{R}eA_0}\mathrm{e}^{i(\delta_2-\delta_0)}. \qquad (2.24)
\end{aligned}$$

ε and ε' are chosen in a way that they reflect the contribution of indirect and direct CP violation. We can choose a phase convention (Wu-Yang phase convention) such that $\mathcal{I}mA_0 = 0$. Then we see from equation (2.22) that $\varepsilon = \bar{\varepsilon}$ which is the mixing parameter from equations (2.6) and (2.7). ε has no contribution from the amplitude A_2 and therefore no phase interference. ε measures the amount of indirect CP violation. On the other hand ε' measures the amount of direct CP violation in $\Delta S = 1$ transitions (that is directly in the decay amplitude of the Kaon). It depends on the phase difference in the decay amplitudes A_2 and A_0. If the phases are identical, ε' vanishes. Incidentally ε and ε' have numerically about the same phase.

Experimentally $|\omega|$ is measured to be 1/22: $\Delta I = 3/2$ transitions are strongly suppressed. This is the so-called $\Delta I = 1/2$ rule. Using the relations (2.22)-(2.24), we can express equations (2.20) and (2.21) as:

$$\eta_{+-} = \varepsilon + \frac{\varepsilon'}{1 + 1/\sqrt{2}\omega} \approx \varepsilon + \varepsilon', \tag{2.25}$$

$$\eta_{00} = \varepsilon - \frac{2\varepsilon'}{1 - \sqrt{2}\omega} \approx \varepsilon - 2\varepsilon'. \tag{2.26}$$

From this we can see that (using $\varepsilon' \ll \varepsilon$)

$$R \equiv \left|\frac{\eta_{00}}{\eta_{+-}}\right|^2 \approx 1 - 6\mathcal{R}e(\varepsilon'/\varepsilon). \tag{2.27}$$

Thus the measurement of the double ratio

$$R = \frac{\frac{\Gamma(K_\mathrm{L} \to \pi^0\pi^0)}{\Gamma(K_\mathrm{S} \to \pi^0\pi^0)}}{\frac{\Gamma(K_\mathrm{L} \to \pi^+\pi^-)}{\Gamma(K_\mathrm{S} \to \pi^+\pi^-)}} \tag{2.28}$$

gives access to the relative magnitude of direct CP violation.

Reviews and introductory articles about CP violation can be found in [Mas94, Ber97a, Cha83, Kle89, Buc97, Nie99, WW93].

2.3 Standard Model Predictions of ε'/ε

Various methods exist to calculate the value of $\mathcal{R}e(\varepsilon'/\varepsilon)$. Due to the difficulties in calculating hadronic matrix elements, which involve long distance effects, this task turns out to be very difficult. Several non-perturbative approaches are used to solve the problem. Summaries of the various results can be found in [Bur99, BFE98]. The following results have been obtained recently:

1. The Dortmund group uses the $1/N_C$ expansion and Chiral Perturbation Theory (χPT). They quote a range of $1.5 \times 10^{-4} < \varepsilon'/\varepsilon < 31.6 \times 10^{-4}$ [HKPS99] from scanning the complete range of input parameters.

2. The Munich group uses a phenomenological approach in which as many parameters as possible are taken from experiment. Their result [BBG$^+$99]

is $1.5 \times 10^{-4} < \varepsilon'/\varepsilon < 28.8 \times 10^{-4}$ from a scanning of the input parameters, and $\varepsilon'/\varepsilon = (7.7^{+6.0}_{-3.5}) \times 10^{-4}$ using a Monte Carlo method to determine the error.

3. The Rome group uses lattice calculation results for the input parameters. Their result is $\varepsilon'/\varepsilon = (4.7^{+6.7}_{-5.9}) \times 10^{-4}$ [Mar99].
4. The Trieste group uses a chiral quark model to calculate ε'/ε. Their result is $7 \times 10^{-4} < \varepsilon'/\varepsilon < 31 \times 10^{-4}$ [BFE98] from scanning.

The scanning method assumes a flat probability within $\pm 1\sigma$ of the theoretical input parameters. It hides the fact that high values of ε'/ε are less probable as all input parameters have to match perfectly.

In general theoretical predictions are lower than the combined experimental result (see Figure 65 on page 110). However, given the difficulties in the calculation, already the agreement in the sign and the order of magnitude is regarded as a success [Bur99]. The theoretical values are within the reach of the experimental results when all input parameters are pushed to the extreme of the allowed limit. But this conspiracy of parameters is seen as unnatural.

3 Principle of the Measurement

The NA48 experiment measures the four decay modes $K_{\rm S,L} \to \pi^0\pi^0$ and $K_{\rm S,L} \to \pi^+\pi^-$ as given in equation (2.28). The limiting mode is $K_{\rm L} \to \pi^0\pi^0 \to 4\gamma$ for two reasons. On one hand these $K_{\rm L}$ decays are suppressed due to indirect CP violation by a factor of 2.3×10^{-3}. On the other hand the neutral final state consists of four particles, leading to a smaller detector acceptance with respect to the $\pi^+\pi^-$ final state. To reach a statistical precision of a few 10^{-4} on $\mathcal{R}e(\varepsilon'/\varepsilon)$, about $4-5\times 10^6$ $K_{\rm L} \to \pi^0\pi^0$ decays have to be collected. First results with this accuracy are envisaged in a few years.

In order to minimize systematic effects, all four decay modes are measured simultaneously. The quantities actually measured are the number of decays $N_{\rm S,L}^{+-,00}$ with $N = \Gamma \cdot \Phi \cdot a \cdot \epsilon$, where Γ is the branching ratio, Φ denotes the flux of $K_{\rm S,L}$, a is the detector acceptance, and ϵ is the trigger efficiency.

To first order trigger efficiencies are identical for $K_{\rm S}$ and $K_{\rm L}$ decays ($\epsilon_L = \epsilon_S$). We also may assume $a_S = a_L$ to a very good approximation, if the fiducial volume and the detector are identical for $K_{\rm S}$ and $K_{\rm L}$ decays. A priori this is not true, as the vertex distributions are different for $K_{\rm S}$ and $K_{\rm L}$ decays due to their different lifetimes. For this reason $K_{\rm L}$ events are weighted such that the vertex distribution equals that $K_{\rm S}$ decays. This results in a loss of statistical power, but a better control of the systematic uncertainty is gained.

If the equalities above hold, we can relate equation (2.28) to the measured quantities N by expanding the equation with terms $a_{\rm L}^{00}/a_{\rm S}^{00}$, $\epsilon_{\rm L}^{00}/\epsilon_{\rm S}^{00}$ (and their charged equivalents):

$$R = \frac{\frac{\Gamma_{\rm L}^{00}}{\Gamma_{\rm S}^{00}}}{\frac{\Gamma_{\rm L}^{+-}}{\Gamma_{\rm S}^{+-}}} = \frac{\frac{\Gamma_{\rm L}^{00}\Phi_{\rm L}a_{\rm L}^{00}\epsilon_{\rm L}^{00}}{\Gamma_{\rm S}^{00}\Phi_{\rm S}a_{\rm S}^{00}\epsilon_{\rm S}^{00}}}{\frac{\Gamma_{\rm L}^{+-}\Phi_{\rm L}a_{\rm L}^{+-}\epsilon_{\rm L}^{+-}}{\Gamma_{\rm S}^{+-}\Phi_{\rm S}a_{\rm S}^{+-}\epsilon_{\rm S}^{+-}}} = \frac{\frac{N_{\rm L}^{00}}{N_{\rm S}^{00}}}{\frac{N_{\rm L}^{+-}}{N_{\rm S}^{+-}}} \tag{3.1}$$

Small deviations from the equalities stated above lead to corrections which have to be applied to the measured raw value of R. These are the main sources of systematic errors.

The analysis is performed in energy bins. Differences in the variation of the energy spectrum between $K_{\rm S}$, $K_{\rm L}$, and simulated Monte Carlo decays can be neglected, as long as the acceptance variation within the energy bins is sufficiently small. A bin size of 5 GeV has been chosen [Par98] to ensure that differences in the acceptance are below 10^{-4}.

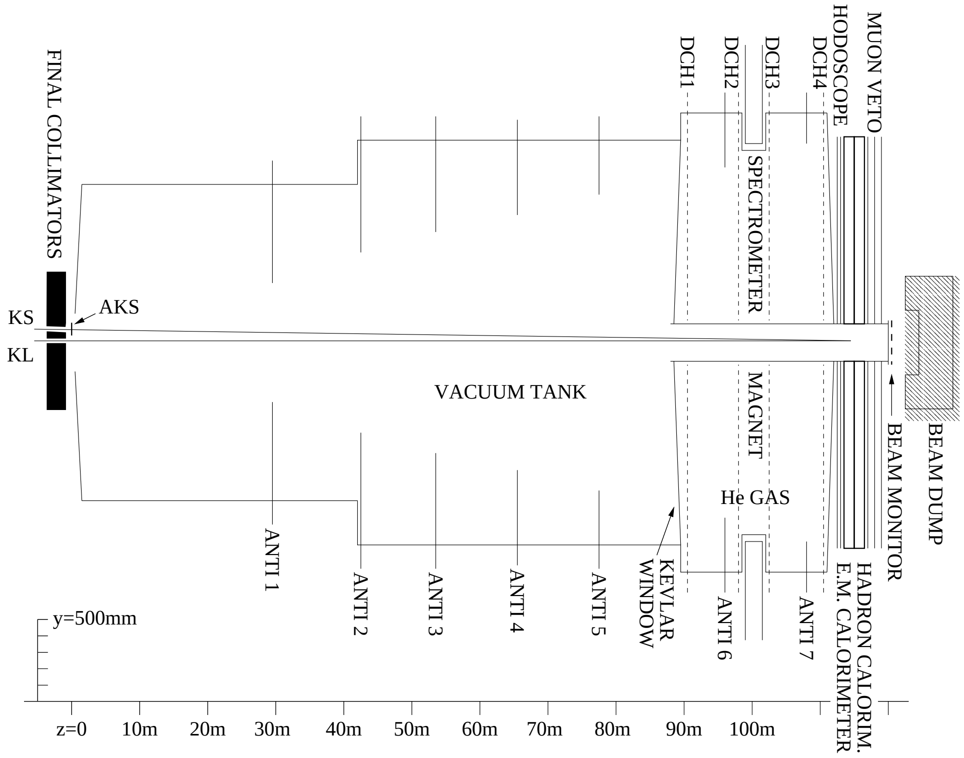

Figure 3: Layout of the main detector components of the NA48 experiment. Note the different scale in the z and y-axis.

4 The Kaon Beams and the NA48 Detector

The design of the NA48 detector exploits the cancellation effect of the double ratio as much as possible. The key features are:

1. Two almost collinear beams, which lead to an almost identical illumination of the detector.

2. Lifetime weighting of the events defined as K_L events.

Therefore acceptance differences between K_S and K_L decays in the two beams are reduced. Figure 3 shows a schematic layout of the detector.

4.1 The Simultaneous K^0 Beams

The two neutral beams [BDG+98] are derived from the CERN SPS proton beam, which has an energy of 450 GeV. A proton spill of 2.4 s duration is extracted every 14.4 s to the NA48 experimental area. The nominal intensity is 1.1×10^{12} protons per burst.

4.1.1 The K_L Target

Figure 4 shows the layout of the beam geometry. The decay lengths at the average kaon momentum of 110 GeV are $\lambda_\mathrm{L} = 3\,480$ m for K_L mesons and $\lambda_\mathrm{S} = 6.0$ m for K_S mesons, respectively. The K_L target is located 126 m upstream of the beginning of the decay region. The neutral beam derived from this target is dominated by K_L decays in the fiducial volume.

The target consists of four 10 cm long Beryllium rods with a diameter of 2 mm. The production angle is chosen to be 2.4 mrad, optimizing the production rate of kaons versus neutrons. After three stages of collimation, the beam divergence is ±0.15 mrad. The total K_L flux is $\approx 1.5 \times 10^7$ per burst.

4.1.2 The Bent Crystal

A bent silicon mono-crystal [DGG96] is used to direct the primary protons which traverse the K_L target without interaction, to the second target. The usage of a bent crystal has four advantages:

1. The size of the crystal is 60 mm. A magnet with an equivalent bending power of 14.4 Tm would be more than 5 m long.
2. The beam is attenuated by a factor of 5×10^{-5} without deterioration of the beam quality.
3. Protons are bent into the desired direction without canceling the sweeping action of the preceeding magnet. A magnet would have increased the flux of background muons by one order of magnitude.
4. The crystal defines the emittance of the proton beam in the horizontal and vertical direction.

The planar channeling effect of the mono-crystal is used to deflect the proton beam (see Figure 5). Two supporting rolls press the crystal to an aluminum cylinder with defined radius of 3.0 m. A goniometer is used to rotate the crystal by an angle Φ about its vertical axis. Thus the effective length of the crystal that the beam traverses can be modified. In this way the deflection angle Θ of the beam is adjusted to be 9.6 mrad.

A tagging detector, described in Section 4.2, is placed in the resulting proton beam to determine a time reference for the protons. The proton

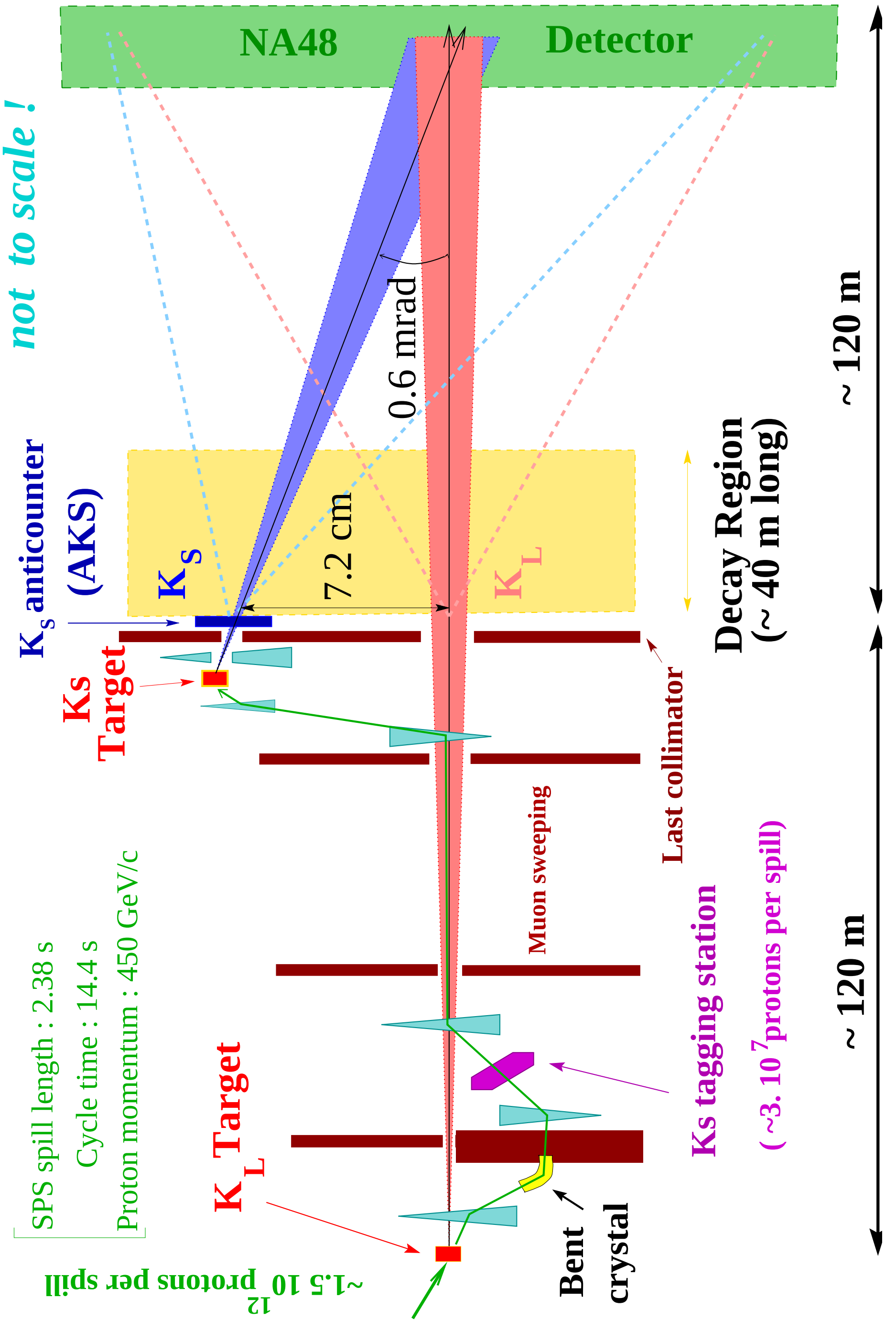

Figure 4: Schematic layout of the beam geometry. Two secondary neutral beams are derived from the CERN-SPS proton beam. The two beams are almost collinear and converge at the detector.

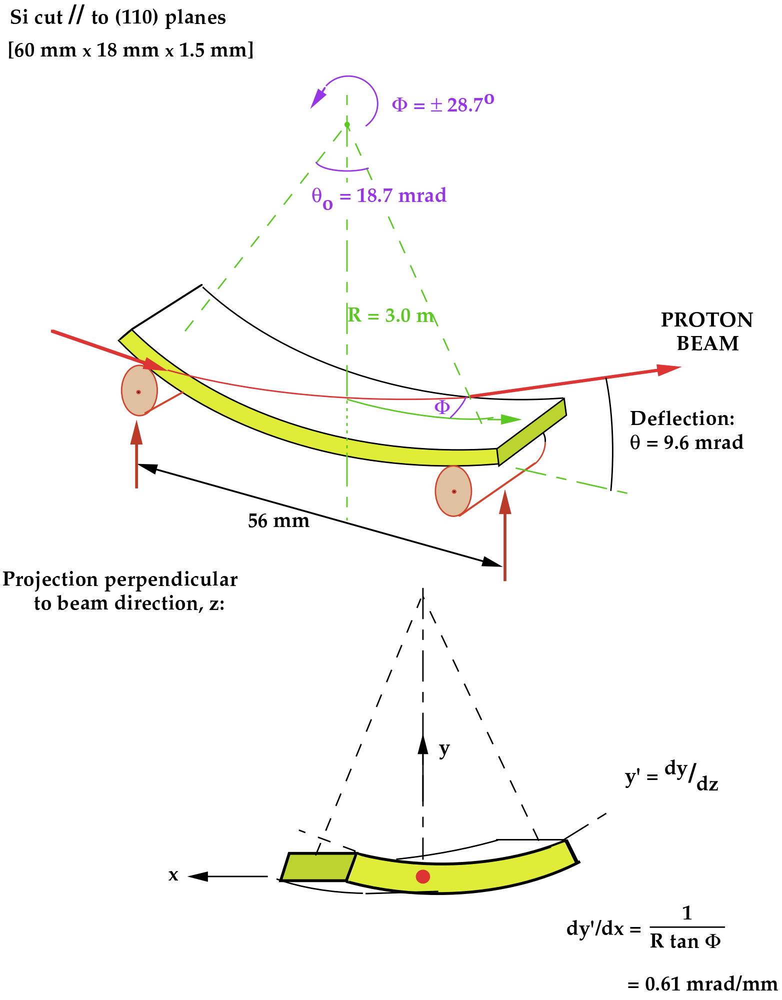

Figure 5: Geometry of the bent crystal.

beam and the secondary neutral beam derived from the K_L target are then transported in a beam pipe towards the main detector.

4.1.3 The K_S Target

About 3×10^7 protons per burst are directed onto the K_S target, which is located 6 m upstream of the decay region. The production angle is 4.2 mrad so that the energy spectrum of K_S decays is as similar as possible to the K_L decay spectrum. The K_S target is placed 7.2 cm above the center of the K_L beam. The two secondary beams are almost collinear: The relative angle of the beams is 0.6 mrad. They converge at the position of the electromagnetic calorimeter, situated 121 m downstream of the K_S target.

The final collimators of both beams are situated about 6 m downstream of the K_S target. The beam divergence of the neutral beam coming from the K_S target is ± 0.375 mrad. This beam is dominated by K_S decays. The resulting K_S flux is $\approx 2 \times 10^2$ per burst.

4.1.4 The Decay Volume

The beginning of the decay region is defined by an anti-counter (AKS). This scintillating detector is used to veto K_S decays occurring further upstream. The decay region itself is contained in an evacuated tank with a length of 90 m.

This vacuum tank is separated by a 0.9 mm (0.003 interaction lengths) thick Kevlar window from the helium tank, which houses the magnetic spectrometer. Within this tank the neutral beam derived from the K_L target is transported through a beam pipe with a diameter of 16 mm.

Seven anti-counter (AKL) consisting of 35 mm iron converter and 10 mm thick scintillator detectors can be used to define the outer limit of the fiducial volume. They define two cones with 10.35 mrad opening angle with the centers of the final collimators as vertex. In this analysis the AKL is not used as veto detector.

4.2 The Tagger

The beam geometry and the lack of angular information in the calorimeter does not allow one to distinguish between the two targets in the neutral decay mode. A tagging detector (Figure 7), consisting of an array of scintillators, is placed in the proton beam directed to the K_S target. 24 scintillators are arranged in a horizontal and a vertical ladder. They are mounted on a carbon fiber support structure. The scintillator thickness varies between 200 μm and

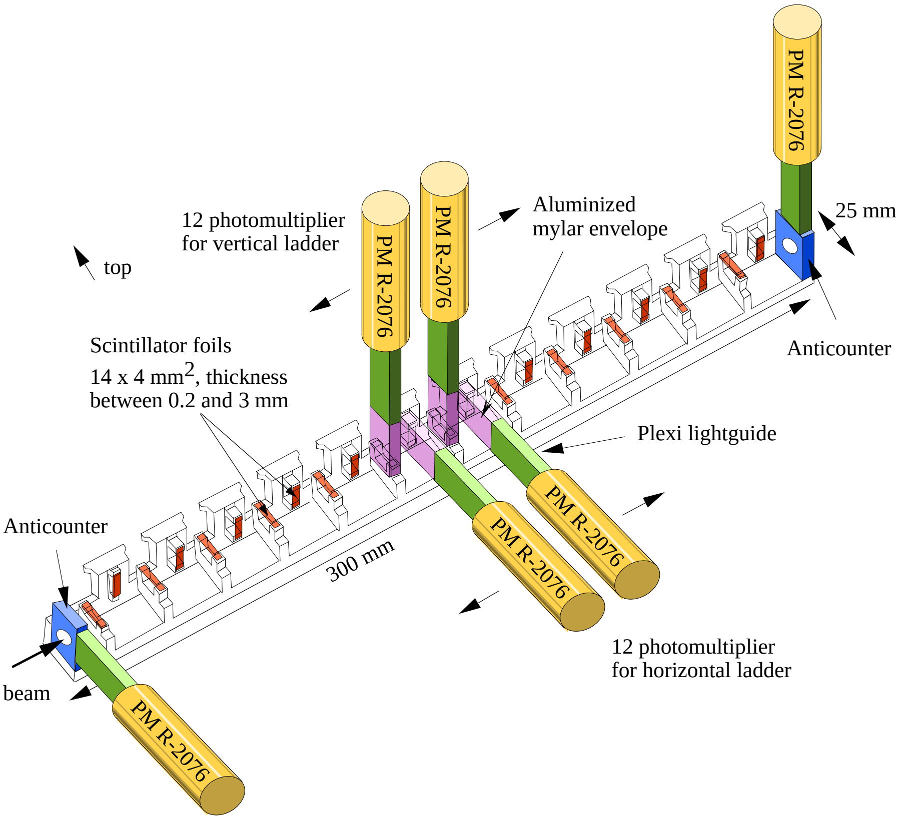

Figure 6: Drawing of the tagging detector. Scintillators are mounted on a carbon fiber structure. The two ladders are read out by photo multipliers.

3 mm in order to achieve an equal proton rate per scintillator, assuming a Gaussian beam profile. Figure 8 shows a cross-section through the Tagger. The overlap between the scintillators is (50 ± 2) μm.

Each scintillator is read out by a photo multiplier and a 8-bit 960 MHz FADC. This leads to a time resolution for a proton of 120 ps; the double pulse separation is 4 ns. If a proton is reconstructed within a time window of ± 2 ns with respect to a decay, the event is defined as K_S event. The absence of a reconstructed proton defines a K_L event.

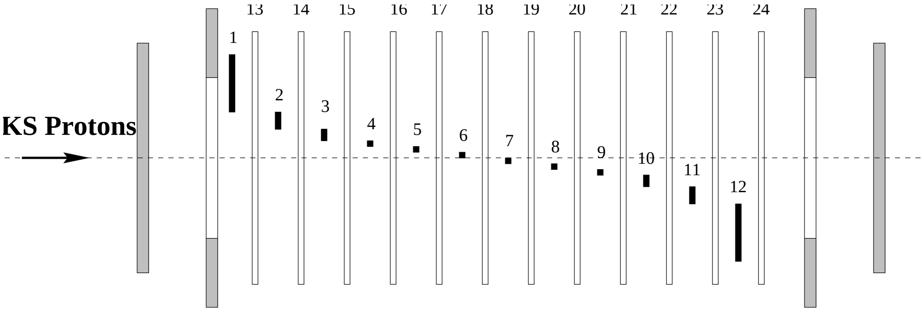

Figure 7: Sketch of a cross-section through the Tagger (not to scale). One ladder is made of 12 scintillators with varying thickness.

4.3 The K_S Anti-counter

The purpose of the K_S anti-counter (AKS) is to define the beginning of the decay region. The AKS also serves to determine the global energy scale for neutral decays.

An uncertainty in the measurement of the z-position of the decay vertex induces an uncertainty in the number of decays, if the fiducial volume is defined by an analysis cut. Moreover, the z-resolution is different for charged and neutral final states. This uncertainty would be large for K_S decays, as the steep exponential decay function would induce a net migration of events into the decay volume. The gains and losses are equal for K_L decays if one assumes a Gaussian z-vertex resolution, as the decay function is practically flat within the fiducial volume. To solve this problem, the beginning of the decay region is defined by a detector which vetoes charged and neutral events occurring further upstream. However, the end of the fiducial volume can be defined by a software cut, as the event numbers are very low because of the exponential decay function.

The AKS consists of four scintillator counters behind the final collimator of the neutral beam derived from the K_S target. The first scintillator has

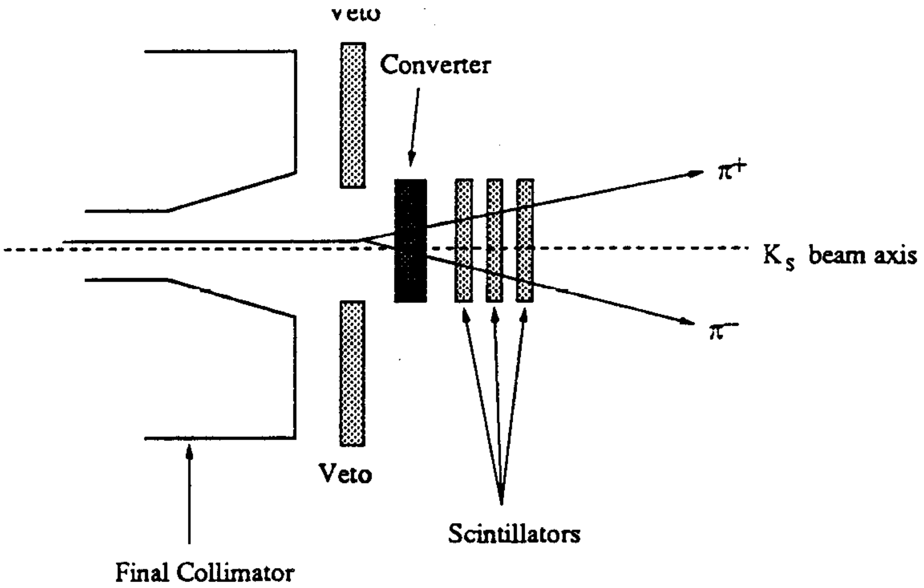

Figure 8: Layout of the K_S anti-counter. The beginning of the decay region is defined by the converter for neutral decays and by the second scintillator (anti-counter 3) for charged decays.

a hole of 3 mm in the middle to allow the beam to pass. The other three scintillators are disks with a diameter of 8 mm. Counter three is used to define the beginning of the decay region for charged decays, while the other counters are used to determine the AKS efficiency.

A 2.96 mm thick iridium crystal is used as a photon converter. The crystal is aligned with respect to the beam as this increases the conversion probability for photons without adding material within the neutral beam. The thickness corresponds to 1.79 radiation lengths X_0 compared to 0.98 X_0 for amorphous iridium of identical thickness. The converter is placed 21 mm upstream of AKS counter 3; thus there is a difference in the beginning of the decay region for charged and neutral final states. This is taken into account in the weighting procedure of the events. The efficiency of the AKS scintillator and the readout has been determined to be 0.9923 ± 0.0010. The probability to have a γ-conversion is 0.9964 ± 0.0003 [Bii99]. To estimate a correction to R, the ratio of the efficiencies is multiplied by the fraction of decays occurring upstream of the AKS, which is 4% for charged decays and 6% for neutral decays. Therefore no correction to R is needed as the result

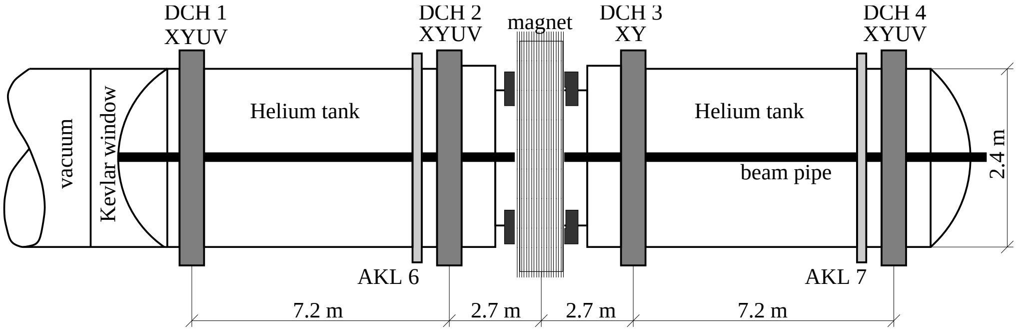

Figure 9: The NA48 spectrometer.

is smaller than 1×10^{-4}.

The position of the AKS is used to define the global energy scale of the calorimeter, as the energy is directly correlated to the distance scale (see equation 7.5 on page 55). The comparison between the reconstructed position of the AKS using $K_S \to \pi^0\pi^0$ decays with the known position determines the energy scale correction factor. The energy scale has been checked daily during the 1997 run.

4.4 The Spectrometer

A magnetic spectrometer (Figure 10) is used to reconstruct tracks of charged particles. The spectrometer consists of a dipole magnet with integrated magnetic field of $\int B\mathrm{d}l = 0.84$ Tm at the nominal current of 1200 A. This leads to a momentum change of 265 MeV/c in the x-direction.

Four drift chambers are used to record the tracks of charged particles. Each chamber consists of 8 planes with 256 sense wires each. The spacing of the sense wires is 1 cm. Two planes together, the A and B planes, build one view (named x, y, u, v) with stereo angles of 0^o, 90^o, -45^o, and 45^o. In chamber three only the x and y views are connected to the readout. The chambers are filled with a 60 : 40 Argon/Ethane mixture.

The spatial resolution of one view is ~ 90 μm. This leads to a momentum resolution of

$$\sigma_p/p \simeq 0.5\% \oplus 0.009\% \times p[\mathrm{GeV}], \tag{4.1}$$

where $\oplus$ means that the terms should be added in quadrature.

The drift chamber readout needs special attention as an overflow condition makes special requirements in the event selection necessary. The amplifier of the chambers are read out by TDC cards. For each hit the time with respect to the global clock is recorded with an accuracy of 25/16 ns. The hit time and the wire address is stored in an output FIFO. For each plane the number of hits within the last 100 ns is counted. In case more than eight hits are found in one plane, the TDC FIFO is reset in order to suppress high multiplicity events. The time when the overflow condition occurs is stored in the data. The maximum time interval between the overflow condition and the reset of the TDC chip is 600 ns. During this interval a $K \to \pi^+\pi^-$ event may thus be lost. This effect needs special care in the event selection, described in Section 7.3.

4.5 The Electromagnetic Calorimeter

A quasi-homogeneous liquid krypton electro-magnetic calorimeter (LKR) [Pal96, B$^+$96] is used to identify the four photons from a $\pi^0\pi^0$ decay. Liquid krypton has a radiation length X_0 of 4.7 cm, which allows one to build a compact calorimeter with very good energy and time resolution. The calorimeter is 1.25 m long, corresponding to $27X_0$.

4.5.1 The LKR Detector

The invariant mass of photon pairs need to be measured accurately in order to achieve a good rejection of $K_\mathrm{L} \to \pi^0\pi^0\pi^0$ background events. Therefore the energy resolution needs to be better than 1%, and the space resolution needs to be better than 1 mm for photons above 20 GeV. Moreover, the geometry and the absolute energy scale must be accurate to the 10^{-4} level. A time resolution better than 0.5 ns for a single shower is required to distinguish K_S and K_L events.

The LKR consists of 13248 cells pointing to the average K_S decay position. The front face of a cell has a size of 2×2 cm^2. The cells increase in size towards the back of the calorimeter with an angle of 10 mrad. Each cell consists of three Cu-Be ribbons, two cathodes and a central anode (see Figure 11). The ribbons are guided by five accurately machined spacer plates (5 mm thick fiber glass reinforced epoxy) and the front and back plate (Figure 12). The electrodes are shaped in an accordion geometry to reduce the non-uniformity coming from the relative position of the shower within the cell. The accordion angle is 48 mrad. The hodoscope for the neutral decay mode (Section 4.7) is located at the second spacer plate.

The 9 m^3 liquid krypton are kept at a temperature of 121 K in a cryostat. Evaporated krypton is filtered, cooled and brought back into the vessel.

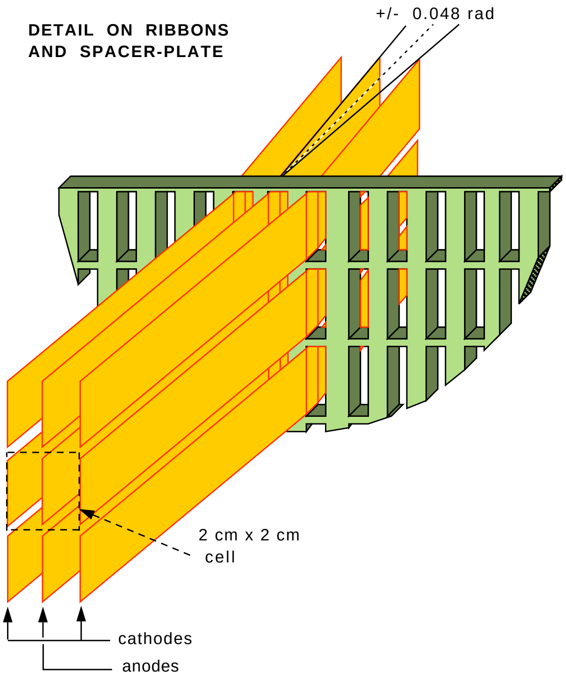

Figure 10: Single calorimeter cell with Cu-Be ribbons guided by the spacer plates.

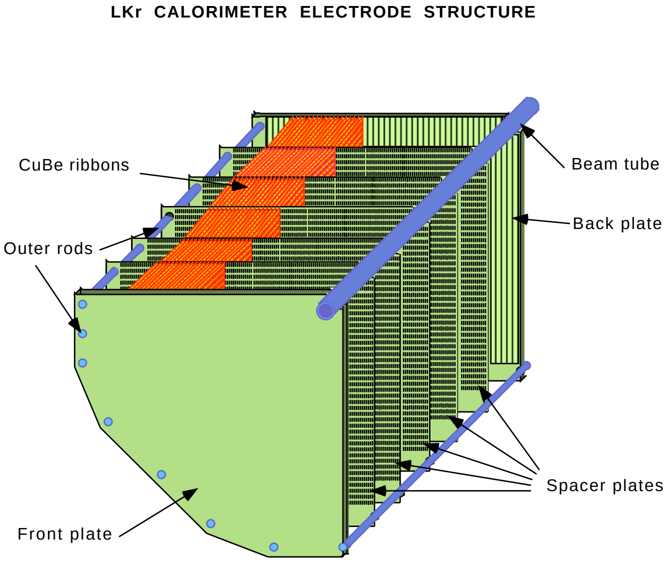

Figure 11: Quarter of the electro-magnetic calorimeter with 5 spacer plates.

4.5.2 The LKR Readout

In order to achieve a good time resolution, an initial current readout is implemented [H$^+$98]. The charge preamplifiers and the electronic calibration system are placed inside the calorimeter in order to have short connections and a fast response.

The calorimeter is calibrated electronically. Every preamplifier is connected to a pulser, which injects a known amount of charge into the amplifier circuit. Eight different pulse heights are used. They are distributed in 64 columns of 2×128 cells. The pulser is controlled by the trigger system.

A transceiver outside the calorimeter transmits the signal via shielded twisted pair cable to the Calorimeter Pipeline Digitizer (CPD). One CPD motherboard houses 32 analog sub-cards (CPDAS) with two channels each.

One CPDAS channel consists of a shaper (Bessel filter) followed by a gain switching amplifier. The output signal is digitized by a 10-bit 40 MHz FADC and stored in a ring buffer. The filter and amplification stage is implemented as a fully custom made ASIC named KRYPTON. At the time of the design 1994, the choice of FADCs was limited to a dynamic range of 10 bit. To extend the dynamic range a non-linear 2-bit FADC determines the expected pulse height and selects one of four possible gains of the amplifier. Thus the effective dynamic range is 12 bit. The gain information is stored together with the ADC value in a 204.8 μs deep ring buffer.

To provide a trigger signal, the output of CPDAS shapers of 2×8 (or 8×2, respectively) adjacent cells are summed up [Fis98]. Thus four analog sums in each of the two projections are calculated for each super cell. The result is then transferred to the Vienna Filter Modules, which are described in Section 5.1.1.

4.6 The Hodoscope for Charged Tracks

A hodoscope (HOD, Figure 13) is used to measure the event time of charged events and to generate a fast trigger signal for decays into charged particles. The hodoscope consists of two planes of plastic scintillators, about 60 cm apart. The separation allows back-scattered background from the calorimeter to be identified. Each plane is divided into quadrants, each consisting of 16 scintillator strips. The width of the strips varies between 6.5 cm and 10 cm.

Each strip is read out by a photo multiplier connected to the PMB (pipelined memory board) readout. The time resolution is about 200 ps per track.

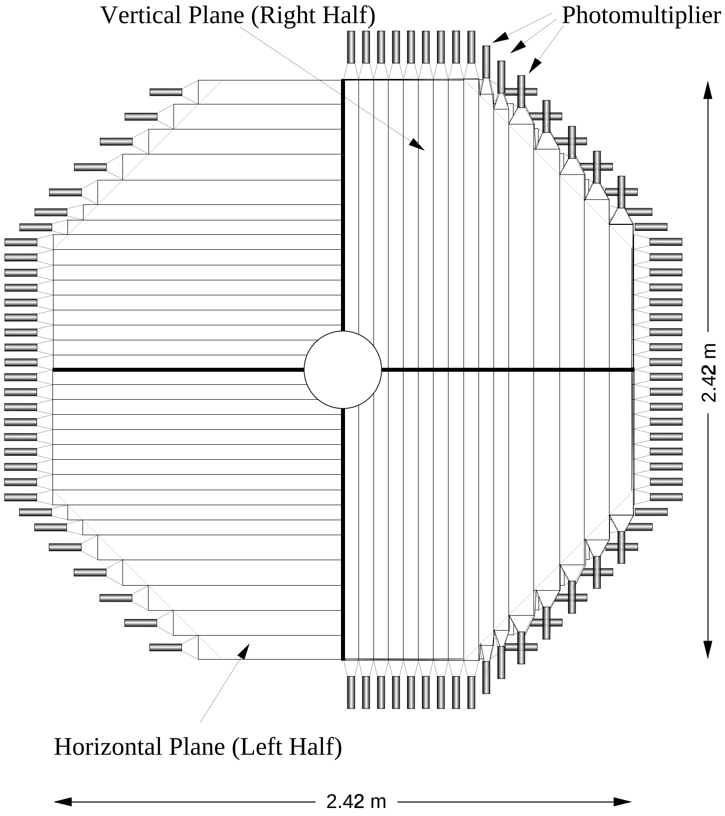

Figure 12: Scintillator counters of the hodoscope for charged decays.

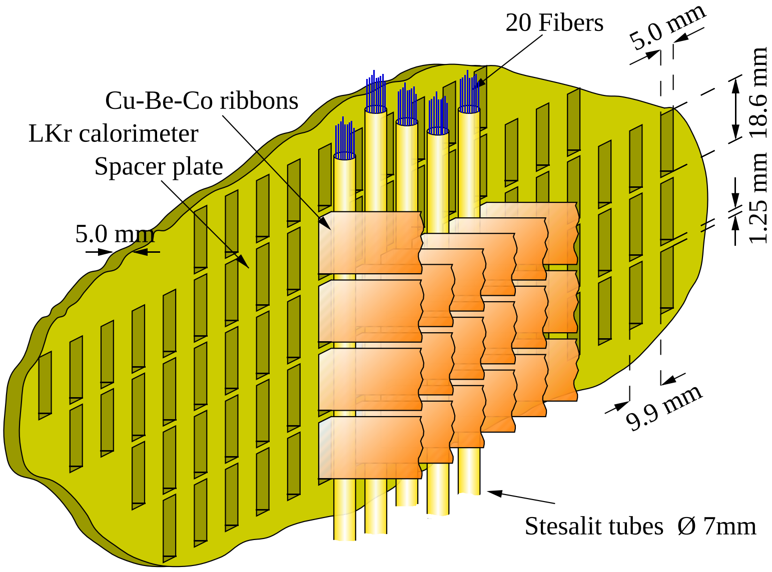

Figure 13: Fiber bundles of the neutral hodoscope within the LKR.

4.7 The Hodoscope for Neutral Particles

The hodoscope for the neutral decay mode (NHOD) is used to provide an independent trigger for neutral decays. It consists of 7 mm diameter tubes, filled with scintillating fibers, within the LKR calorimeter (see Figure 14). The NHOD is placed at the position of the shower maximum (~ 9.5 radiation lengths). A total of 10080 fibers are arranged in 4 quadrants with eight readout channels each. The readout system is the same as for the charged hodoscope (PMB).

4.8 The Hodoscope Readout (PMB)

The PMB (Pipelined Memory Board) readout serves 2 purposes:

1. The digitized signals of the HOD and the NHOD are buffered and added to the data when a trigger is issued.

2. The digital trigger information is stored and read out.

The HOD and NHOD information allows a precise reconstruction of hit times in the sub-detectors. The charging and decharging of a capacitor is continuously digitized with a 40 MHz FADC. This data is stored in the PMBs. In the reconstruction program the signal time is calculated using a fit to the digitized ramp.

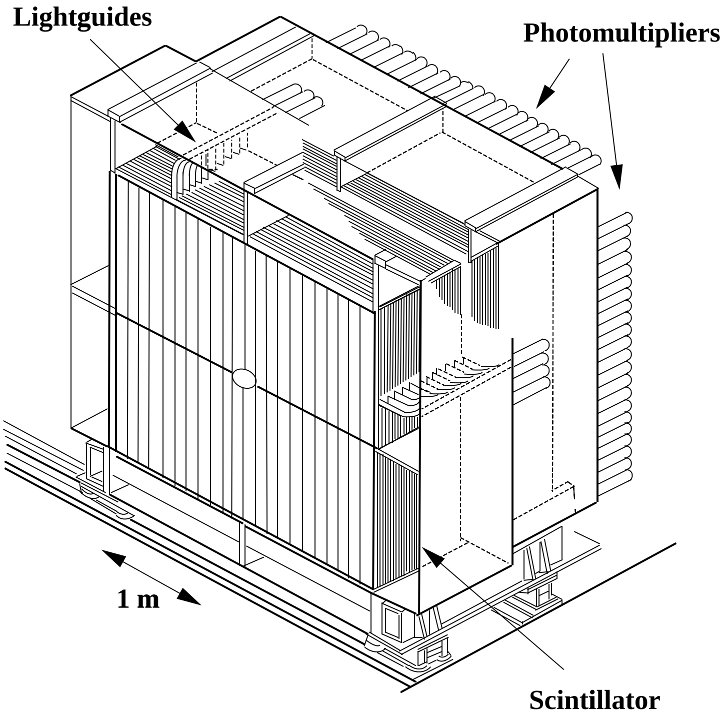

Figure 14: The Hadron Calorimeter.

The PMBs are also used to store the information coming from the charged and the neutral trigger sub-systems without previous digitization process (so-called digital PMBs or Pattern Units). The information is used for monitoring of the neutral trigger. In the charged trigger the Pattern Units are used to determine the efficiency of trigger components, for example of the Q_x and of the E_{tot} trigger signals.

4.9 The Hadron Calorimeter

The Hadron Calorimeter (HAC, Figure 15) is an iron sandwich calorimeter with two modules (front- and back module). The HAC is 1.42 m deep, resulting in 6.7 nuclear interaction lengths. It consists of a total number of 48 2.5 cm thick steel plates and 49 scintillating planes, divided into 44 strips per plane. The strips are alternating horizontally and vertically oriented. Strips are grouped together such that the readout is projective: subsequent strips with the same orientation are read out by a single photo multiplier. Four CPDs, identical to those used in the LKR calorimeter readout (see Section 4.5.2), are used to digitize the signal. The analog sum of the signals is used in the Level 1 Charged Trigger for determining the hadronic contribution to the total energy. This part is described in Section 5.1.1.

4.10 The Muon Veto Counter

A muon veto detector (MUV), consisting of three planes of scintillator, each shielded by 80 cm of iron, is used to identify muons to veto $K_{\mathrm{L}} \rightarrow \pi\mu\nu$ ($K_{\mu 3}$) decays. The first two planes consist of 11 scintillator counters with a thickness of 10 mm each. Plane three has six 6 mm thick counters. The counters are read out by photo multipliers on both ends. All three planes are used to veto events with muons.

4.11 The Beam Intensity Monitor

A Beam Intensity Monitor [Blü95] ('Beam Counter'), located at the end of the beam line, is used to measure the instantaneous K_{L} beam intensity. It consists of square fibers horizontally and vertically aligned. The active area is 1.8×1.8 cm^2. The Beam Intensity Monitor is also used to give a random trigger proportional to the instantaneous beam intensity.

4.12 The K_{S} Monitor

The K_{S} Monitor [BCLM97] is situated in the iron support structure of the K_{S} target. Four scintillator counters give a signal proportional to the instantaneous intensity of the proton beam impinging on the close by target. Four veto counters, surrounding the beam pipe upstream of the K_{S} Monitor, ensure that protons missing the target are not counted directly.

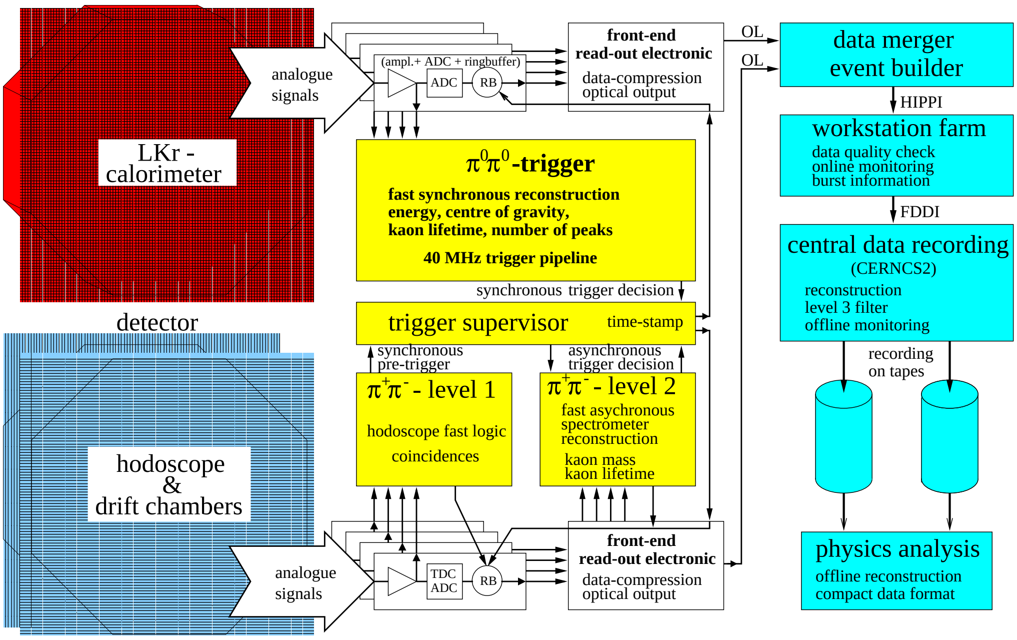

Figure 15: Overview of the NA48 trigger and data acquisition.

5 The Trigger and the Data Acquisition

Trigger and data acquisition are designed to cope with the high rates of the NA48 detector. The trigger consists of two stages, which reduce the total output rate to about 5 kHz with a minimal dead time. The Data Merger (DM) collects the data from the various sub-detectors and builds complete events and bursts. The raw data is then processed by the Level 3 / Real Time Reconstruction program (L3/RTR). Several output streams are saved on tape. Figure 16 gives an overview of the trigger and the data acquisition (DAQ) system.

5.1 The Trigger

The NA48 trigger [Arc99] is an asynchronous trigger in two stages (see Figure 17). One common 960 MHz clock is used as time reference, which is distributed to all sub-systems. SPS control signals determine the beginning and the end of a burst. The first stage of the trigger (Level 1) is implemented as hardware trigger with fast logic modules. The task is to reduce the input rate for the second stage to about 70 kHz. The second stage reduces the trigger rate to about 5 kHz. In the charged branch the so-called "Massbox"

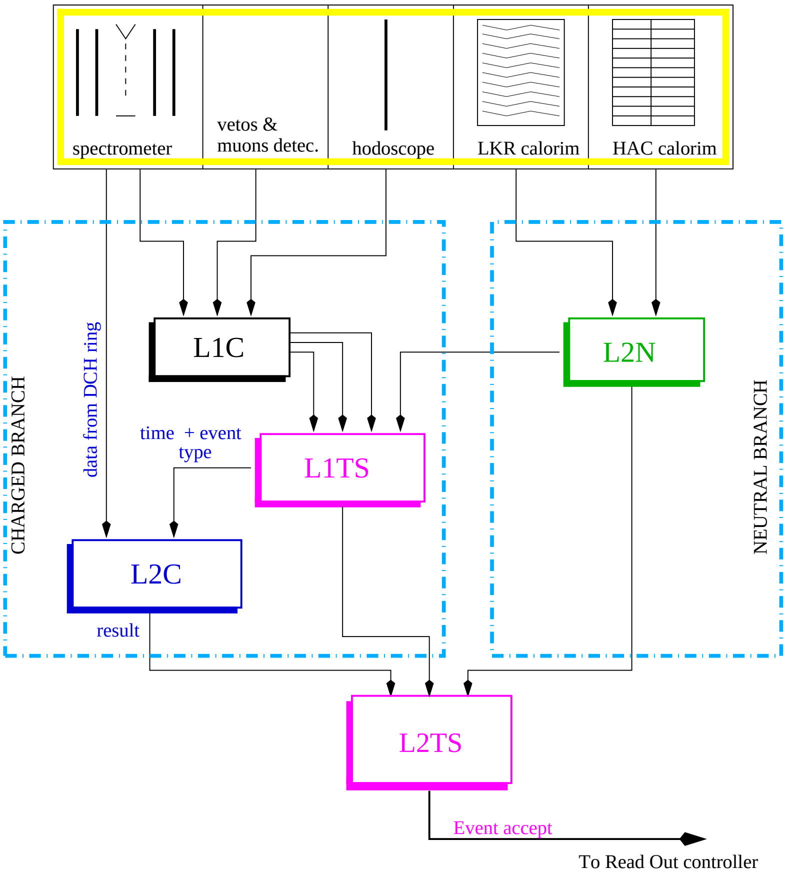

Figure 16: Overview of the 3 stages of the NA48 trigger.

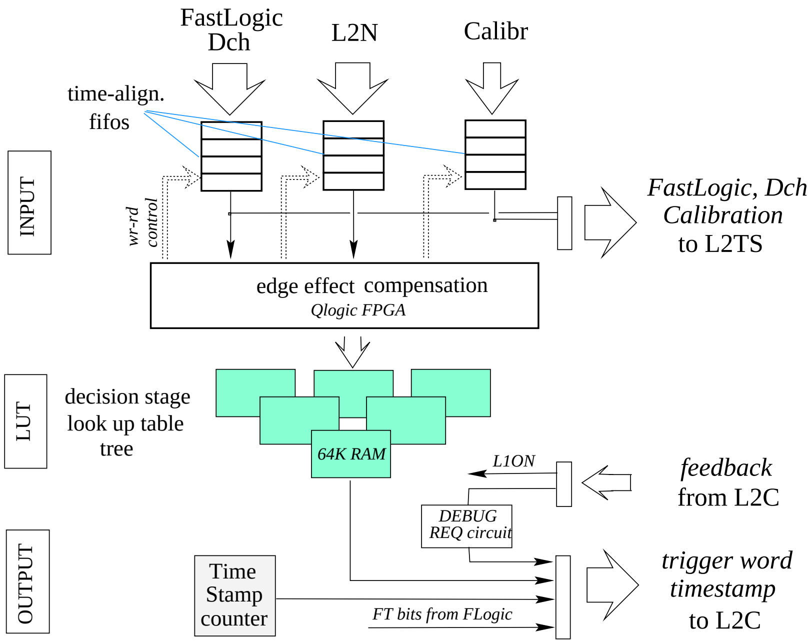

Figure 17: Block diagram of the Level 1 Trigger Supervisor.

imposes cuts on physical quantities such as kaon mass and lifetime. In the neutral branch the two stages are merged. The neutral trigger information is used by the Trigger Supervisor (TS) of both stages.

The Level 1 Trigger Supervisor uses the signals from the hodoscope, the neutral hodoscope, and the neutral trigger. Additional inputs, which are not used in this analysis, come from the anti-counter (MUV and AKL) and from drift chamber one (multiplicity). The first task of the L1TS is to synchronize the input signals. This is achieved with a delay FIFO. The Level 1 Trigger Supervisor then decides, whether a trigger condition is fulfilled. The L1TS has to reach a decision within 5 μs.

A positive decision is passed to the Level 2 Trigger Supervisor and, if a charged trigger is issued, the Level 2 Charged Trigger (L2C) is started. The L1TS also generates a time stamp and a fine time of the Q_x signal, which are both used by the L2C.

The L2TS receives the information from the L1TS, the L2C and the L2N. It can queue up to five trigger requests. The guaranteed minimum time span between two trigger is 20 μs. If a positive trigger decision is reached, the readout of all sub-detectors is started. The time stamp sent by the L2TS is used to extract the event from the ring buffers of the sub-detectors. The data is then sent to the Data Merger.

5.1.1 The Neutral Trigger

The Vienna Filter Modules (VFM) receive the information of the super cells from the CPDs of the calorimeter [Fis98] (see Section 4.5.2). The signal is digitized and summed-up into 64 channels for the x and y-projection. In the Peak Sum System (PSS) the number of peaks per projection, their associated time, the total energy (zeroth order moment) and the first and second order moment are calculated. The n-th order moments $m_{n,v}$ per view v are defined as:

$$m_{0,v} = \sum_{i=1}^{64} E_i^v, \tag{5.1}$$

$$m_{1,v} = \sum_{i=1}^{64} E_i^v \times (i-32), \tag{5.2}$$

$$m_{2,v} = \sum_{i=1}^{64} E_i^v \times (i-32)^2, \tag{5.3}$$

where i is the index of the channel.

Look Up Tables (LUT) use these values to calculate physical quantities combining the two views. Here the total energy E_{LKR}, the center of gravity (COG), the distance d of the z-decay vertex from the calorimeter, the kaon lifetime τ, and the fine time of the event are calculated:

$$E_{\mathrm{LKR}} = \frac{m_{0,x}+m_{0,y}}{2}, \tag{5.4}$$

$$\mathrm{COG} = \frac{\sqrt{m_{1,x}^2+m_{1,y}^2}}{E_{\mathrm{LKR}}}, \tag{5.5}$$

$$d = \frac{\sqrt{E_{\mathrm{LKR}}(m_{2,x}+m_{2,y})-(m_{1,x}^2+m_{1,y}^2)}}{m_{K^0}}, \tag{5.6}$$

$$\tau = \frac{d_{\mathrm{AKS-LKR}}-d}{E_{\mathrm{LKR}}/m_{K^0}\cdot c\tau_{K_{\mathrm{S}}}}. \tag{5.7}$$

After applying the selection summarized in Table 4, a trigger decision is provided for each time slice (25 ns). The trigger decision is passed to the Trigger Supervisor (see Section 5.1). The digital information after each step is recorded by the PMB system and added to the data.

5.1.2 The Total Energy Trigger

The analog sum signal of one super cell of the HAC is also digitized by two VFM modules. In the LUT system the HAC and LKR signals are synchro-

quantity	cut
E_{LKR}	≥ 50 GeV
COG	≤ 15 cm
τ	$\leq 5.5\ \tau_{K_S}$
# peaks x-projection	≤ 6
# peaks y-projection	≤ 5

Table 4: Selection criteria of the neutral trigger.

nized and calibration factors for the front and back HAC are applied. If the total energy $E_{\mathrm{tot}} = E_{\mathrm{LKR}} + E_{\mathrm{HAC}}$ is greater than 30 GeV, the E_{tot} trigger signal is sent to the Level 1 and the Level 2 Trigger Supervisor.

5.1.3 The Charged Trigger

The charged trigger [C$^+$97b, C$^+$97a] has three stages: Level 1 Charged (L1C), the Level 1 Trigger Supervisor (L1TS), and Level 2 (L2C). The requirements in the three stages are:

- **Level 1 Charged:** The quadrants of the charged hodoscope are extended by two adjacent counters of the neighboring quadrant. Two diametrical quadrants of the hodoscope are required to be in coincidence (Q_x condition): $Q_x = ((Q_{V1} + Q_{H1}) \times (Q_{V3} + Q_{H3})) + ((Q_{V2} + Q_{H2}) \times (Q_{V4} + Q_{H4}))$. The Fine Time (FT) of the Q_x signal in units of 6.24 ns with respect to the 40 MHz clock is recorded.

- **Level 1 Trigger Supervisor.** The Q_x signal is down-scaled by a factor of 2 and, in a different branch, by a factor of 128. The E_{tot} signal coming from the neutral trigger (Section 5.1.2) is widened dynamically, depending on the most significant bit (MSB) of the Q_x Fine Time. Table 5 gives an overview of the possible cases. The coincidence of $Q_x/2$ with the widened E_{tot} signal is required. If the coincidence is missed due to edge effects caused by unavoidable time jitters, the charged trigger is inefficient. Thus the L1C trigger signal is $Q_x/2 \cdot E_{\mathrm{tot}} + Q_x/128$. The $Q_x/128$ fraction is used to measure the E_{tot} efficiency. In addition a down-scaled fraction of the Q_{OR} trigger is accepted as well.

- **Level 2.** Drift chamber information is used to calculate physical quantities such as mass, decay vertex, and lifetime. If all cuts are fulfilled, the positive decision is sent to the Level 2 Trigger Supervisor. The L2TS starts the readout of all sub-detectors.

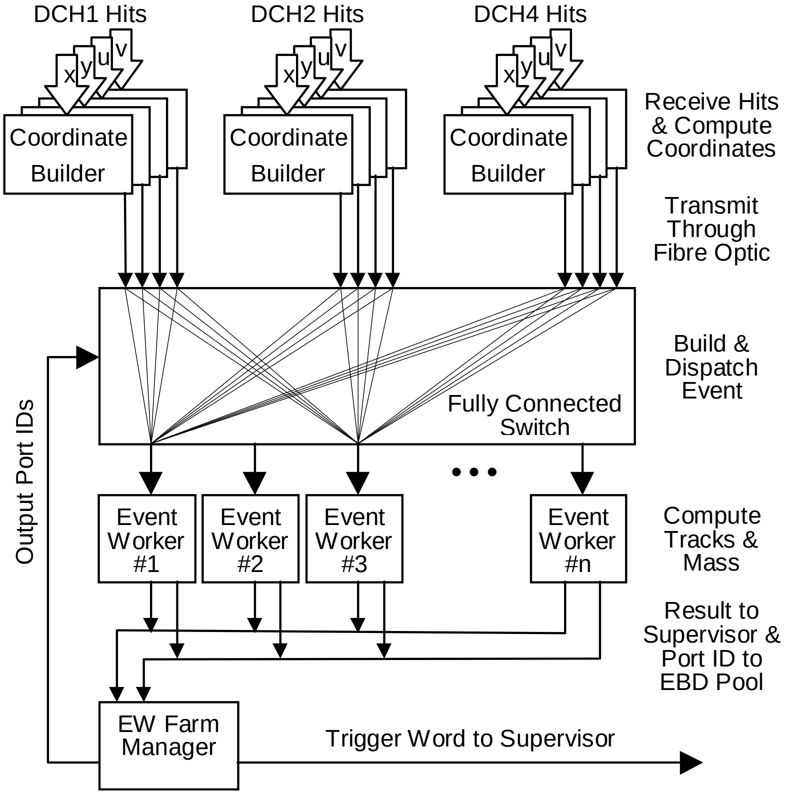

Figure 18: Block diagram of the Level 2 Charged Trigger [A+98].

time slice	12345	12345	12345	12345	12345	12345
$Q_x/2$	00100	00100	01000	00010	01000	00010
Q_x FT MSB	00000	00100	01000	00010	00000	00000
E_{tot}-in	00100	00100	00100	00100	00100	00100
E_{tot}-out	00110	00110	x1110	x0100	x1100	x0110

Table 5: Dynamic widening of the E_{tot} signal [AM98]. The output of the E_{tot} signal is given for possible combinations of the input signals. Per definition, the E_{tot} input signal is located in time slice 3. The Q_x signal may jitter around this position by ±1 time slice. The Fine Time bits can as well have a jitter with respect to the $Q_x/2$ signal. This is the case for the marked column, where $Q_x/2$ and E_{tot}-out are not in coincidence. These edge effects lead to an inefficiency of the charged trigger.

The L2C [DH96, $\mathrm{A}^{+}98$] is built as combined hardware and software real time processing system. A trigger decision has to be available within 100 μs and the event rate has to be reduced to $\sim$ 2 kHz. A block diagram of the L2C is given in Figure 19. The following calculation steps are performed:

1. Each view of drift chamber 1, 2, and 4 is connected to a Coordinate Builder (also called A & B card, equipped with Xilinx firmware). A coordinate is calculated from the event time and from the drift time measured in the two planes of one view. For the calculation the Q_x Fine Time information is used.

2. An Event Builder and Dispatcher sends all coordinates of one event to an Event Worker Farm.

3. An Event Worker calculates space points and executes the algorithm to select a good event:

   (a) Tracks are constructed from all possible combinations of space points. Tracks are combined to vertices. The closest distance of approach (CDA) of two tracks must be < 5 cm, the opening angle must be < 15 mrad.

   (b) The z-decay vertex is calculated. A selection of 100 cm $\leq z_{\mathrm{vtx}} \leq$ 4260 (4800) cm is performed. The upper z-vertex value changed during the data taking from 4260 cm to 4800 cm.

   (c) The tracks belonging to a selected vertex are extrapolated to drift chamber four. The invariant mass m is calculated using the pion hypothesis from associated space points within a certain y-band of the extrapolated track. A cut of $0.95\ m_{K_{\mathrm{PDG}}} \leq m$ is applied. The mass resolution achieved is 5 MeV/c^2.

   (d) The lifetime is calculated and a selection of $\tau \leq 4\ (4.5)\ \tau_{K_\mathrm{S}}$ is done.

4. An Event Worker Farm Manager transfers the trigger decision to the Level 2 Trigger Supervisor.

Run number	4705 - 5066	5067 - 5290	5291 - 5377
lifetime	$< 4\ \tau_{K_\mathrm{S}}$	$< 4.5\ \tau_{K_\mathrm{S}}$	
z-decay vertex	$1.0 < z_{\mathrm{vtx}} < 42.6$ m		$1.0 < z_{\mathrm{vtx}} < 48.0$ m
CDA	< 5 cm		
opening angle of tracks	< 15 mrad		
invariant $\pi^+\pi^-$mass	$> 0.95\ m_{K_{\mathrm{DPG}}}$		

Table 6: Massbox selection criteria for different run periods [DGdC98].

The Massbox achieves a rejection power of 60. The selection criteria are summarized in Table 6. The overall latency is 80 μs per event. About 1% of the events cannot be processed in time (so called “watch dog” events). The total L2C can sustain an input rate of 70 kHz.

5.2 The Data Acquisition

The data acquisition consists of several sub-systems: the sub-detector readout, the Data Merger, which builds complete events, the Front End Workstations (FEWS), which store completed bursts, Monitor Workstations (MWS) for online monitoring of data quality, and the Central Data Recording, which writes the data on tape. Figure 20 gives an overview of the data flow.

5.2.1 The Sub-Detectors

The data of the sub-detectors are constantly digitized with a frequency of 40 MHz and stored in ring buffers. Each ring buffer is at least 200 μs deep. The Trigger Supervisor issues a readout request containing the event number, the time stamp, and the trigger code of the event. According to the time stamp the corresponding part of the ring buffer is read out. The Read Out Controller of the sub-detector appends an end-of-event code and sends the data via optical link to the Data Merger. The optical link can sustain a rate of 10 MByte/s.

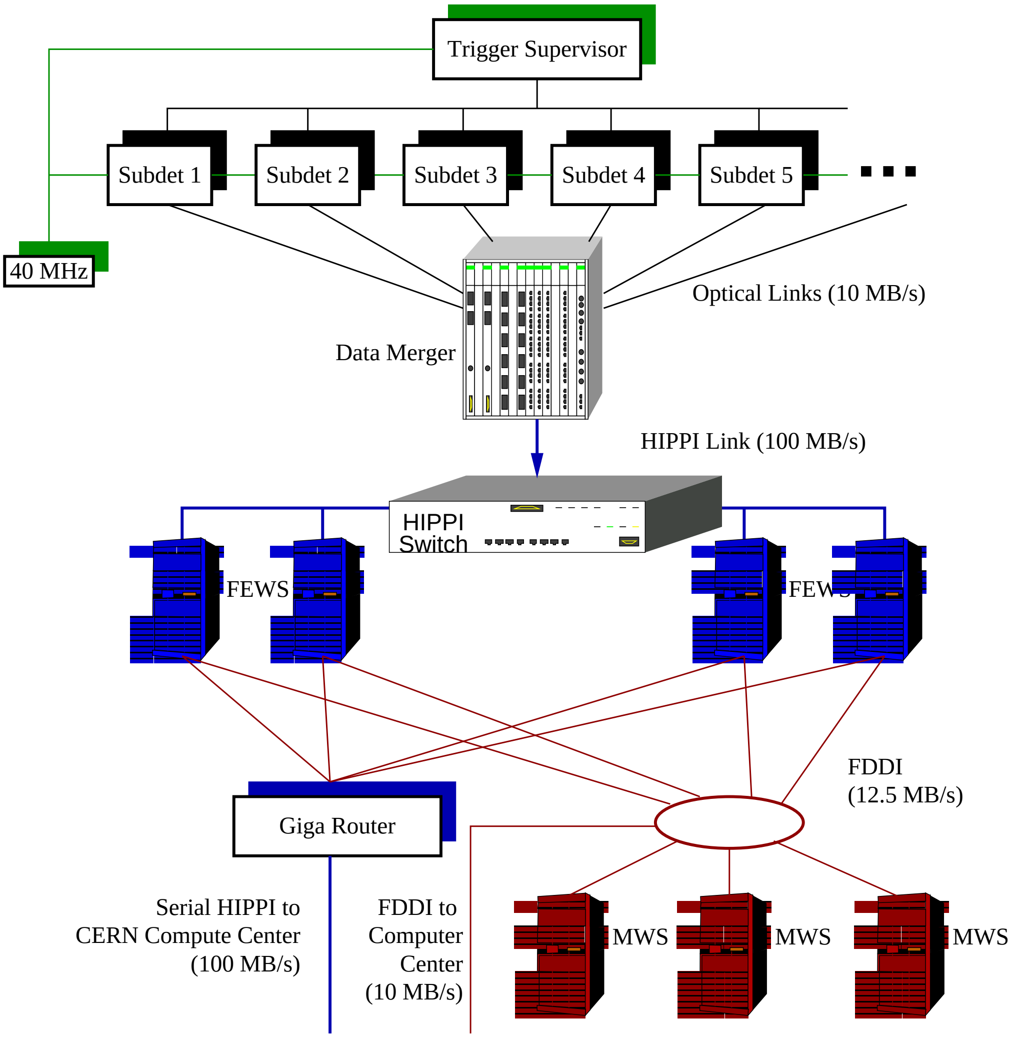

Figure 19: Overview of the NA48 data flow.

5.2.2 The Data Merger

The Data Merger has Input Buffers (IB) for each sub-detector, which receive the incoming data in an asynchronous mode. If the event is completed, a token is passed between the IBs and each IB is read out. A special bus with a bandwidth of 100 MByte/s ("R-Path") is used for this task. The data is transmitted via the FIFO Output Formatter (FOF), which adds a header and a trailer to the data block. The complete burst is sent via HIPPI (High Performance Peripheral Interconnect) link to one of the Front End Workstations (FEWS).

5.2.3 The Front End Workstations

Four DEC 3000 machines have been used as Front End Workstations. They are connected to the Data Merger via a HIPPI switch so that bursts can be sent to different workstations. The FEWS builds an event list and saves the burst to a local hard disc. At the same time the burst is transferred to the CERN computer center via a serial HIPPI connection. Figure 21 shows the set-up and the connection of the workstation farm and the CERN computer center. The FEWS also check the integrity of the data format and send a subset of events to the Monitor Workstations. There the events are completely reconstructed and online histograms are filled.

5.2.4 The Central Data Recording

At the CERN computer center the data is received by the Meiko CS-2, a super-computer with 128 processors. About 1 TByte disk space is connected to the CS-2 as parallel file systems. After a burst is received, it is saved to disk and the reception is acknowledged so that the FEWS can delete the burst from disk. The processes on the CS-2 are running independently and asynchronously so that the system is redundant and failure tolerant. The following tasks are performed by the Central Data Recording (CDR):

1. The burst is added to a database. The database keeps track of the position of the burst on disk and what the processing status is.

2. The burst is saved to tape. This is the primary task which has the highest priority.

3. One of the Level 3 / Real Time Reconstruction (L3/RTR) daemons processes the burst. Each event is reconstructed and classified. Depending

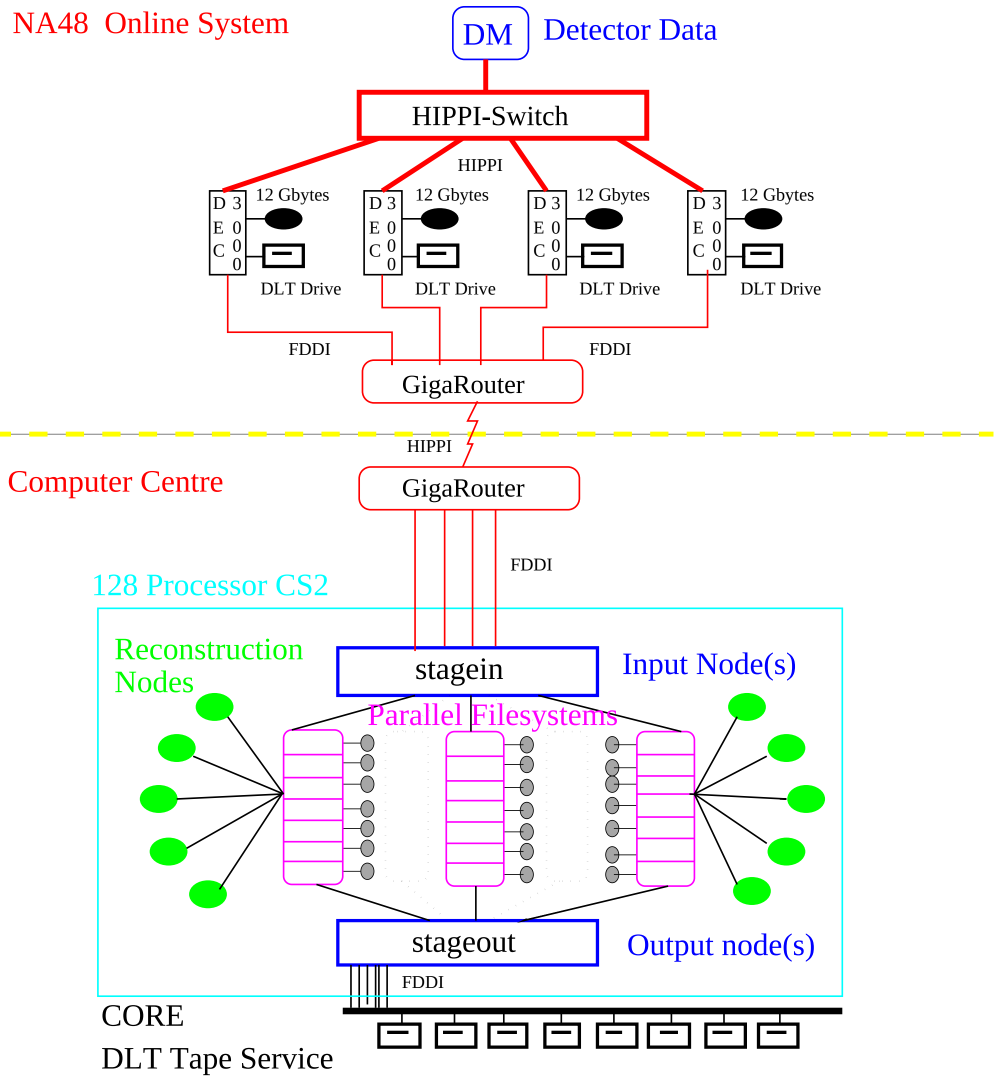

Figure 20: Setup of the NA48 online system and the Central Data Recording.

on the result the event is sent to different output streams. Two output formats are possible: raw data format and the COmPACT[1] data format. The COmPACT data format is a reduced data summary format containing mainly physical quantities, which are computed by the reconstruction software. While a raw data event has a size of about 15 kByte, the COmPACT event has a size of about 1.9 kByte.

4. Each L3/RTR output burst is saved to tape.
5. If the disks are filled up to a level of 650 GByte, bursts which are taped and processed by the L3/RTR are deleted from disk.
6. If the disks are filled up to a level of 800 GByte, bursts which are taped are deleted from disk. In this case the processing by the L3/RTR is omitted to ensure the ongoing of the data taking.

As database a UNIX file system is used. For each task a separate database corresponding to a directory exists. Each burst is represented by a file or another directory, containing information about the burst like burst length, time of creation, ID of the processing PC, position on disk, position on tape, etc. Depending on their state, entries are moved, copied, or deleted from the corresponding database.

The controlling jobs are implemented as scripts, either shell-scripts or perl-scripts, which increases the portability. This has been useful, as for the data taking from 1998 on the CS-2 has been replaced by SUN-Enterprise computer as disk servers and PCs running Linux as compute server. Each job is running independently to ensure asynchronous data processing. If one of the jobs fails, data taking itself is not concerned, as long as bursts are accepted, taped and afterwards deleted from disk. Each job searches its input database for bursts to be processed. The corresponding action is performed and the input and output databases are modified.

5.3 The Level 3 / Real Time Reconstruction Software

The Level 3 / Real Time Reconstruction Program has three tasks:

1. The selection of events which are used for calibration and for checks of the data quality during the data taking.
2. The pre-selection of events which are used for the final analysis during data re-processing.

---

[1] **C**ompact **O**pti**m**ized **P**rogram to **A**ccess **C**ountless **T**erabytes

3. The reduction of the data volume in order to increase accessibility by using the COmPACT output format.

In order to fulfill this task, the program consists of four loops over the various modules. The decoding or reconstruction of each sub-detector corresponds to one of the modules. Which module is switched on is steered by the trigger word. The loops are:

1. **L3 Pass.** In the first pass only those reconstruction modules are executed, that are needed for the Level 3 selection. For a charged event this is the DCH and the LKR reconstruction. For a neutral event this is the LKR reconstruction alone. Based on the trigger word and a few variables such as E/p, a decision is reached whether the event is selected for one of the output streams, and whether the following passes are needed[2].

2. **Filter Pass.** All reconstructions necessary for the filter modules are executed. For events with charged trigger this is the HOD and PMB reconstruction. In the filter modules the decision is taken whether the event is kept for the final analysis. These events are foreseen for one of the COmPACT output streams.

3. **Reconstruction Pass.** For events passing at least one of the filters all reconstruction modules not yet executed are called. The results of the reconstruction are written out in COmPACT format.

4. **Overlay Pass.** A fraction of the events selected by the filter is overlaid with a random event to estimate the effect of accidentals (see Section 8.10). Events are overlaid at the level of decoded raw data. The reconstruction is repeated for the overlaid event. Overlaid events are written in COmPACT format into the same output streams as the original event.

At the end of the second pass events are selected by specialized filter modules for the final analysis. The filters most important for this analysis are [FHK$^+$98]:

1. **Neutral Filter.** The neutral filter requires a minimum total energy deposited in the LKR calorimeter of 50 GeV. The number of shower has to be between 4 and 25. Each cluster has to have an energy of at least 2 GeV. All clusters must be within a time interval of 12.5 ns.

---

[2] During the data taking 1997 no selection for the main data output has been performed. All the data taken was also taped.

The center of gravity must be within radius of 15 cm around the K_L beam axis. The reconstructed lifetime must be below six times the K_S lifetime, and the ellipse number (see Section 7.2) must be smaller than 20. In order to select the photon pairing for the ellipse number selection the χ^2_m variable (equation (7.6)) is used.

2. **Charged Filter.** The closest distance of approach of the two tracks belonging to a vertex must be smaller than 5 cm for the event to be selected. The center of gravity must be within a 12 cm radius and the reconstructed invariant $\pi^+\pi^-$ mass must be between 477.67 MeV and 517.67 MeV. The lifetime must be lower than five times the K_S lifetime. A powerful criteria rejecting events with electrons is the requirement that for both tracks the ratio E/p must be smaller than 0.95.

3. **Additional Filter.** There are more filters (e.g. Rare Decay Filter, Lambda Filter, 4-track Filter, K_{e3} Filter), which are not used in this analysis and therefore are not described here. For a description see [FHK$^+$98].

After each of the passes events can be written into one of the output streams. The following output streams have been defined:

1. **Goldraw.** Events selected by the Neutral Filter, the Charged Filter, or the Rare Decay Filter are written out in raw data format. A reduction by a factor of about 14 is achieved compared to the incoming data.

2. **Goldcompact.** The same events which are written into the Goldraw output stream are also written out in COmPACT data format.

3. **Ke3raw.** A special filter selects events containing an electron track in order to cross-calibrate the LKR calorimeter cells. The raw data is needed to be able to re-run the reconstruction, in case problems were found in the analysis.

4. **Ke3compact.** The same events as before are as well written in a reduced COmPACT output format just containing the track and the cluster information.

5. **Calibration.** Events needed for the detector calibration are written in raw data format into this output stream. The events are identified by the trigger word and are of type HAC pulser, laser trigger, LKR calibration, and random trigger.

In order to further reduce the amount of data Goldcompact data, a compressed SuperCOmPACT format has been introduced. SuperCOmPACT is a data format, which contains only physical quantities relevant for the final analysis. In this way it has been possible to reduce the size of the data to 6.4 GByte and to run over the complete set of data within a matter of hours. For the SuperCOmPACT production more event selection criteria are added to further reduce the background [MWS99]. All requirements are less selective than the ones used in the final analysis described in Section 7 and act on the same variables. Therefore they are not described here. The final SuperCOmPACT sample contains 21.6×10^6 events, which is a reduction by a factor of 5 with respect to the Goldcompact data sample.

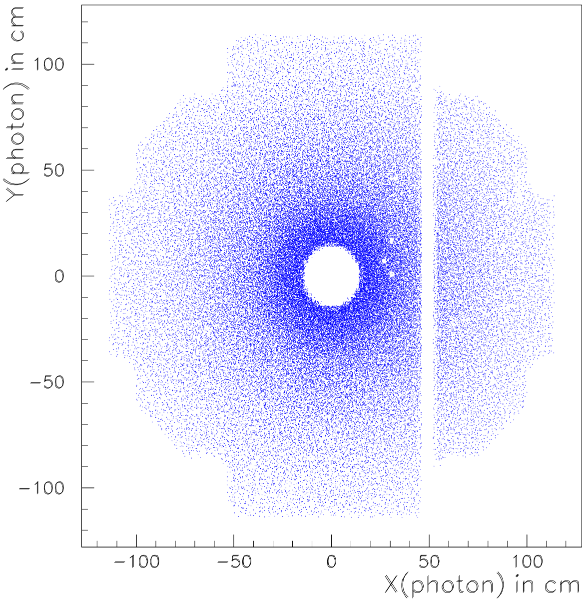

Figure 21: Hit map of photons at the LKR. Clearly visible is the column that is not connected to the high voltage.

6 The 1997 Data Taking

The first data taking period for the $\mathcal{R}e(\varepsilon'/\varepsilon)$ measurement lasted for 42 days in September and October 1997. The beam intensity was 2/3 (1×10^{12} protons per pulse) of the nominal intensity due to a fire in the SPS some weeks before. During this time about 24 TByte of raw data have been recorded.

One of the columns of the LKR calorimeter was not connected to the high voltage, as can easily be seen from the hit map (Figure 22). The dead region corresponds to a 4 cm wide strip. The high voltage was also reduced to 1.5 kV because of a problem with capacitors on the boards for the high voltage connection. Both problems have been fixed in the 1997/1998 winter shut-down.

Short periods with special data taking conditions are used to study systematic effects. Periods, so-called K_S-runs, where only the beam derived from the K_S target is used, have been used to determine the efficiency of the K_S identification with the Tagger. A so-called η-run at the end of the data taking period has been used to study the energy scale. A π^0 beam impinges on a 3.5 cm thick CH_2 target, placed 30 cm downstream of the AKS. The reconstructed z-decay vertex position of the produced π^0 is compared to the known position of the target to determine the energy scale (see Section 8.3).

7 The Reconstruction and Event Selection

7.1 The Reconstruction of the Charged Final State

The reconstruction of the drift chambers is split into two parts. In the first part tracks are built without using the drift time information. In the second part drift times are used to refine the tracks.

As a first step hits in the A and B planes of each view are grouped together to clusters. One of the planes can have two hits so that a cluster consists of 1, 2, or 3 hit wires. Track segments are formed from the clusters of identical views in chamber one and two. A segment is a projection of a track in one of the views. The angle of one segment with respect to the beam direction must be smaller than 20 mrad. The four segments of the views build one track. These tracks are then extrapolated to chamber 4.

In chamber 4 space points are built from the clusters. If a space point is found in a certain search region around the extrapolated intersection point of a track with chamber 4, this point is associated to the track. The search region is equivalent to a requirement on the bending angle of the track. The angle must be smaller than 45 mrad in the x-view, smaller than 5 mrad in the y-view, and smaller than 35 mrad in the u-view and in the v-view.

In the second part the drift time information is used to increase the accuracy of the track information. Ambiguities are resolved and mini-tracks are formed. Several mini-tracks can be formed out of one of the previous tracks. The mini-tracks are selected with a χ^2 test. For each of the selected tracks the time information is stored.

The track momentum and the sign of the charge is determined using the measured space points and the integral of the magnetic field along the track. A map of the magnetic field has been determined using a Hall probe. The z-position of the decay vertex for pairs of tracks with opposite charge is defined by the closest distance of approach (CDA) of the two tracks. The x and y-coordinates of the decay vertex are defined as the center point between the two tracks.

The kaon energy is determined using the opening angle of the tracks. This procedure reduces systematic effects due to the magnet and multiple scattering. For the calculation the opening angle Θ of the two tracks and the energy E_{+-} of the single tracks is used:

$$R = \frac{(E_+ + E_-)^2}{E_+ E_-}, \tag{7.1}$$

$$E = \frac{\sqrt{(m_K^2 - m_\pi^2 R)R}}{\Theta}. \tag{7.2}$$

The tracks belonging to a reconstructed vertex are extrapolated to the hodoscope. Hodoscope hit times are corrected for the impact position of the hits. The times of hodoscope hits associated to a track are used to calculate the charged event time. In this way up to four hodoscope hits can be used per event.

The DCH tracks are extrapolated to the muon veto counter. Within a certain region an associated hit in the MUV is searched for. The search region depends on the track momentum to account for multiple scattering effects, which are more likely for particles with low momentum. If the extrapolated track is close to the edge of a strip, also the neighboring scintillator is taken into account. If a hit in one of the three muon veto planes is found, the hit time is associated to the track.

7.2 The Reconstruction of the Neutral Final State

The first step of the LKR reconstruction [Una95, Una98] is to convert the ADC counts into energy for each cell. The pedestal is subtracted using the first 3 samples, which do not contain the signal. The conversion factor is obtained from the electronic calibration. Seed cells which are a local maximum compared to the eight surrounding cells and have an energy greater than 0.2 GeV are searched. Only seeds which are a local maximum in time are kept. Clusters are built using the cells within an 11 cm radius around the seed cell. For each of these cells the energy and time is determined using a digital filter. 11 different pulse shape categories have been found [Una98], each having a different set of constants for the digital filter. An energy sharing algorithm, using a parameterization of the measured transverse shower development, is applied to cells belonging to more than one cluster. The energy of each cell is corrected by a factor, found from the analysis of K_{e3} data. The cluster energy is the sum of the energy of each cell belonging to the cluster. The cluster time is given by the time information of the seed cell, whereas also the surrounding cells are taken into account to determine the event time.

The center of gravity for each cluster is calculated to determine the cluster position. The position is corrected using a functional dependency found with detailed Monte Carlo studies. The cluster energy is corrected in order to account for effects of different distances of the shower core from the anode. For overlapping clusters a correction taking into account the energy sharing between the clusters is applied. As the high voltage has been lower than the design value, space charge can accumulate during a burst. A small correction is applied for this effect. For a cluster within a radius of 20 cm of the beam hole, or within a distance of 13 cm to the dead column, a correction for the lost energy is applied.

With the NA48 Liquid Krypton calorimeter 1997 an energy resolution of

$$\frac{\sigma(E)}{E} = \frac{3.2\%}{\sqrt{E}} \oplus \frac{125\ \text{MeV}}{E} \oplus 0.5\% \tag{7.3}$$

has been achieved.

From all photon candidates all possible combinations of four clusters is built. For each combination the following quantities are calculated:

1. The kaon energy

$$E_{\text{K}} = \sum_{i=1}^{4} E_i. \tag{7.4}$$

2. The distance D from the LKR to the decay vertex is reconstructed using the position of the four cluster. The formula is:

$$D = \frac{1}{M_{\text{K}}} \sqrt{\sum_{i,j} E_i\, E_j\, r_{ij}^2}, \tag{7.5}$$

using the nominal kaon mass M_{K} as hypothesis.

3. The invariant mass of the two photon pairs (i, j) and (k, l) is determined using the distance D from equation (7.5) as parameter. For each possible combination of clusters i, j, k, l a χ^2 variable is calculated:

$$\chi_m^2 = (m_{ij} - m_\pi)^2 + (m_{kl} - m_\pi)^2. \tag{7.6}$$

The combination with the lowest χ_m^2 is chosen for further event selection. This χ^2 variable is only used in the event selection of the Neutral Filter within the Level 3/Real Time Reconstruction (see Section 5.3). For the final analysis a selection based on the quantity R_{ellipse} (see equation (7.12)) is used.

7.3 Common Event Selection Criteria

As a general principle selection criteria have to be as identical as possible for K_{S} and K_{L} decays. If conceivable also the requirements for the charged and the neutral decay mode should be identical. In this Section selection criteria which affect both, the charged and the neutral decays, are discussed.

The kaon energy range for this analysis has been restricted to be from 70 GeV to 170 GeV. This ensures that the kaon production spectra are comparable and that systematic effects, *e.g.* the non-linearity of the calorimeter response, are small.

As described in Section 4.3, the upstream end of the fiducial region is defined by the K_{S} anti-counter. No hit in the AKS within ±3 ns of the event time is allowed. The AKS position for charged and neutral decays differs by 21 mm, as the converter is used for neutral decays, and the counter is used for charged decays. Therefore the vertex of K_{L} decays is required to be downstream of the converter for $K_{\mathrm{L}} \to \pi^0\pi^0$ decays and downstream of the counter for $K_{\mathrm{L}} \to \pi^+\pi^-$ decays. Both, K_{S} and K_{L} decays, are required to have a proper time of flight $\tau < 3.5\tau_{K_{\mathrm{S}}}$. Again, converter and counter are used to calculate the lifetime for neutral and charged decays, respectively. This ensures that the length of the fiducial volume is identical.

For K_{L} decays a weight w_i is applied to event i according to the ratio of the decay distribution function $F(\tau)$ for K_{S} and K_{L} decays:

$$w_i = \frac{F(\tau_S)}{F(\tau_L)}, \tag{7.7}$$

$$F(\tau) = \mathrm{e}^{-\tau/\tau_{K_{\mathrm{S}}}} + |\eta|^2\mathrm{e}^{-\tau/\tau_{K_{\mathrm{L}}}} + 2|\eta|D(p)\mathrm{e}^{-\tau(1/\tau_{K_{\mathrm{S}}}+1/\tau_{K_{\mathrm{L}}})/2}\cos(\Delta m\tau + \phi), \tag{7.8}$$

where $\tau_{S,L}$ is the kaon lifetime seen from the K_{S} or K_{L} target, respectively. τ_i denotes the reconstructed proper lifetime of the kaon for event i. The values for $\eta, \Delta m$, and ϕ are taken from the Particle Data Group [PDG98]. D(p) parameterizes the $K_{\mathrm{S}}/K_{\mathrm{L}}$ production ratio as function of the kaon energy and and has been measured by the NA31 collaboration [Ber97b]. The effect of the interference term in equation (7.8) is a small contribution above 140 GeV (see Figure 23).

The weight w_i is normalized such that it is equal to 1.0 at the position of the AKS converter. Using a maximum lifetime of 3.5, the loss of statistical power due to the weighting is a factor of 1.4. The lifetime distribution of K_{L} decays after weighting is equal to the one of K_{S} decays, as shown in Figure 24.

As described in Section 4.4, an overflow condition in the chamber readout can lead to the loss of a close by $K \to \pi^+\pi^-$ event. As can be seen in Figure 25a, charged events may be lost when an overflow within a time window of ±312.5 ns around the event time occurs. Because of the overflow the information of at least one of the DCH planes is missing. This can lead to mis-reconstruction of tracks and vertices by the Massbox or by the L3/RTR.

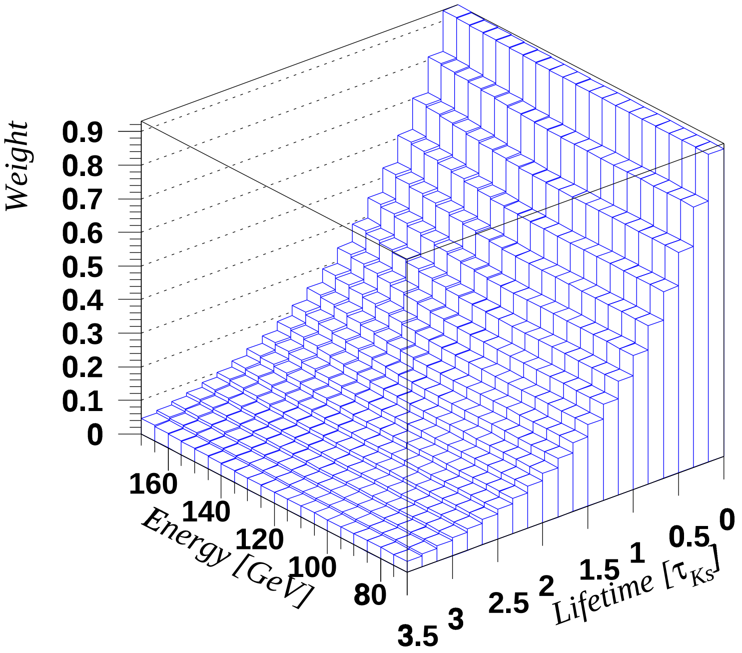

Figure 22: Weight applied to K_L decays as function of energy and lifetime. The interference term leads to a small correction at higher energies.

Therefore a charged event with overflow may not be accepted. For neutral events the reset of a FIFO does not lead to a loss of events (Figure 25b). However, in order to symmetrize this effect, charged and neutral events are rejected if there is one or more DCH planes in overflow within this time window. In case of the neutral events this leads to a loss of 20.4% of the events.

To confirm that this selection does not introduce a bias between charged and neutral events, the overflow rate outside the window is compared. For this comparison the misidentification of K_L events due to accidental hits in the Tagger is determined separately. Both effects, the overflow events and the accidental Tagger hits, are dependent on the proton rate. For neutral overflow events the probability for a proton to hit a shifted tagging window is 1.4 percentage points higher than for all neutral events. The corrected overflow rates are given in Table 7. The double ratio built from the fraction of overflow events is 0.996 ± 0.008, thus compatible with 1.

A much smaller effect is due to the Massbox dead-time. In case of high rate and complicated events the Massbox is not able to process all L1 triggers.

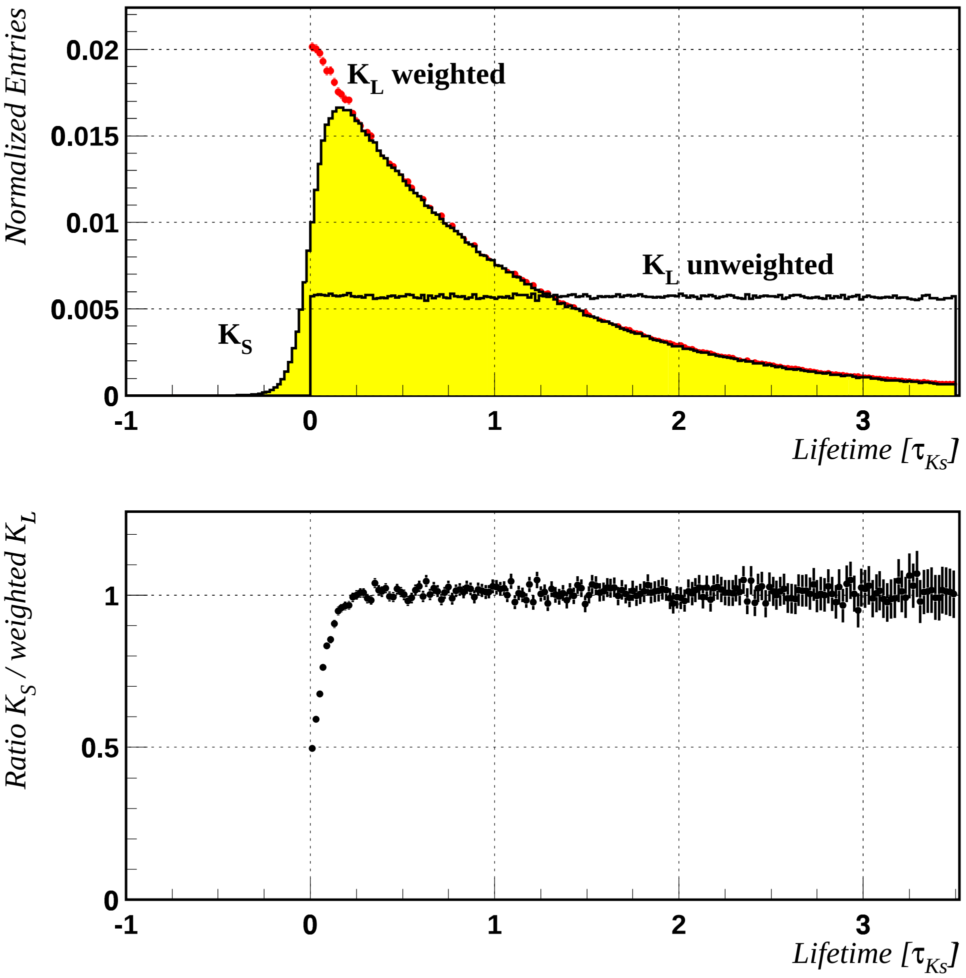

Figure 23: Normalized lifetime distributions for K_{S} and weighted and unweighted K_{L} decays. Shown is the charged decay mode. After weighting, the lifetime distributions for K_{S} and K_{L} decays become equal for $\tau > 0.2\tau K_{\mathrm{S}}$, as shown by the ratio in the lower plot.

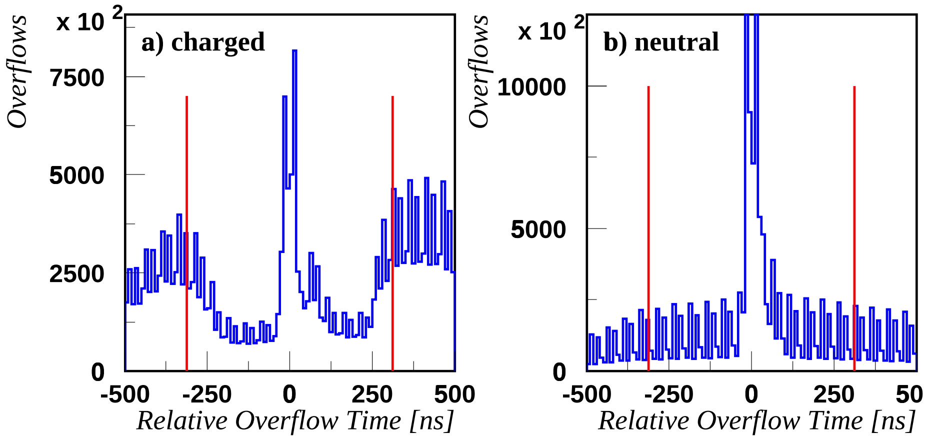

Figure 24: Overflow time with respect to the event time for charged and neutral events. Within a time window of ±312.5 ns charged events are lost because of a close-by overflow. Events within this window are not selected in both decay modes.

	charged	neutral
K_S	0.0981 ± 0.0002	0.0989 ± 0.0004
K_L	0.1026 ± 0.0003	0.1039 ± 0.0006

Table 7: *Fraction of events with overflow condition outside the relevant time window of* ±312.5 *ns.*

In this case the Massbox sends a signal which is recorded by the PMBs. In the analysis this dead-time is artificially applied to neutral events to symmetrize the effect, leading to a rejection of 1.08% of the neutral events.

To further symmetrize the acceptance, fiducial selection criteria applied to neutral events are also applied to charged events. Clusters and tracks within a radius of 2 cm of a dead cell or the dead column of the LKR are rejected. Clusters and tracks must lay within an octagon of 110 cm inner radius at the LKR.

Charged and neutral events are required to have the center of gravity (COG) at the position of the LKR within a radius of 10 cm around the K_L beam axis. For a neutral event the energy weighted mean of the cluster positions is used. For charged events the tracks in front of the magnet are extrapolated to the LKR and, again, the energy weighted mean of the trajectories is computed. The selection criteria are summarized in Table 8.

Kaon Energy	70 GeV $< E_K <$ 170 GeV
Lifetime	$c\tau < 3.5\ c\tau_{K_\mathrm{S}}$
Lifetime	$c\tau > 0$ for K_L events
AKS	±3 ns around the event time
Center of gravity	COG $<$ 10 cm
Dead LKR cells	2 cm around a dead cell
Dead column	±3.94768 cm around the dead column
Overflow time	±312.5 ns around the event time

Table 8: *Summary of the event selection criteria common to the charged and the neutral final state.*

7.4 The Selection of Charged Events

A decay vertex is required to consist of a positive and negative track within 6 ns of one another. The closest distance of approach (CDA) of those two tracks must be lower than 3 cm. Each track must have a momentum of at least 10 GeV. The event time must be within 20 ns of the trigger time to exclude events where the trigger was issued on an after-pulse of the Q_x signal.

In order to reject K_{e3} decays, electrons are identified by the ratio of reconstructed energy in the LKR calorimeter E and the measured track momentum p. Both tracks have to fulfill $E/p < 0.8$ (see Figure 26). While only about 4% of $\pi^+\pi^-$ events are lost (Figure 26c), the background is reduced to the level of 10^{-3} (Figure 26d).

Another requirement that reduces the background from semi-leptonic 3-body decays is based on the transverse momentum. A new kinematic variable ${p_\mathrm{t}}'$ is defined, which has a similar resolution for K_S and K_L decays. ${p_\mathrm{t}}'$ is defined as

$$ {p_\mathrm{t}}' = |\vec{p_1} + \vec{p_2}| \cdot \Theta, \tag{7.9} $$

where Θ is the (small) angle between the reconstructed momentum $\vec{p} = \vec{p_1} + \vec{p_2}$ and the line between target and intersection point D of the momentum $\vec{p}$ with drift chamber 1 (see Figure 27). In the ideal case Θ is equal to 0 for a two body decay, as the kaon momentum points in the direction of the target - vertex line. With this definition the resolution of ${p_\mathrm{t}}'$ is nearly independent of the target position and the beam divergence. In contrast to that, the variable p_t in its usual definition has a better resolution for K_L decays than for K_S decays. The reason is that the beam divergence is smaller for the beam derived from the K_L target, as the distance between target and defining collimator is larger.

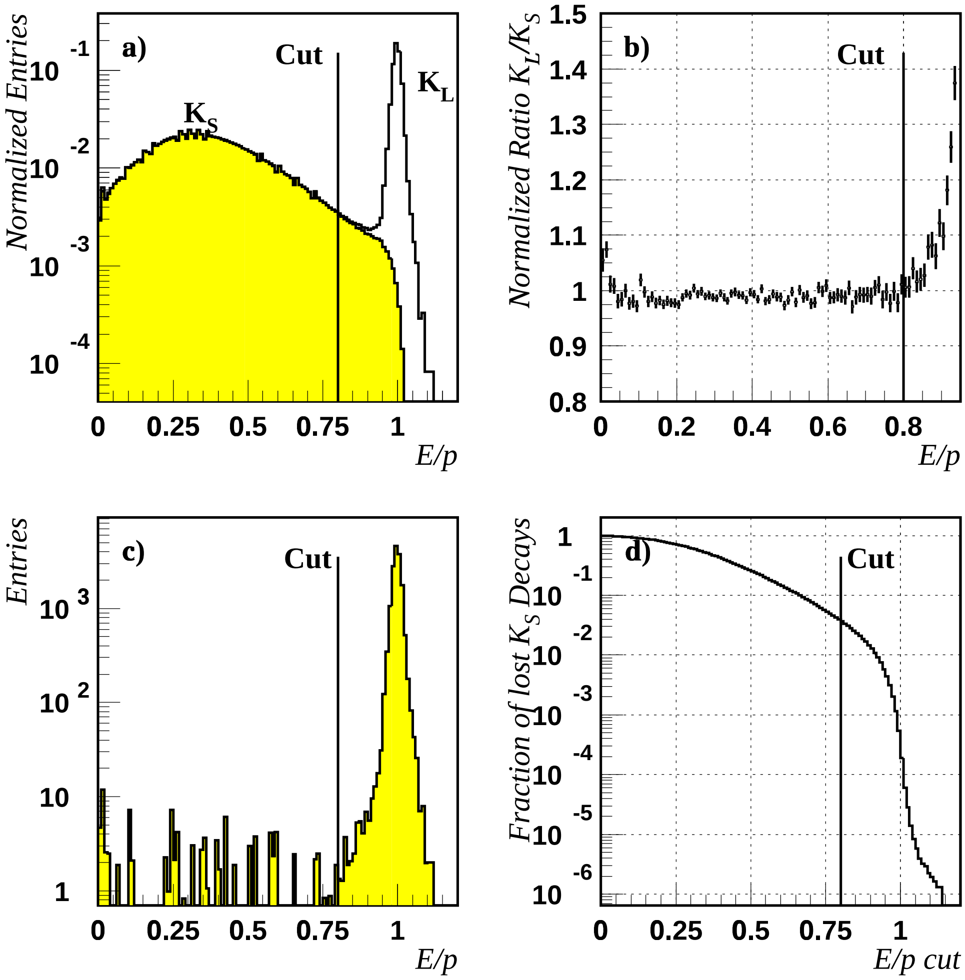

Figure 25: E/p selection to reject K_{e3} background. a) E/p distribution for vertex identified K_S and K_L decays. All other selection criteria are applied. For K_L decays the electron peak at $E/p \sim 1$ is visible. The distributions are normalized to the area defined by $E/p < 0.7$. b) Normalized ratio of the K_S and K_L E/p distribution. c) E/p distribution for K_L decays after subtraction of the normalized K_S distribution. d) Fraction of lost K_S decays as function of the E/p selection.

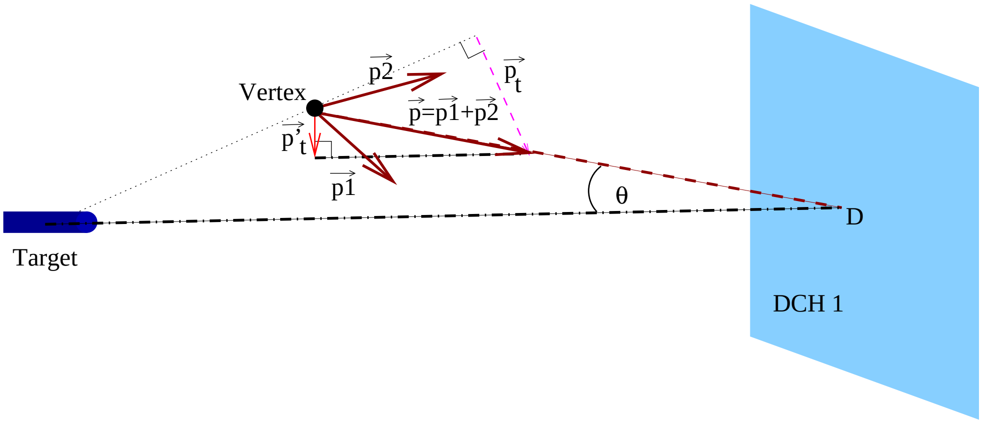

Figure 26: Definition of the new kinematic variable ${p_{\rm t}}'$. The resolutions for $K_{\rm S}$ and $K_{\rm L}$ decays are identical for ${p_{\rm t}}'$, while the resolution in $p_{\rm t}$ is better for $K_{\rm L}$ decays due to the different target position.

${p_{\rm t}}'$ is calculated with respect to the target, which is selected according to the decay vertex position: $K_{\rm S}$ and $K_{\rm L}$ can be unambiguously distinguished by the y-vertex position (see Figure 38 in section 8.4.2 and text there). Charged events with ${p_{\rm t}}'^2 > 200$ MeV^2/c^2 are rejected as background events. Event losses of about 8×10^{-4} are caused mainly by a mis-reconstructed vertex position and are identical for $K_{\rm S}$ and $K_{\rm L}$.

In order to further suppress background from $K_{\mu 3}$ decays, events with an identified muon are rejected. If one of the tracks can be associated to a muon hit within 4 ns of the event time, the event is not accepted.

A requirement on the momentum asymmetry between the two pions is used to reject events with one pion close to the beam pipe. The asymmetry parameter A is defined as

$$A = \frac{|p_1 - p_2|}{p_1 + p_2}. \tag{7.10}$$

Since a two body decay is observed, A reflects the decay orientation in the kaon rest frame. Events with large momentum asymmetry have one track close to the beam axis. This relation is energy dependent, as the opening angle of the tracks shrinks with increasing kaon energy. Figure 28a shows this behavior for 3 different energies. Selected events must have $A < 0.62$ and $A < 1.08 - 0.0052 \times E_K$, where E_K is the kaon energy in GeV (Figure 28b). Using this selection criteria, events with tracks close to the beam pipe are rejected. In this way it is not necessary to have a very detailed Monte Carlo modeling of tracks close to the beam pipe. The event selection is instead

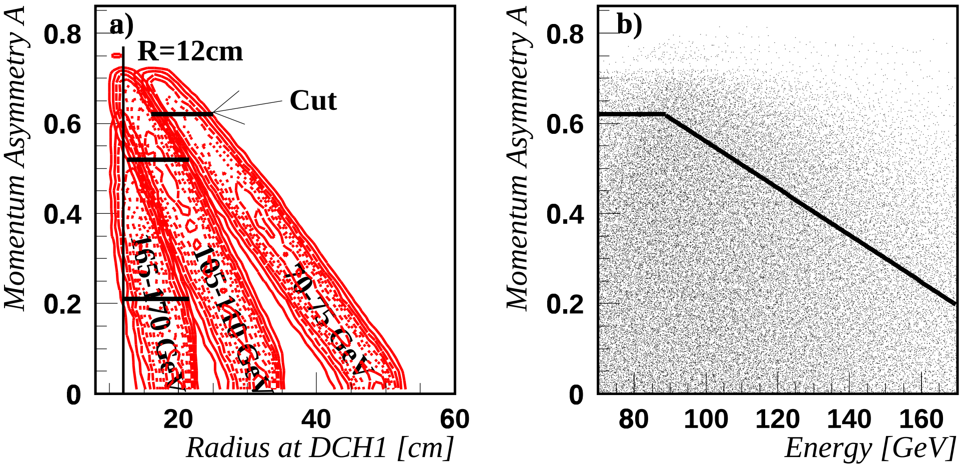

Figure 27: Momentum asymmetry A of $\pi^+\pi^-$ decays. a) The momentum asymmetry versus the radius at drift chamber 1 is shown for 3 different energies. In order to reject events with one track close to the beam pipe, an energy dependent selection on A (marked by lines in the plot) is done. The radius $R = 12$ cm is marked as well. b) The selection is $A < 0.62$ and $A < 1.08 - 0.0052 \times E_K$, marked by the line in the plot. The rejection of events with reconstructed Λ mass is seen as depleted region at $A = 0.73$.

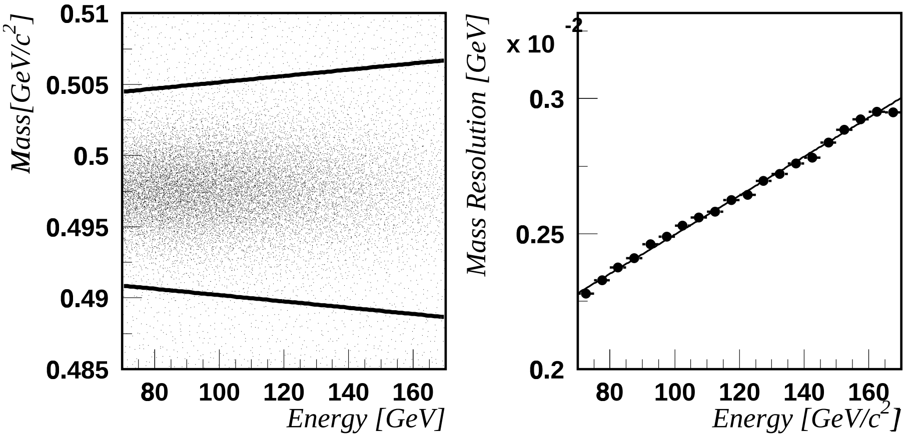

Figure 28: Energy dependence of the resolution of the reconstructed kaon mass.

based on the decay orientation of the kaon, which is easy to model in the Monte Carlo simulation.

The requirement on A in addition removes Λ and $\bar{\Lambda}$ decays coming from the K_S-target. This is seen as depleted region in Figure 28b at high asymmetries A. In any case, $\Lambda \rightarrow p\pi$ decays with reconstructed Λ mass between 1.112 GeV $< m_\Lambda <$ 1.119 GeV are rejected.

The fiducial volume is defined by the requirement that no track must be within a radius of 12 cm from the centre of the beam pipe at the position of drift chambers 1, 2, and 4 and within a radius of 15 cm at the LKR position. Furthermore, no track must be within a square of 12.5 cm width around the center of the beam pipe at the muon veto position.

Selected events must have a reconstructed kaon mass within $3\sigma_m$ around the nominal kaon mass of $m_K = 0.497672$ GeV [PDG98]. The mass resolution depends on the momentum resolution, which is energy dependent. Therefore σ_m is parameterized as function of the energy (see Figure 29). From data one obtains:

$$\sigma_m = 1.755 \times 10^{-3} + 7.372 \times 10^{-6} \cdot E_K[\mathrm{GeV}] \qquad (7.11)$$

For a 100 GeV kaon this translates into the requirement 495.180 MeV $< m_{\pi\pi} <$ 500.164 MeV.

Selection criteria for the charged final state are summarized in Table 9.

Track time difference	$\|t_1 - t_2\| < 6.0$ ns
CDA	CDA < 3.0 cm
Track momentum	$p_{\mathrm{Track}} > 10$ GeV
Trigger time	$\|t_{\mathrm{Event}} - t_{\mathrm{Trigger}}\| < 20$ ns
E/p	$E/p < 0.8$
p_{t}'	$p_{\mathrm{t}}'^2 < 200\ \mathrm{MeV}^2/\mathrm{c}^2$
Λ decays	$1.112\ \mathrm{GeV} < m_{p\pi} < 1.119\ \mathrm{GeV}$
MUV time	±4 ns around event time
Fiducial requirements	12 cm at chambers 1, 2, and 4 15 cm at LKR 12.5 cm at MUV
Momentum asymmetry	$A < 0.62$ and $A < 1.08 - 0.0052 \times E_K$
Mass	$\pm 3\ \sigma_{m_{\pi\pi}}$, $\sigma_{m_{\pi\pi}} = 1.755 \times 10^{-3} + 7.372 \times 10^{-6} \cdot E_K[\mathrm{GeV}]$

Table 9: Summary of the selection criteria for the charged final state.

7.5 The Selection of Neutral Events

For the selection of a neutral event, the reconstructed γ energy must be between $3\ \mathrm{GeV} < E_\gamma < 100\ \mathrm{GeV}$. This selection ensures that the energy resolution is sufficiently good, while non-linear effects of the calorimeter energy response are still small. The distance between two cluster has to exceed 10 cm to avoid problems in the reconstruction when clusters overlap and share energy. The time of the clusters must be no more than 5 ns from the mean time. No accidental cluster with energy greater than 1.5 GeV within a 3 ns time window around the event is allowed. This requirement rejects background from $3\pi^0$ decays, as many of those events have an additional cluster in time with the event. The condition of a minimum energy of 1.5 GeV ensures that $K \to \pi^0\pi^0$ decays with shower fluctuations are not lost.

As described in Section 7.2, clusters are paired, and for each pair the invariant π^0 masses m_1 and m_2 are calculated. As the kaon mass is used as constraint to calculate the pion masses, m_1 and m_2 are not independent. The distribution of m_2 versus m_1 (Figure 30) exhibits an elliptical shape. To take this into account, the selection is based on a χ^2 variable R_{ellipse}:

$$R_{\mathrm{ellipse}} = \left(\frac{(m_1 + m_2)/2 - m_{\pi^0}}{\sigma_+}\right)^2 + \left(\frac{(m_1 - m_2)/2}{\sigma_-}\right)^2 . \qquad (7.12)$$

$\sigma_\pm$ denote the resolution on the quantities $(m_1 \pm m_2)/2$ and are functions of the lowest photon energy (Figure 31). These functions are obtained from

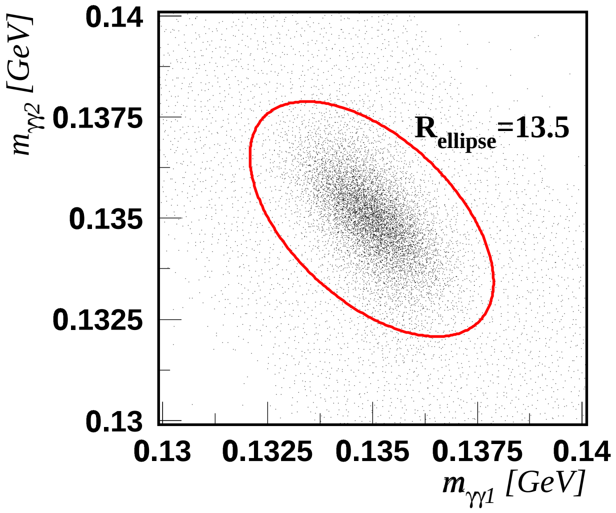

Figure 29: Distribution of the invariant $\gamma\gamma$ masses for K_S decays. The ellipse marks the selection criteria $R_{\text{ellipse}} = 13.5$.

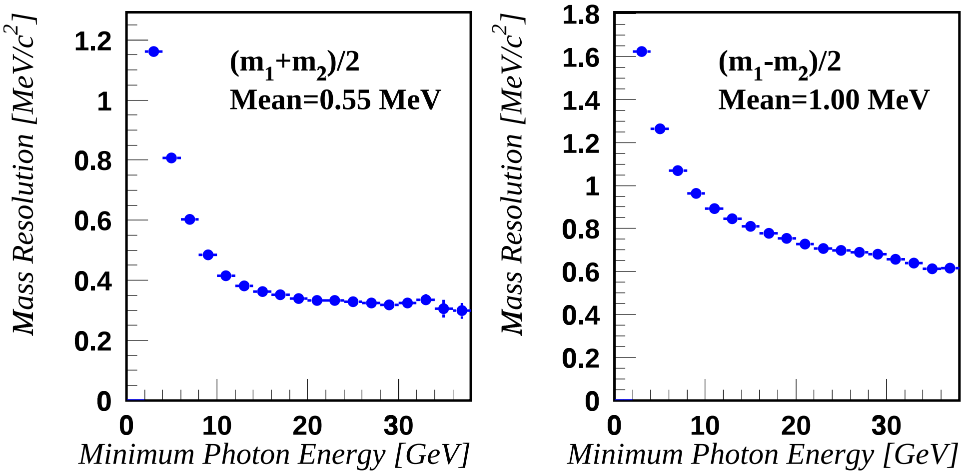

Figure 30: Resolution (1 standard deviation) of $(m_1+m_2)/2$ and $(m_1-m_2)/2$ as function of the lowest photon energy.

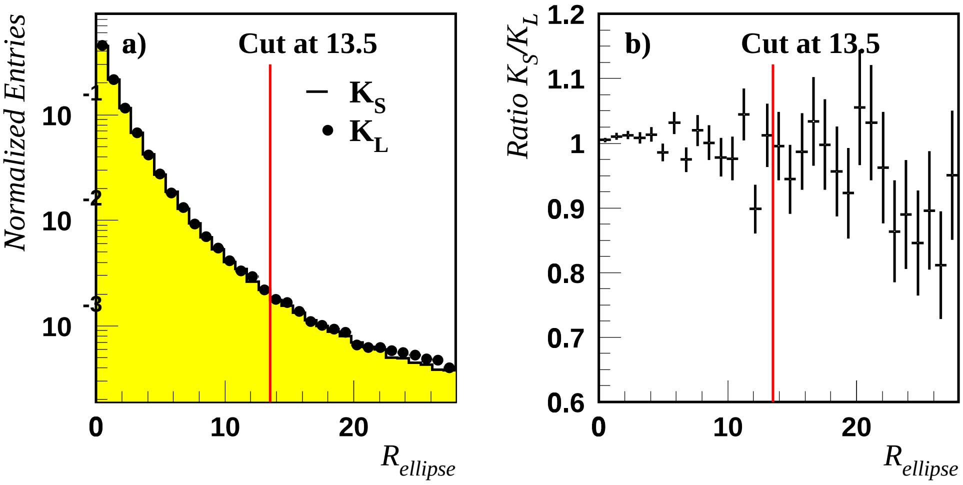

Figure 31: a) Normalized number of K_{S} and K_{L} decays as function of R_{ellipse}. See also Figure 50a on page 93. b) Ratio of $K_{\mathrm{S}}/K_{\mathrm{L}}$ decays as function of R_{ellipse}. Events with $R_{\text{ellipse}} < 13.5$ are selected.

the data. The mean resolution on $(m_1 \pm m_2)/2$ is 0.55 MeV and 1.00 MeV, respectively. Constant values of R_{ellipse} for different masses m_1, m_2 are ellipses in Figure 30. A selected event is required to have $R_{\text{ellipse}} < 13.5$ (see Figure 32).

Photon Energy	3 GeV $< E_\gamma <$ 100 GeV
Cluster separation	$d_{ij} >$ 10 cm
Cluster times	within 5 ns of the mean
Accidental cluster with $E >$ 1.5GeV	none within ±3 ns of the event time
R_{ellipse}	$R_{\text{ellipse}} < 13.5$
Event time quality	$\geq$ 5 cells required

Table 10: Summary of the selection criteria for the neutral final state.

8 The Double Ratio and Corrections

8.1 The Unbiased Estimator and the Error Calculation

The analysis is performed in 20 energy bins. Each of these 20 measurements are statistically independent. An unbiased estimator (log-R estimator) is chosen to combine the measurements R_i to a global result R. The error of a ratio a/b is given by

$$\sigma\left(\frac{a}{b}\right) = \frac{a}{b}\sqrt{\frac{\sigma^2(a)}{a^2} + \frac{\sigma^2(b)}{b^2}}, \tag{8.1}$$

thus it is dependent on the magnitude of the ratio a/b itself. In contrast, the error of the logarithm of the ratio $\log(a/b)$ does not depend on the magnitude:

$$\sigma\left(\log\frac{a}{b}\right) = \sqrt{\frac{\sigma^2(a)}{a^2} + \frac{\sigma^2(b)}{b^2}}. \tag{8.2}$$

The log-R estimator is the weighted average of the logarithm of the R_i values for each energy bin i:

$$\bar{L} = \frac{\sum \left(L_i/\sigma^2_{L_i}\right)}{\sum \sigma^2_{L_i}}, \tag{8.3}$$

$$\sigma(\bar{L}) = \left(\sum \frac{1}{\sigma^2_{L_i}}\right)^{-\frac{1}{2}}. \tag{8.4}$$

L_i is the logarithm of the double ratio (equation (3.1)) for energy bin i:

$$L_i = \log R_i = \log N^{00}_{L,i} - \log N^{00}_{S,i} - \log N^{+-}_{L,i} + \log N^{+-}_{S,i}. \tag{8.5}$$

This estimator has two advantages:

1. A naïve fit underestimates R, as data points statistically fluctuating to smaller values have smaller errors as well. The log-R estimator does not have this problem.

2. The errors of the 20 measurements can be combined easily, in contrast to a log-likelihood fit.

In the error calculation the weighting of the events must be taken into account. The uncertainty of a weighted number of events $N_w = \sum_i w_i$ is given by

$$\sigma(N_w) = \sqrt{\sum_i w_i^2}. \tag{8.6}$$

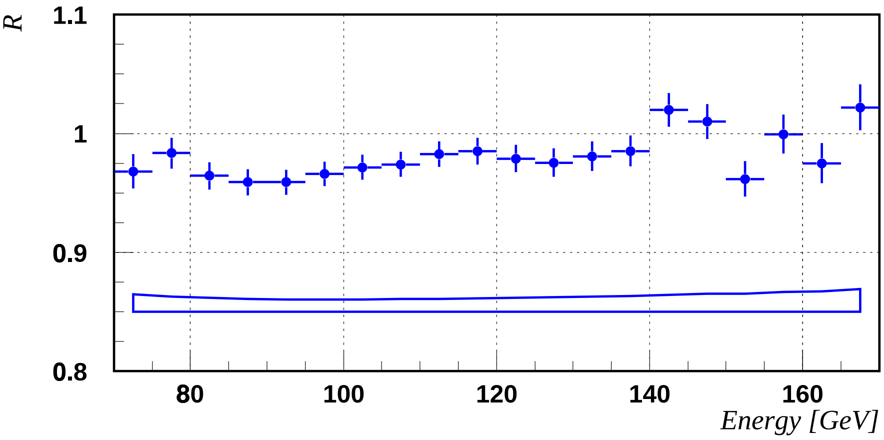

Figure 32: R values for each energy bin without corrections. The uncertainty is also visualized by the band.

In case of unweighted events ($w_i = 1$ for all i), one obtains the well known Poissonian uncertainty $\sigma(N_w) = \sqrt{N_w}$. When an efficiency ϵ is calculated, binomial statistics with weighted events is used:

$$\epsilon = \frac{n_w}{n_w + m_w}, \tag{8.7}$$

$$\sigma(\epsilon) = \sqrt{\frac{m_w^2 \sigma(n_w)^2 + n_w^2 \sigma(m_w)^2}{(n_w + m_w)^4}}, \tag{8.8}$$

where n_w is the number of efficient events, and m_w is the number of inefficient events. For unweighted events this reduces to:

$$\sigma(\epsilon) = \sqrt{\frac{\epsilon(1-\epsilon)}{N}}, \tag{8.9}$$

with $N = n_w + m_w$.

8.2 The Raw Double Ratio

The event numbers in the four decay modes, after applying the selection criteria described in the previous Section, are listed in Table 11. Figure 33 shows the raw values of the double ratio R for each of the 20 energy bins. Combining the 20 values using the log-R estimator yields:

$$R_{\text{raw}} = 0.9779 \pm 0.0028 \; (stat). \tag{8.10}$$

	K_S	K_L	K_L weighted
$\pi^+\pi^-$	2218800	952699	267173.3
$\pi^0\pi^0$	1040573	435298	122441.0

Table 11: Event numbers of the four decay modes after the final event selection.

The statistical error is dominated by the weighted number of $K_L \to \pi^0\pi^0$ decays. The uncertainty is a factor of 1.4 larger than for unweighted events.

In the following Sections systematic corrections to the raw value of R and their uncertainties are discussed.

8.3 The Energy Scale

For neutral decays the energy scale and the distance scale are related by equation (7.5). The distance of the decay vertex from the calorimeter is calculated using the reconstructed photon energies. The beginning of the decay volume is defined by the AKS counter and is thus independent of the neutral reconstruction. Therefore one can use the known position of the AKS to fix the global energy scale and to check the linearity of the energy measurement.

At the position z_{AKS} of the AKS a sharp edge, smeared by the z-vertex

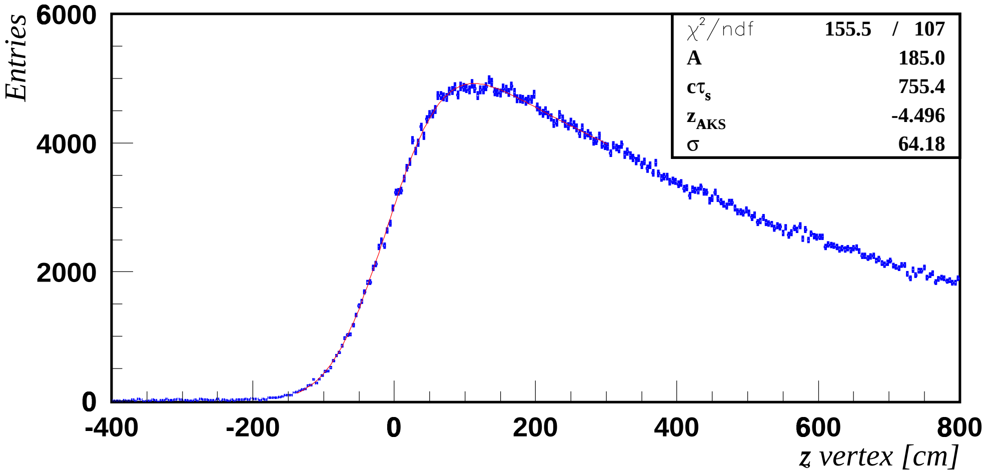

Figure 33: Fit of the AKS position for neutral K_S decays.

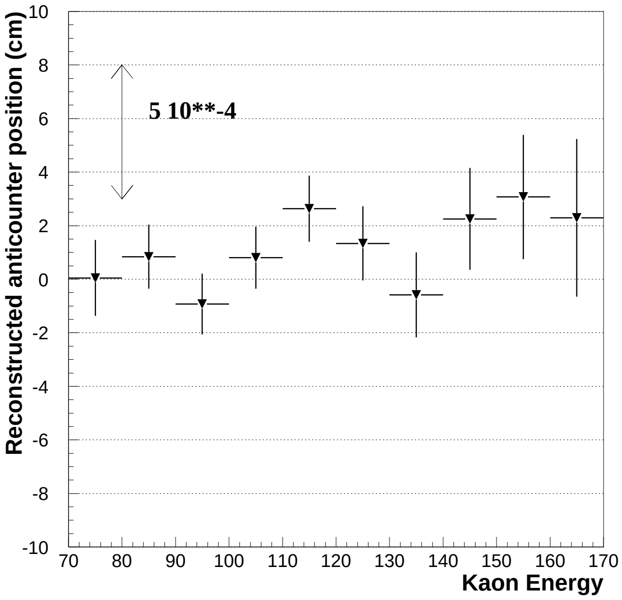

Figure 34: Fit of the AKS position for neutral decays for different energies. A shift of the reconstructed anti-counter position of 5 cm, as idicated in the figure, corresponds to a change in R of 5×10^{-4}.

resolution, is seen (Figure 34). Downstream of the AKS the rate decreases exponentially according to the K_S decay constant. For the z-vertex resolution a Gaussian distribution is assumed. Therefore the convolution

$$f(z) = A \cdot \int_{z_{\mathrm{AKS}}}^{\infty} \mathrm{e}^{\frac{z'-z_{\mathrm{AKS}}}{c\tau_S}} \cdot \mathrm{e}^{-\frac{(z-z')^2}{2\sigma^2}} \mathrm{d}z' \tag{8.11}$$

is used to fit the measured z-vertex distribution. The fit result of z_{AKS} is compared to the fitted AKS position from Monte Carlo events. The resulting difference is translated into an energy scale factor. The energy scale-factor used in this analysis is 1.0024. Systematic uncertainties of the energy scale are discussed in the rest of this Section.

The AKS fit is done for 10 energy bins. Figure 35 shows that the global scale is stable within 5 cm over the full energy range. Given the distance of the AKS to the LKR, this corresponds to a relative value of $\pm 5 \times 10^{-4}$, which is also the resulting uncertainty on R. The global scale is also checked using the η-run at the end of the data taking period [Giu99]. A hydrogen target is positioned 634.4 cm downstream of the K_S target. A π^- beam is

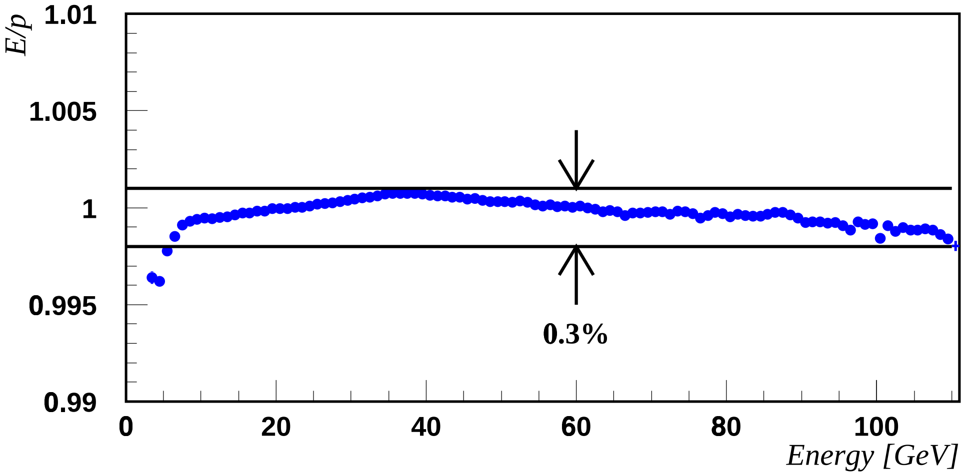

Figure 35: Linearity of the reconstructed LKR energy. The E/p value for electron clusters coming from K_{e3} decays varies within 0.3% over the energy range 10 GeV- 100 GeV.

used to produce π^0 and η, which decay subsequently into 2 or 6 photons. The reconstructed position of the decay vertex is compared to the target position. This measurement coincides with the global scale found with the AKS fit within $\pm 5 \times 10^{-4}$.

The uncertainty in the transverse energy scale is determined using K_{e3} events. The projected impact position of the electron is compared to the reconstructed cluster position. This leads to an uncertainty of $\pm 3 \times 10^{-4}$ in the transverse energy scale.

An additional uncertainty of $\pm 3 \times 10^{-4}$ comes from residual calorimeter non-uniformities measured with π^0, η, and K_{e3} decays.

The linearity of the calorimeter is also checked using K_{e3} decays. The momentum of the electrons is compared to the reconstructed energy of a cluster. Including an offset of $\sim$ 20 MeV, which is due to energy loss in the material in front of the calorimeter, the deviation from linearity varies within a range of 0.3% (Figure 36). Additional checks are done using π^0 and η decays. The corresponding uncertainty in R is $\pm 9 \times 10^{-4}$.

Residual uncertainties in the energy measurement due to space charge effects, energy sharing, and incidence angle of the photon are estimated to be $\pm 4 \times 10^{-4}$ on R.

The uncertainties in R add up to $\pm 12 \times 10^{-4}$. Table 12 summarizes the different contributions.

The uncertainty in the charged vertex reconstruction is affected by uncertainties in the detector geometry. In addition the magnetized vacuum tank of the decay region produces a magnetic field, diverting the tracks. Residual effects are estimated to add $\pm 5 \times 10^{-4}$ to the uncertainty of R.

	Uncertainty on R [$\times 10^{-4}$]
global energy scale	5
transverse scale	3
calorimeter uniformity	3
calorimeter linearity	9
energy measurement	4
Sum	12
charged vertex reconstruction	5

Table 12: Different contributions to the uncertainty in the energy scale.

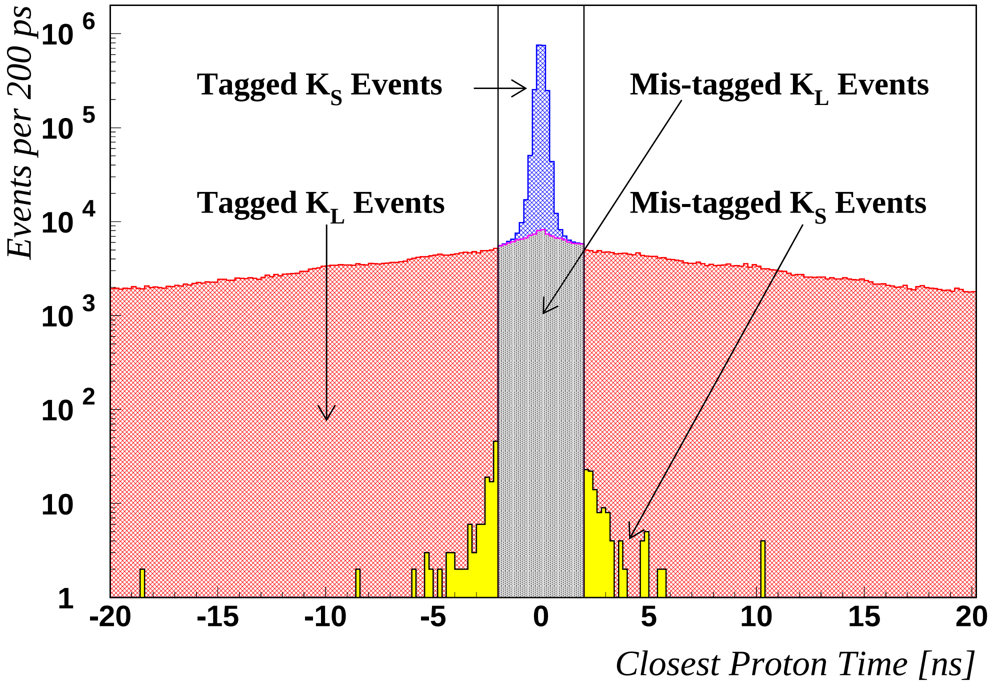

Figure 36: Time of the closest proton hit in the Tagger with respect to the event time for selected K_S and K_L events. The events are tagged by the y-position of the decay vertex. The tagging window of ±2 ns is marked by the two lines. Correctly tagged K_S events are shown on top of the K_L distribution, mis-tagged K_S events are shown at the bottom. K_L events with an accidental proton hit in the time window are mis-tagged.

8.4 Tagging Efficiency and Dilution

8.4.1 Introduction

The Tagger is used to distinguish between K_S and K_L decays. An event with a proton hit in the Tagger, which is within ±2 ns of the reconstructed event time (tagging window), is defined as K_S decay. Events without a reconstructed proton hit in the tagging window are defined as K_L events. In this Section systematic effects due to misidentification of the kaon type are discussed.

In the charged decay mode the true kaon type can be identified by the vertex position (vertex tag). Figure 37 shows the closest proton hit time in the Tagger with respect to the event time for events identified by the vertex tag. If the tagging is inefficient, true K_S decays (N_S^T) are misidentified as

$K_{\rm L}$ events. This will lower the number of measured $K_{\rm S}$ events. On the other hand accidental activity in the Tagger leads to a misidentification of true $K_{\rm L}$ events ($N_{\rm L}^{\rm T}$) as $K_{\rm S}$ events. This effect is coined "tagging dilution", or shortly "dilution". When ϵ denotes the tagging efficiency and $\alpha_{{\rm L}S}$ the fraction of $K_{\rm L}$ events that are misidentified ($K_{\rm L} \to K_{\rm S}$ transitions), the measured event numbers $N_{\rm S}^{\rm M}$ and $N_{\rm L}^{\rm M}$ relate to the true values as:

$$N_{\rm S}^{\rm M} = \epsilon N_{\rm S}^{\rm T} + \alpha_{{\rm L}S} N_{\rm L}^{\rm T}, \tag{8.12}$$

$$N_{\rm L}^{\rm M} = (1-\epsilon) N_{\rm S}^{\rm T} + (1-\alpha_{{\rm L}S}) N_{\rm L}^{\rm T}. \tag{8.13}$$

Using these relations one obtains for the true number of events:

$$N_{\rm S}^{\rm T} = \frac{1-\alpha_{{\rm L}S}}{\epsilon-\alpha_{{\rm L}S}} N_{\rm S}^{\rm M} - \frac{\alpha_{{\rm L}S}}{\epsilon-\alpha_{{\rm L}S}} N_{\rm L}^{\rm M}, \tag{8.14}$$

$$N_{\rm L}^{\rm T} = \frac{\epsilon}{\epsilon-\alpha_{{\rm L}S}} N_{\rm L}^{\rm M} - \frac{1-\epsilon}{\epsilon-\alpha_{{\rm L}S}} N_{\rm S}^{\rm M}. \tag{8.15}$$

To correct for dilution effects, the different selection criteria for $K_{\rm S}$ and $K_{\rm L}$ decays are taken into account. For $K_{\rm S}$ decays the beginning of the decay region is defined by the AKS counter, while for $K_{\rm L}$ decays it is defined by selecting events with reconstructed position downstream of the nominal AKS position.

To calculate the true number of events according to equations (8.14) and (8.15), events with selection criteria belonging to the opposite kaon type have to be used. The $N_{\rm L}^{\rm M}$ events on the right hand side of equation (8.14) are unweighted and have no lifetime cut. The $N_{\rm S}^{\rm M}$ events on the right hand side of equation (8.15) have to fulfill the criteria $c\tau > 0$.

8.4.2 Tagging Efficiency and Dilution in the Charged Decay Mode

The dilution factor $\alpha_{{\rm L}S}$ and the tagging inefficiency ($K_{\rm S} \to K_{\rm L}$ transitions) $\alpha_{{\rm S}L} = 1-\epsilon$ can be measured in the charged decay mode, as the y-position of the vertex unambiguously identifies $K_{\rm S}$ and $K_{\rm L}$ decays. $K_{\rm S}$ decays are defined by the requirement $y_{\rm vertex} > 4.2 * (1 - z_{\rm vertex}/z_{\rm LKR})$. Figure 38 shows the x-y-projection and the y-z-projection of the vertex distribution for $K \to \pi^+\pi^-$ decays. The results are:

$$\alpha_{{\rm L}S}^{+-} = 0.11205 \pm 0.00029, \tag{8.16}$$

$$\alpha_{{\rm S}L}^{+-} = (1.5 \pm 0.1) \times 10^{-4}, \tag{8.17}$$

leading to a correction to R of

$$\Delta R = +59 \times 10^{-4}. \tag{8.18}$$

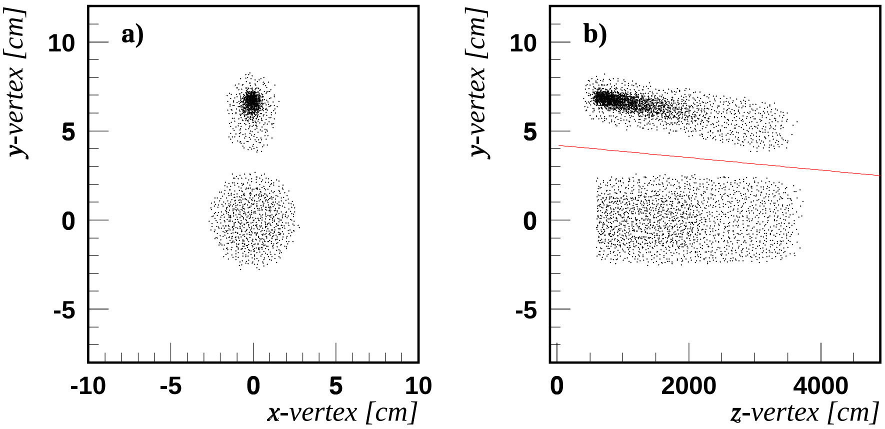

Figure 37: a) x-y-projection and b) y-z-projection of the vertex distribution for $K \to \pi^+\pi^-$ decays. K_{S} decays can be clearly distinguished from K_{L} decays by the y-position of the vertex.

This correction has no uncertainty, as the measurement is exact in case of the charged decay mode. However, the uncertainty on $\alpha^{+-}_{\mathrm{L}S}$ is taken into account when calculating the difference in dilution to the neutral decay mode.

8.4.3 Dilution in the Neutral Decay Mode

As different sub-detectors and different triggers are used to measure charged and neutral decays, $\alpha_{\mathrm{L}S}$ can in principle be different for the two decay modes. As it is not possible to distinguish K_{S} from K_{L} in the neutral decay mode from the calorimeter information, a side band method is used to determine the difference $\Delta\alpha_{\mathrm{L}S} = \alpha^{00}_{\mathrm{L}S} - \alpha^{+-}_{\mathrm{L}S}$ between the neutral and the charged decay mode.

The dilution depends only on the proton rate in the Tagger and on the width of the tagging window. Thus the determination of the proton hit probability in a time window $\overline{W}$ of the same width as the tagging window is an estimation of the dilution. This determination is possible for the neutral decay mode as well as for the charged decay mode. Therefore it can be used to determine a dilution difference between both decay modes.

Figure 39 shows the time structure of the SPS proton beam. Because of the 200 MHz structure only shifts of the tagging window in steps of 5 ns are allowed. Otherwise the proton rates would be different for the real tagging window W and for the shifted window $\overline{W}$. The choice of shifted tagging windows $\overline{W}$ is further limited by the Tagger readout: Since the Tagger read-

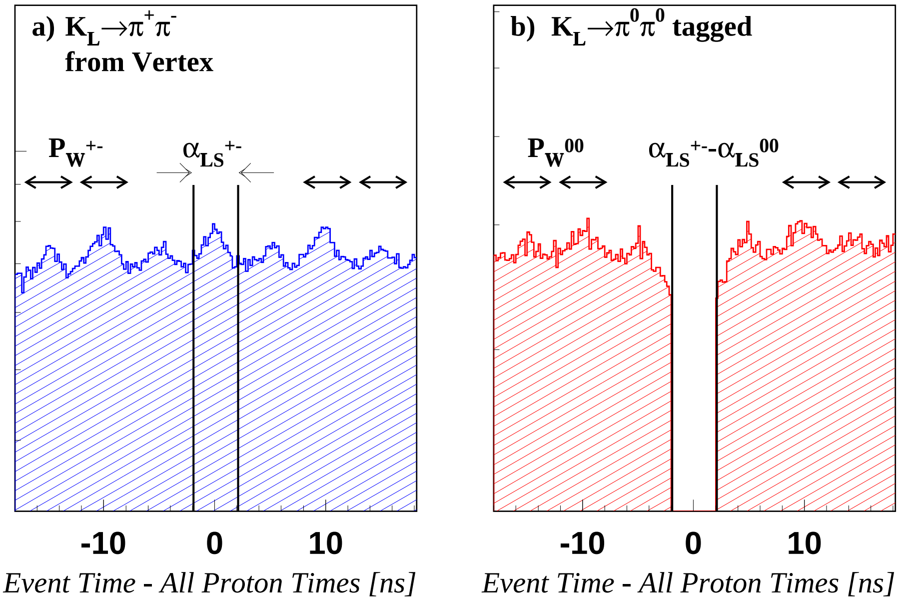

Figure 38: Proton hit times and shifted tagging windows. The number of proton hits with respect to the event time for a selected event is shown. A 200 MHz structure is clearly visible. The tagging window W is shifted in 5 ns steps $(\overline{W})$ to determine the proton hit probabilities $P_{\overline{W}}^{+-}$ and $P_{\overline{W}}^{00}$ in the sidebands.

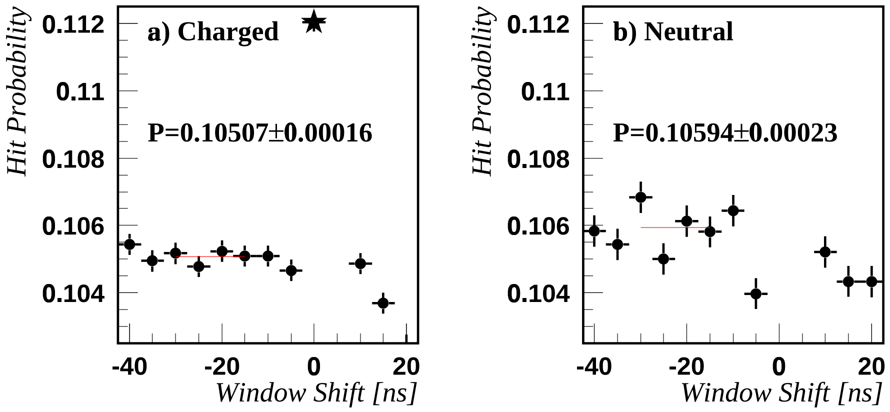

Figure 39: Proton hit probability in shifted tagging windows. The tagging window is shifted in 5 ns steps around the event time. The probability for a proton to hit the window is measured. The dilution in the charged decay mode, measured with the vertex method, is marked with a star.

out window is different for charged and neutral events, only shifts in the interval $[-30\text{ ns}, +5\text{ ns}]$ around the event time are allowed. The interval $[-10\text{ ns}, +5\text{ ns}]$ is affected by after pulses. Thus window shifts of -30, -25, -20, and -15 ns are used.

The probability $P_{\overline{W}}$ for a proton to hit the shifted tagging window is determined in the charged and the neutral decay mode. The difference is then

$$\Delta\alpha_{LS} = 1.035 \cdot (P_{\overline{W}}^{00} - P_{\overline{W}}^{+-}). \tag{8.19}$$

As the neutral decay mode is used, K_L events have to be identified with the Tagger. Thus the event sample does not conain true K_L events which are mis-tagged. There is a correction factor of 1.035 to $\Delta\alpha_{LS}$ due to a difference in the proton hit probability for events that are correctly tagged and for events that are mis-tagged. The change in R is 0.5×10^{-4} due to this correction factor. For a complete derivation of formula (8.19) see Appendix A.1.

Figure 40 shows the proton hit probabilities for various shifted windows and the result of the fit. $P_{\overline{W}}^{+-}$ and $P_{\overline{W}}^{00}$ are determined from a one parameter fit to the four data points. The error is calculated as binomial error for each window shift. The measured dilution from the charged vertex tag is marked with a star in the plot. The measurement of α_{LS} using the vertex tag is done with a sample of events including mis-tagged events. The hit probability in the side bands is measured with a sample of tagged events, *i.e.* events without an accidental hit in the Tagger. The proton hit probability in the side bands is higher for events that are mis-tagged. This explains why vertex tagging gives a higher dilution than the side band method (see also Appendix A.1). The sideband method yields a result of

$$\Delta\alpha_{\mathrm{L}S} = (9.0 \pm 2.8) \times 10^{-4}. \tag{8.20}$$

The resulting correction to R is

$$\Delta R = (+16 \pm 9) \times 10^{-4}. \tag{8.21}$$

The main reason for the dilution difference in the charged and neutral final state is the trigger inefficiency of about 10% in the charged mode. The charged trigger efficiency is intensity dependent. The charged trigger rejects more events under conditions of high beam intensity and thus the charged event sample has on average a lower proton rate in the Tagger. Therefore the dilution is higher in the neutral decay mode.

8.4.4 Tagging Efficiency in the Neutral Decay Mode

In general there are two possibilities to measure the tagging efficiency in the neutral decay mode. The first one is the direct method, using K_{S} events which are identified by a different criteria other than using the Tagger. The second one is to compare the time measurement of the neutral decay mode to the time measurement of the charged decay mode and to deduce the difference in the tagging efficiency. Both principles have been used:

- γ conversions from $K \to \pi^0\pi^0$, $\pi^0\pi^0\pi^0$ decays are used to determine differences in the measurement of the time between the neutral and the charged decay component. A detailed study [Len99] shows that there is no difference between the charged and neutral tagging efficiency within an accuracy of $\pm 1 \times 10^{-4}$. Figure 41 shows the measured time difference using the LKR and the HOD. Tagging inefficiencies are mainly due to the Tagger, which is intrinsically symmetric between K_{S} and K_{L}.

- The tagging efficiency is measured directly with Dalitz decays $K_{\mathrm{S}} \to \pi^0\pi^0{}_D \to \gamma\gamma\gamma e^+e^-$ and with γ conversion from $K_{\mathrm{S}} \to \pi^0\pi^0$ decays. The electron tracks are used to determine the y-vertex position. The vertex tag is then compared to the Tagger result. This method is limited by the small number of events. One mis-tagged event out of 6939 with 0.65 expected K_{L} background events has been found [Vat98]. Using Poisson statistics the resulting inefficiency is $(0.8^{+3.3}_{-0.6}) \times 10^{-4}$, which is

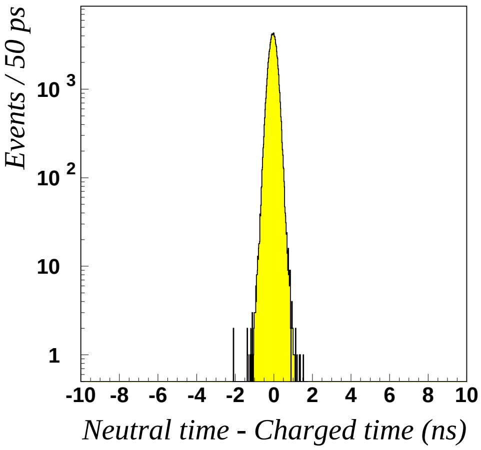

Figure 40: Time difference between the neutral time and the hodoscope time for neutral events with γ conversion. The neutral time is a weighted average of the LKR time and the NHOD time.

consistent with the tagging inefficiency in the charged decay mode of $\alpha_{SL}^{+-} = (1.5 \pm 0.1) \times 10^{-4}$.

- The mis-tagging rate is also determined in pure K_S data taking periods. The disadvantage is that conditions are not identical to the ε'/ε data taking. In particular accidental effects may be different. The tagging efficiency is measured to be $(0.9 \pm 0.7) \times 10^{-4}$ [Vat98] in the K_S runs.

In all methods the difference between the charged and neutral tagging efficiency is consistent with 0. Therefore no correction to R is applied for this effect. Sabine Crépé has shown [Cré98] that an uncertainty $\mathrm{d}\Delta\alpha_{SL}$ in $\Delta\alpha_{SL}$ translates into an uncertainty on R of $\mathrm{d}R = 6.1 \cdot \mathrm{d}\Delta\alpha_{SL}$. Therefore an additional uncertainty of

$$\mathrm{d}R = \pm 6 \times 10^{-4} \tag{8.22}$$

due to the uncertainty in the tagging efficiency of the neutral decay mode is assigned to R.

8.5 Charged Trigger Efficiency

The inefficiency of the charged trigger has contributions from the following sources:

1. The efficiency of the L1 Trigger signal $Q_x/2 \cdot E_{\mathrm{tot}}$. This efficiency has to be determined separately for the Q_x and the E_{tot} trigger.
2. The efficiency of the Massbox (L2C). This efficiency is determined using the $Q_x/2 \cdot E_{\mathrm{tot}}$ signal generated by the Level 2 Trigger Supervisor.

Both efficiencies are discussed in the next two Sections.

8.5.1 L1C Trigger Efficiency

The Level 1 Charged Trigger is built from the coincidence of the Q_x signal, which is down-scaled by a factor of 2, and the E_{tot} signal coming from the neutral trigger. In addition the Q_x signal, which is down-scaled by a factor of $D = 128$ (Q_x/D), is used in the L1C. Thus the L1C trigger signal is $Q_x/2 \cdot E_{\mathrm{tot}} + Q_x/D$. The down-scaling and the coincidence of these signals is done in the Level 1 Trigger Supervisor (see Section 5.1).

In order to determine the efficiency of the Q_x signal, the NHOD trigger is used. The E_{tot} trigger efficiency is determined using the Q_x/D trigger. The NHOD trigger cannot be used for measuring the E_{tot} efficiency, as the event selection might be biased, since the NHOD requires already an energy deposit in the LKR.

To determine the efficiency of the Q_x and the E_{tot} trigger signals, the same event selection is used as in the determination of R. The Pattern Unit information (see Section 4.8) on the Level 1 Trigger signals is used to determine whether the trigger is set. The trigger must occur in the same time slice or in a neighboring time slice as the event. This is done to account for a relative time jitter between the the two trigger signals, *i.e.* the down-scaled trigger and the trigger under investigation. Inefficiencies due to a jitter between the $Q_x/2$ and the E_{tot} signals are accounted for in the Level 2 Trigger efficiency.

In total 6171 NHOD triggers with $\pi^+\pi^-$ events are selected. Of these events 6154 also have the Q_x trigger set. The resulting Q_x efficiency, separated for K_{S} and K_{L} decays, is:

$$\epsilon_{Q_x,\mathrm{S}} = 0.9970 \pm 0.0008, \qquad (8.23)$$

$$\epsilon_{Q_x,\mathrm{L}} = 0.9976 \pm 0.0015. \qquad (8.24)$$

As the efficiencies are, within errors, symmetric for K_{S} and K_{L} decays, no correction to R is applied.

There are 2447 Q_x/D events selected to determine the E_{tot} efficiency. Only 3 events are found which do not have the E_{tot} signal set in the same or a neighboring time slice. However, these 3 events have the E_{tot} signal set 2 time slices before the Q_x/D signal. In addition all 3 events have the signal 'Strobe to Massbox' set, meaning that the coincidence $Q_x/2 \cdot E_{\text{tot}}$ was fulfilled in the Level 2 Trigger Supervisor. Therefore these events are not inefficient E_{tot} triggers, but most likely occur due to an inefficiency of the PMB readout. Using 68.27% and 90% confidence limits [FC98], the E_{tot} efficiencies for K_{S} and K_{L} decays are:

$$\begin{aligned}
\epsilon_{E_{\text{tot}},\text{S}} &> 0.9992\ (68.27\%\text{C.L.}), && (8.25)\\
\epsilon_{E_{\text{tot}},\text{L}} &> 0.9985\ (68.27\%\text{C.L.}), && (8.26)\\
\epsilon_{E_{\text{tot}},\text{S}} &> 0.9985\ (90\%\text{C.L.}), && (8.27)\\
\epsilon_{E_{\text{tot}},\text{L}} &> 0.9971\ (90\%\text{C.L.}). && (8.28)
\end{aligned}$$

As no inefficient event has been found, no correction to R is applied for the E_{tot} inefficiency.

8.5.2 L2C Trigger Efficiency

There are three reasons that can lead to a Massbox inefficiency:

1. The $Q_x/2$ and the E_{tot} coincidence is not made correctly in the L1TS (so-called no-strobe events, see Table 5 on page 42). The reason for this effect is a time jitter between the two signals and the insufficient dynamical E_{tot} widening, which leads to edge effects (see Section 5.1). The resulting inefficiency is up to 7% in certain run periods.

2. The drift chamber is inefficient. This affects the Massbox more than the reconstruction, as the algorithm has been tuned to be fast.

3. The Massbox algorithm is inefficient or too slow, *e.g.* when too many hits increase the number of possible combinations and the Massbox cannot give a trigger decision in time.

All inefficiencies can be determined using the down-scaled $Q_x/2 \cdot E_{\text{tot}}$ signal, generated by the Level 2 Trigger Supervisor. Since the coincidence algorithm of the L2TS is fully efficient, the L1TS coincidence efficiency can be determined.

The running conditions have been changed several times during the data taking period (see Table 13). These modifications changed the efficiency of the Massbox. Only after the E_{tot} realignment in period 6, the optimal efficiency of 0.961 ± 0.002 was reached. Figure 42 gives an overview of the Massbox efficiency over the data taking period. While the alignment of the internal time offsets allowed for a more exact computation of drift times

Period	Run Number	Changes
1	4705 - 4865	
2	4866 - 4952	Alignment of time offsets
3	4953 - 5145	Increase of the time budget, lower $c\tau$ cut, Q_x realignment
4	5146 - 5276	Reversal of the magnetic field
5	5277 - 5312	Switching (off/on) of the magnet, higher z-vertex cut
6	5313 - 5366	E_{tot} realignment

Table 13: The six different run periods due to changes in the charged trigger or in the magnetic field. For a change in the selection criteria see also Table 6.

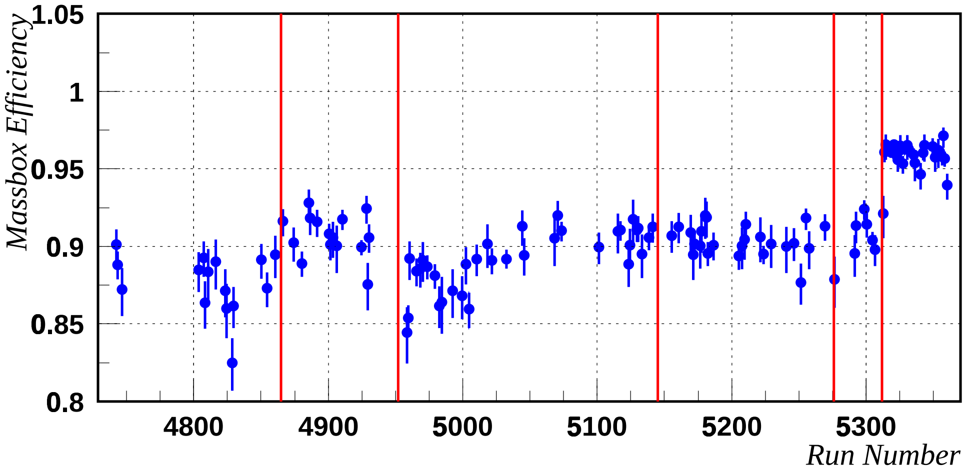

Figure 41: Global Massbox efficiency as function of the run number. Short runs have been excluded from this plot.

and increased the efficiency, the Q_x realignment caused losses of triggers due to missed coincidences with the E_{tot} signal. This changed only after the E_{tot} realignment after run 5313. The changes in the magnetic field did not affect the Massbox efficiency. As an upper limit of 3.5 τ_{K_S} is used in the final analysis, the change in the Massbox lifetime requirement from 4.5 τ_{K_S} to 4.0 τ_{K_S} has not affected the Massbox efficiency. Also the change of the requirement of the z-decay vertex position has not affected the Massbox efficiency.

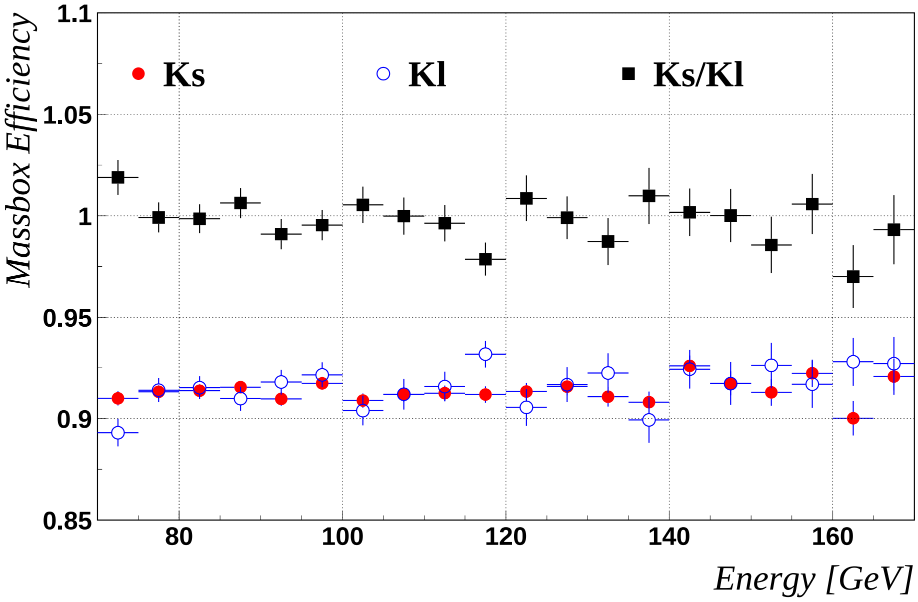

Figure 42: Massbox efficiency for K_S and K_L events for each energy bin.

The overall Massbox efficiencies are:

$$\epsilon_{\mathrm{MBX,S}} = 0.9131 \pm 0.0009, \tag{8.29}$$

$$\epsilon_{\mathrm{MBX,L}} = 0.9138 \pm 0.0018. \tag{8.30}$$

The Massbox efficiency as function of energy is shown in Figure 43. The resulting correction to R is:

$$\Delta R = (+11 \pm 22) \times 10^{-4}. \tag{8.31}$$

8.6 Neutral Trigger Efficiency

The efficiency of the neutral trigger is determined using the independent trigger from the Neutral Hodoscope. This trigger requires a hit in both halves of the NHOD: either in the upper and lower halves, or in the left and right halves. In total 6841 K_S and 2948 K_L events with a NHOD trigger are selected. As the neutral trigger efficiency is lifetime dependent [Fis98], the trigger efficiency is calculated with weighted K_L events. The number of weighted K_L events obtained in this way is 832.27.

10 inefficient K_S events and 2 inefficient K_L events (0.23 events after

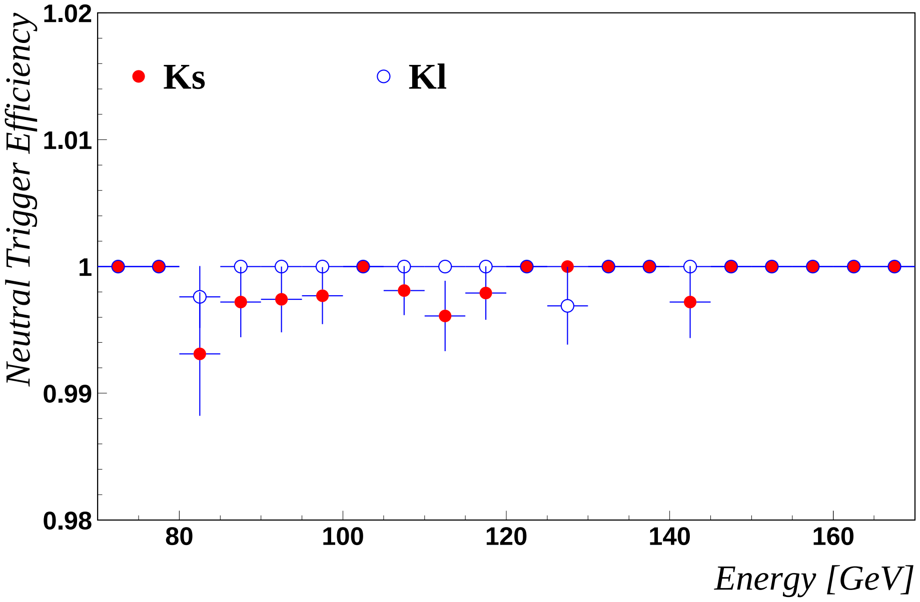

Figure 43: Efficiency of the neutral trigger for K_{S} events and weighted K_{L} events per energy bin.

weighting) are found. The resulting inefficiencies are:

$$\begin{aligned}\epsilon_{\mathrm{NUT,S}} &= 0.9985 \pm 0.0004,\\ \epsilon_{\mathrm{NUT,L}} &= 0.9993 \pm 0.0005.\end{aligned}$$

Figure 44 shows the trigger efficiency with weighted K_{L} events per energy bin. The inefficient events have been checked on an event by event basis. The reasons for inefficiencies are [Fis98]:

1. One strip of the y-view of the LKR (see Section 5.1.1) has a bit error. The energy of a photon hitting this strip is therefore underestimated.
2. A few LKR cells are mis-calibrated and the mis-reconstructed energy causes the loss of events.
3. Lambdas produced at the K_{L} target decay into protons, which may pass the cleaning magnets. If the Λ decay is accidentally in time with a $K \rightarrow \pi^0\pi^0$ event, the proton can deposit so much energy in the LKR calorimeter that the good event is rejected by the COG selection.
4. Accidental $K_{\mathrm{L}} \rightarrow 3\pi^0$ decays close in time to the good event cause a rejection, as the number of peaks exceeds the allowed limit.

For several reasons no correction due to the neutral trigger inefficiency has been applied:

- The K_S and K_L inefficiencies are compatible with each other within errors. This fact is confirmed by a first look at the neutral trigger efficiency of the data taken in 1998.
- Problems in calibration and electronics are intrinsically symmetric for K_S and K_L events. Acceptance studies show that the effect of remaining geometrical differences are small.
- Studies of accidental effects have shown that they are almost symmetric for K_S and K_L.

For these reasons, and given the small statistics in the K_L data sample, no correction has been applied.

8.7 Charged Background

Three possible sources of background are identified:

1. K_{e3} events. An electron can be misidentified as a pion if the energy or the momentum is not measured correctly. In this case the electron may pass the E/p selection. If the neutrino has a low transverse momentum, the event may also pass the ${p_\mathrm{t}'}^2$ selection.
2. $K_{\mu3}$ decays may also be misidentified as $\pi^+\pi^-$ events due to inefficiencies of the Muon Veto detector.
3. Radiative decays $K_\mathrm{S,L} \to \pi^+\pi^-\gamma$ can be misidentified. Analytic calculations and Monte Carlo simulations have shown that this effect is negligible for the 1997 data taking.

The background is determined by extrapolating the event numbers found in two control regions into the signal region. The signal region is defined by the selection criteria given in Section 7.4. The definitions of the control regions are given in Table 14. Figure 45 shows the position of the control regions in the $m_{\pi\pi} - {p_\mathrm{t}'}^2$-plane.

Pure samples of K_{e3} and $K_{\mu3}$ decays are used to determine the extrapolation factors. The distribution of K_{e3} and $K_{\mu3}$ decays in the $m_{\pi\pi} - {p_\mathrm{t}'}^2$-plane is shown in Figures 46c and 46d. The control regions are selected such that control region 1 is dominated by K_{e3} decays, and control region 2 is dominated by $K_{\mu3}$ decays. K_{e3} events are selected by requiring $E/p > 0.95$ for

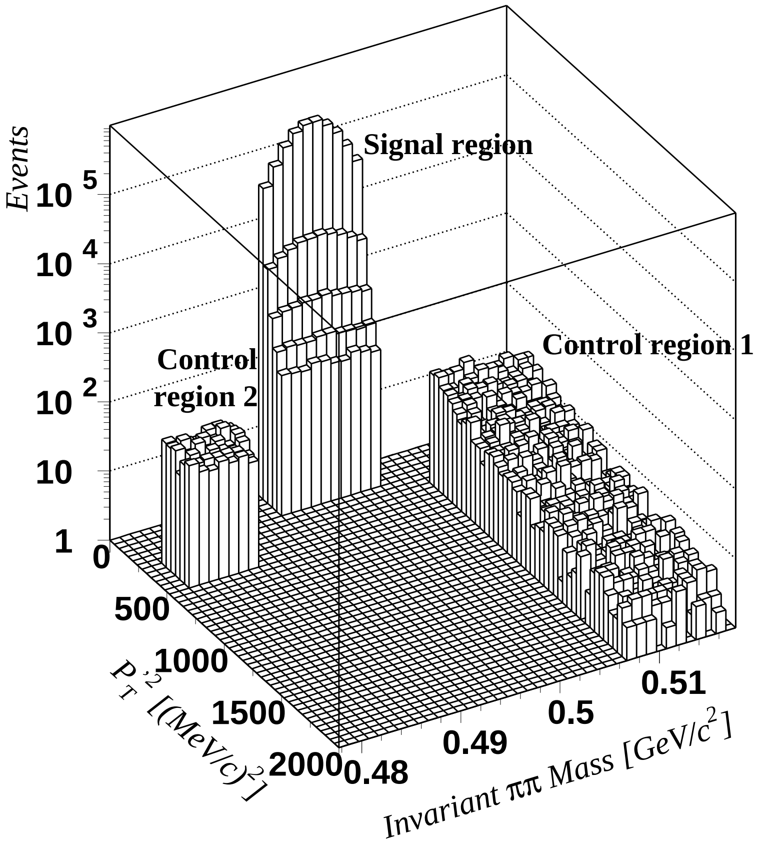

Figure 44: Location of the control regions in the $m_{\pi\pi} - {p_{\mathrm{t}}'}^2$-plane. Shown are $K_{\mathrm{L}} \rightarrow \pi^+\pi^-$ events in the control regions and in a region close to the signal region. The real signal region cannot be defined in terms of a fixed mass range, as the mass selection is based on the resolution and is energy dependent.

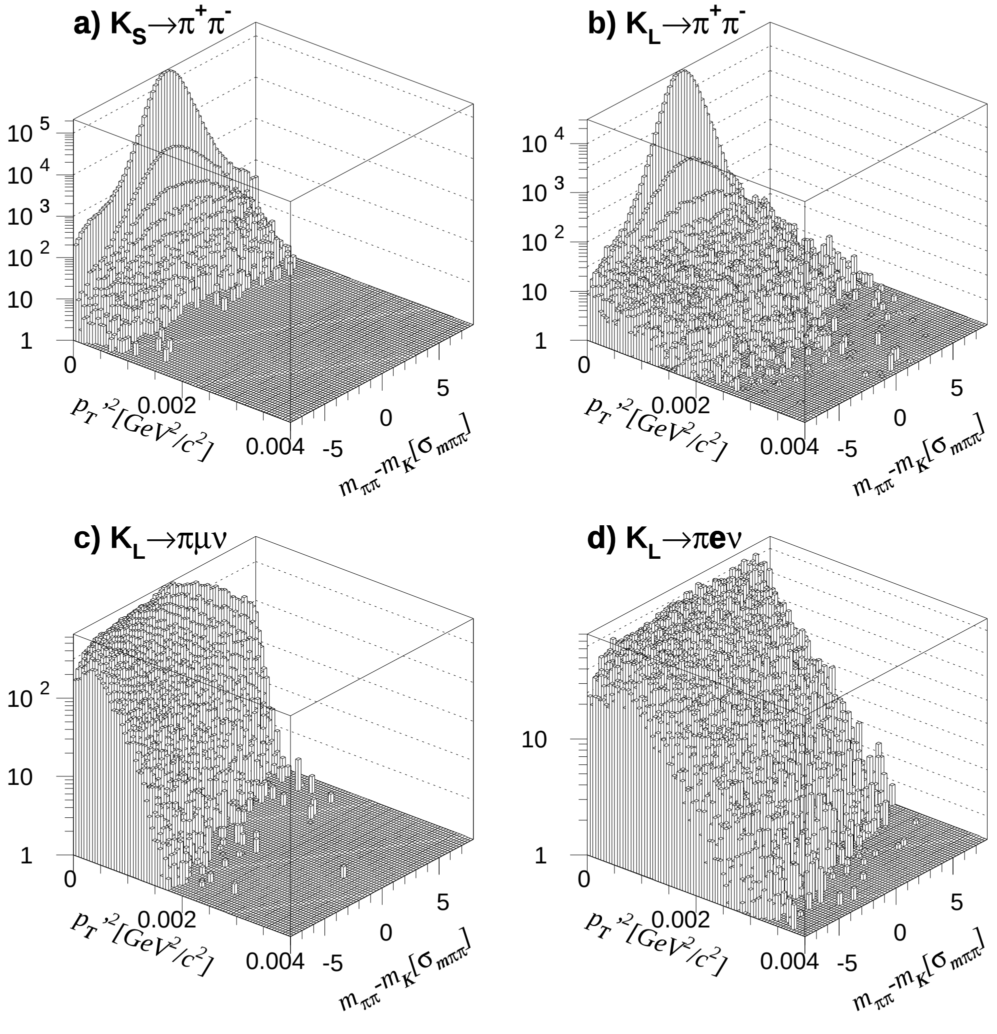

Figure 45: Distributions of ${p_t}'^2$ versus mass for various decay modes. K_S and K_L decays are identified with the vertex tag. A MUV hit, in time with the event time, is required for a $K_{\mu3}$ event. K_{e3} events are selected by requiring $E/p > 0.95$.

	Mass [MeV]	${p_\mathrm{t}'}^2[(\mathrm{MeV}/c^2)^2]$
Control region 1	$507.2 < m_{\pi\pi} < 516.7$	$300 < {p_\mathrm{t}'}^2 < 2000$
Control region 2	$480.7 < m_{\pi\pi} < 486.7$	$300 < {p_\mathrm{t}'}^2 < 500$

Table 14: Definitions of the control regions. Their position is shown in Figure 45.

one track. $K_{\mu3}$ events must have a hit in the Muon Veto around one of the extrapolated tracks within ±4 ns of the event time. The selected events M are used to determine extrapolation factors $\alpha_i^{K_{e3}(K_{\mu3})}$ for control region i:

$$\alpha_i^{K_{e3}} = \frac{M_S^{K_{e3}}}{M_i^{K_{e3}}}, \tag{8.32}$$

$$\alpha_i^{K_{\mu3}} = \frac{M_S^{K_{\mu3}}}{M_i^{K_{\mu3}}}. \tag{8.33}$$

$M_{i,S}^{K_{e3}(K_{\mu3})}$ denote the number of events found in the control region i, or the signal region S, for selected K_{e3} ($K_{\mu3}$) events.

The number of selected K_L events $N_i^{K_\mathrm{L}}$ in control region i (Figure 46b) consists of the sum of K_{e3} and $K_{\mu3}$ events in that control region:

$$N_i^{K_\mathrm{L}} = N_i^{K_{e3}} + N_i^{K_{\mu3}}. \tag{8.34}$$

The extrapolation factors (8.32) and (8.33) are also valid for the unknown number of K_{e3} and $K_{\mu3}$ events in the signal region and the control region of the K_L decays:

$$N_i^{K_{e3}} = \frac{N_S^{K_{e3}}}{\alpha_i^{K_{e3}}}, \tag{8.35}$$

$$N_i^{K_{\mu3}} = \frac{N_S^{K_{\mu3}}}{\alpha_i^{K_{\mu3}}}. \tag{8.36}$$

Using these relations together with equations (8.34), one obtains for the number of K_{e3} and $K_{\mu3}$ decays in the signal region:

$$N_S^{K_{e3}} = \frac{\alpha_1^{K_{e3}}\alpha_2^{K_{e3}}(\alpha_1^{K_{\mu3}}N_1^{K_\mathrm{L}} - \alpha_2^{K_{\mu3}}N_2^{K_\mathrm{L}})}{\alpha_1^{K_{\mu3}}\alpha_2^{K_{e3}} - \alpha_2^{K_{\mu3}}\alpha_2^{K_{e3}}}, \tag{8.37}$$

$$N_S^{K_{\mu3}} = \frac{\alpha_1^{K_{\mu3}}\alpha_2^{K_{\mu3}}(\alpha_1^{K_{e3}}N_1^{K_\mathrm{L}} - \alpha_2^{K_{e3}}N_2^{K_\mathrm{L}})}{\alpha_1^{K_{e3}}\alpha_2^{K_{\mu3}} - \alpha_2^{K_{e3}}\alpha_2^{K_{\mu3}}}. \tag{8.38}$$

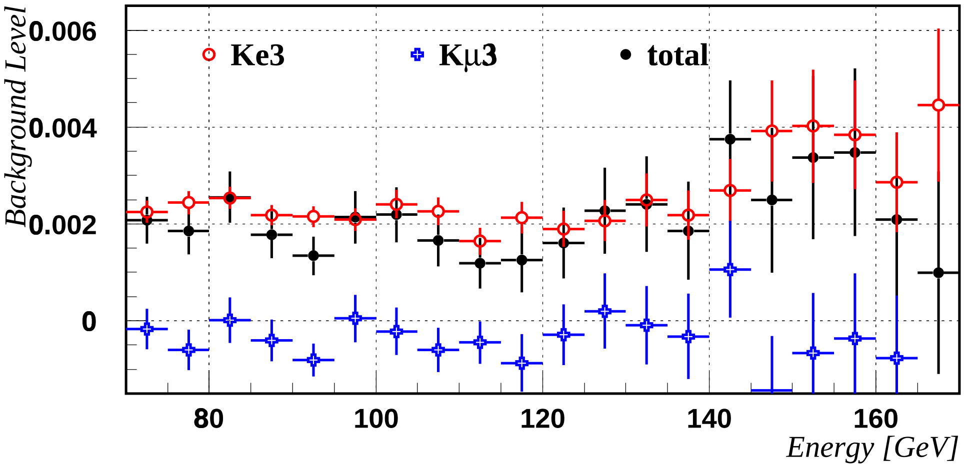

Figure 46: Relative background level for K_{e3} and $K_{\mu3}$ decays per energy bin.

For this calculation the number of K_S events (Figure 46a) in the control regions is subtracted from the number of K_L events in the control regions.

Figure 47 shows the background fraction for K_{e3} and $K_{\mu3}$ decays in the signal region. There is no background coming from $K_{\mu3}$ decays. The background is dominated by K_{e3} decays. The global background fraction in the signal region is $(+20 \pm 3) \times 10^{-4}$.

The systematic uncertainties in the background determination have been studied using different control regions. As an alternative, a different method than the one described above has also been used. In this method the background shape is fitted in the control region. The fit result is then extrapolated into the signal region. Comparing the various results, an additional uncertainty of $\pm 4 \times 10^{-4}$ is found.

The resulting correction to R is:

$$\Delta R = (+20 \pm 5) \times 10^{-4}.$$

8.8 Scattering at the Collimator

Some genuine $K \to \pi^+\pi^-$ decays have been found in the K_L sample with values of ${p_\mathrm{t}'}^2$ beyond the signal region (see Figure 48). To be consistent with the observed high ${p_\mathrm{t}'}^2$ momentum, the kaon must have scattered at one of the collimators.

The events under the peak of Figure 48 are compared to those of the mass sidebands. The radius of the decay vertex position at the z-position of

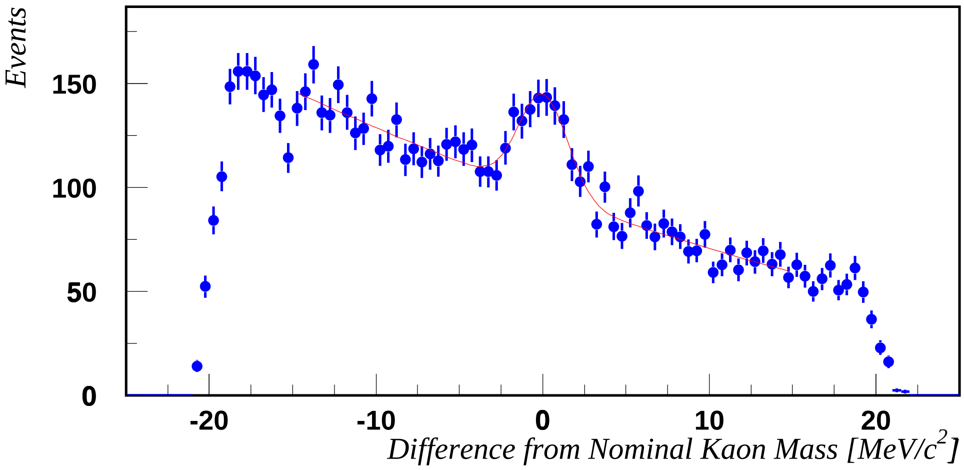

Figure 47: Mass distribution of events in the K_L sample with ${p_\mathrm{t}'}^2 > 200\ (\mathrm{MeV/c})^2$ with respect to the nominal kaon mass.

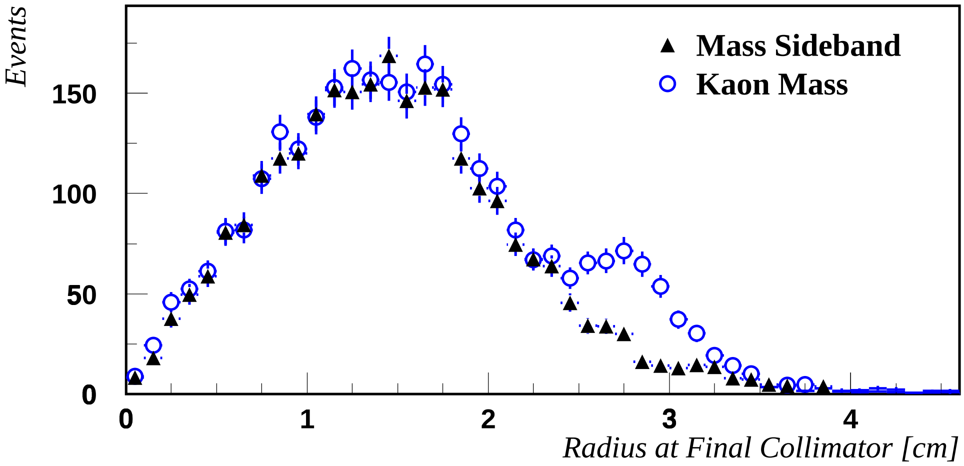

Figure 48: Radius of the events at the z-position of the final collimator. The open circles represent events under the mass peak of Figure 48, and the triangles represent events from side bands.

the collimators of events under the mass peak is consistent with the radius of the final collimator (Figure 49) and the cleaning collimator. A fit to the $\pi^+\pi^-$ mass distribution yields 350 events in the mass peak.

These events pass the COG selection, but are rejected by the requirement on ${p_{\mathrm{t}}'}^2$ in the charged mode. As they are not identified and rejected in the neutral mode, a correction of

$$\Delta R = (-12 \pm 3) \times 10^{-4} \tag{8.39}$$

is applied to R.

8.9 Neutral Background

A $K_{\mathrm{L}} \rightarrow \pi^0\pi^0\pi^0$ decay can be misidentified as a $K_{\mathrm{L}} \rightarrow \pi^0\pi^0$ decay if one or two photons miss the detector. To determine the background under the K_{L} signal, event numbers with high R_{ellipse} are extrapolated into the signal region. Figure 50a shows the R_{ellipse} distribution for K_{S}, K_{L}, and weighted K_{L} decays (see also Figure 30 in Section 7.5).

The background determination consists of three steps:

1. A correction for the dilution effect is applied to the K_{S} sample in bins of energy and R_{ellipse}.
2. The normalized K_{S} signal distribution is subtracted from the weighted K_{L} distribution. The main reason for K_{S} events with high R_{ellipse} numbers is γ conversion in the material in front of the calorimeter. The tails in the distribution are reproduced by the Monte Carlo simulation.
3. The flat background (see Figure 50b) is averaged in a region of $36 < R_{\mathrm{ellipse}} < 126$ and extrapolated into the signal region. From Monte Carlo simulation of $K_{\mathrm{L}} \rightarrow 3\pi^0$ decays an extrapolation factor of 1.2 ± 0.2 is determined. This factor accounts for the fact that the background is not flat under the signal peak. The uncertainty is governed by Monte Carlo statistics.

Figure 51 shows the background level determined for each energy bin. The resulting correction to R is

$$\Delta R = (-8 \pm 2) \times 10^{-4}. \tag{8.40}$$

8.10 Effect of Accidental Activity

Photons and other neutral particles produced at the target are part of the beams, as they cannot be removed. If one of these background particles, a so-called accidental, crosses the detector at the same time as the decay products of a kaon, the good event may be rejected, although it would have

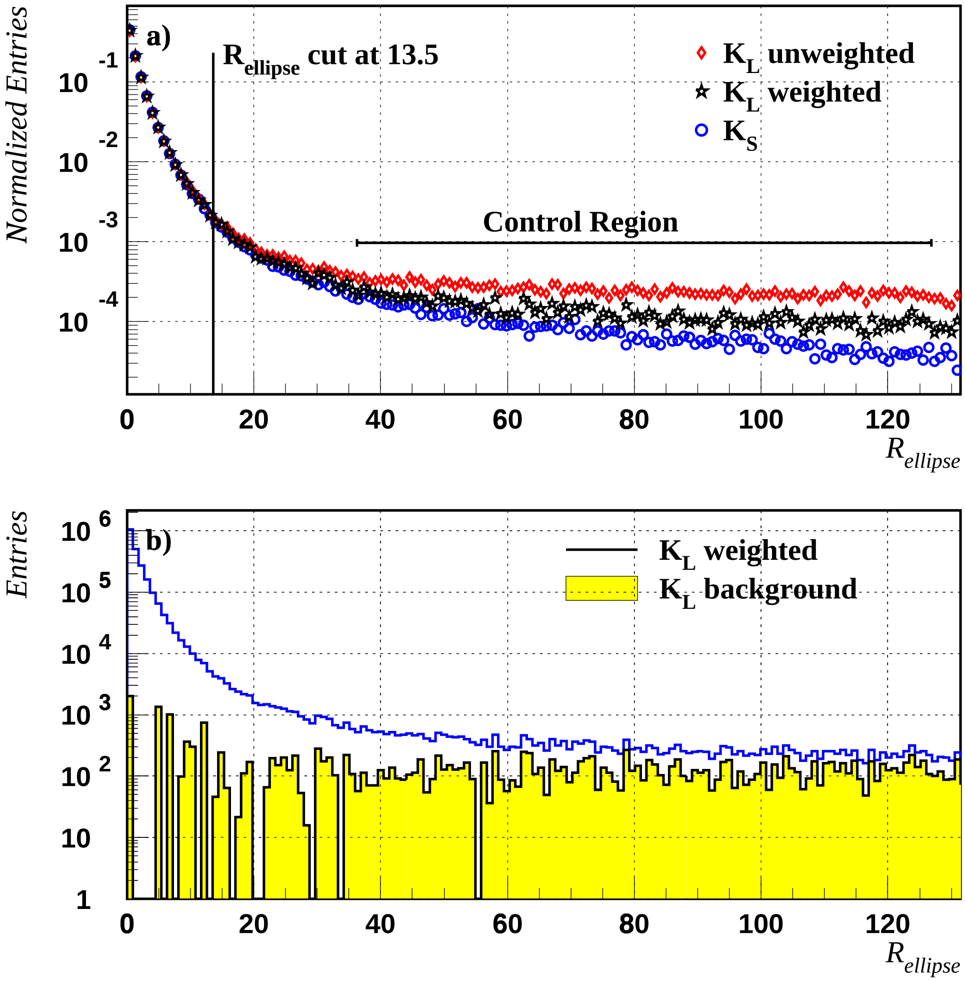

Figure 49: a) R_{ellipse} distribution for K_S, K_L, and weighted K_L decays. The selection cut is at $R_{\text{ellipse}} = 13.5$. The K_S distribution is corrected for dilution. The source of K_S events with high R_{ellipse} number are converted photons. b) Number of weighted K_L events and of background events. The determination of the background is described in the text.

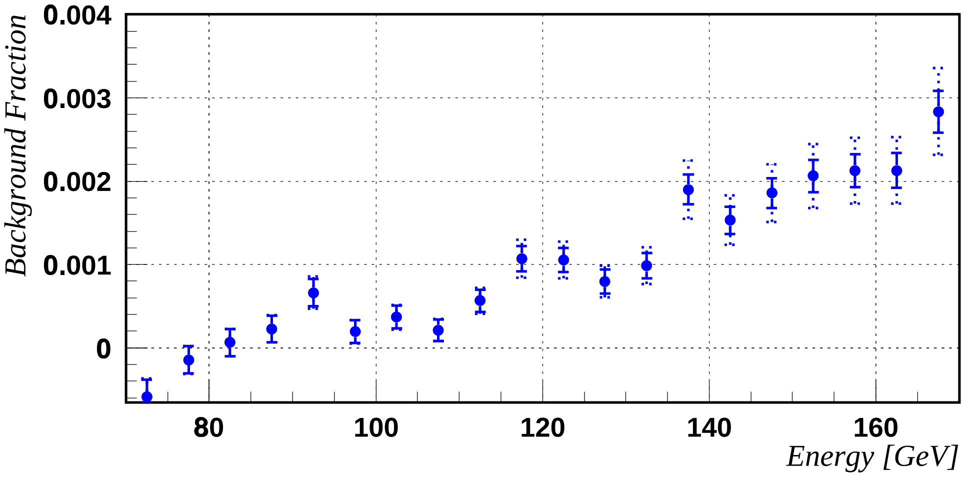

Figure 50: Neutral background level per energy bin. The uncertainty of the Monte Carlo extrapolation factor is added as dotted error bars to the plot.

been accepted without the effect of the extra particle. Statistical fluctuations within the electronics may also alter the measurement.

In principle the effect of accidental activity is very small, as the four decay modes are taken simultaneously and the geometrical illumination of the detector is almost identical. Residual effects are measured using events which are overlaid with random events.

Random events are recorded proportional to the instantaneous K_S and K_L beam intensity. These intensities are determined with the K_S Monitor and the Beam Intensity Monitor. In general a random event does not contain a good event, but just detector noise and background activity from accidentals. The effect of accidentals in time with an event can be determined by overlaying a normal event with a random event containing background activity. In this way the accidental activity is doubled for overlaid events. As all LKR cells are read out for random events, the noise in the resulting overlaid event is doubled.

The overlaying of events has been done during the re-processing of the data within the L3/RTR program. 35% of pre-selected neutral events and 20% of pre-selected charged events are overlaid with random events.

Overlaid events have to fulfill the same selection criteria as normal events. Random events with overflow in the drift chambers are excluded. The accidental activity can have the following effects:

1. **Losses.** An event may not pass the selection criteria due to the ac-

cidental activity. This is the case for up to 3% of the events. For the charged final state, accidental muons, which are reconstructed in time with the event, cause most of the losses. Also the value of E/p may be shifted leading to event losses. For the neutral final state the main effect is the R_{ellipse} selection. The noise level in the LKR is artificially doubled, degrading the mass resolution needed to calculate R_{ellipse}. This effect is a priori symmetric for K_{S} and K_{L} decays.

2. **Gains.** To a lesser extent (0.1%-0.9%) events are added to the sample of selected events by adding accidental activity.

3. **Weight shifts.** The kaon energy may be mis-reconstructed due to accidental activity. For K_{L} events this changes the reconstructed lifetime and therefore the weighting factor of the event (see equation (7.8)). This effect is taken into account.

4. $K_{\mathrm{S}} \leftrightarrow K_{\mathrm{L}}$ **transitions.** K_{S} to K_{L} transitions and vice versa can occur when the event time is reconstructed differently due to accidentals, but the event is not lost. This is only the case for few events. Since tagging effects are measured and corrected separately, this effect is not taken into account here.

Table 15 gives an overview of the gains and losses in each decay mode. It shows that indeed the effect of accidentals cancels in the double ratio. The final correction to R is:

$$\Delta R = (-3 \pm 16) \times 10^{-4}, \tag{8.41}$$

where the uncertainty is due to the limited statistics.

	events	gains	losses	net migration
$K_{\mathrm{S}} \to \pi^+\pi^-$	329540	344	7234	-2.09%
$K_{\mathrm{S}} \to \pi^0\pi^0$	265280	2258	8730	-2.44%
$K_{\mathrm{L}} \to \pi^+\pi^-$	139222	204	3084	-2.06%
$K_{\mathrm{L}} \to \pi^0\pi^0$	110061	2456	5250	-2.39%

Table 15: Effect of accidentals estimated with overlaid events. The first column gives the total number of overlaid events. The second column the number of gained events and the third column the number of lost events due to accidentals. The fourth column contains the net migration of events in the four decay modes.

8.11 Acceptance Correction

The purpose of the acceptance correction is to correct for residual geometrical differences between the detection of K_S and K_L decays. In principle these differences have to be small, as both beams are almost collinear and as the fiducial volume is identical. For the acceptance correction, $K_\mathrm{S,L} \rightarrow \pi\pi$ events are generated in a Monte Carlo simulation and subjected to almost the same selection criteria as data events. The input value for the double ratio R is 1. The difference from 1 in the double ratio after the event selection is then applied as correction to the data.

For this purpose the NMC Monte Carlo program [Sch96] is used. Kaons are generated with the following production spectrum [A$^+$80, Hay96], which is adapted to measurements performed 1995 with the NA48 detector:

$$\begin{aligned}\frac{\mathrm{d}^2N}{\mathrm{d}p\mathrm{d}\Omega} &= \frac{\eta p^2}{4p_0}\left[1.30\cdot\mathrm{e}^{-(8.5p/p_0+3.0p^2\Theta^2)} + 4.35\cdot\mathrm{e}^{-(13p/p_0+3.5p^2\Theta^2)}\right] \\ &\quad \times\left[\mathrm{e}^{(-4.2+0.053p)} + 0.016\right]. \qquad (8.42)\end{aligned}$$

Here p_0 denotes the proton momentum of 450 GeV/c, p the kaon momentum and Θ the production angle.

Kaon decays are generated including interference effects between K_S and K_L. Decay particles are then tracked through the detector. The responses of the sub-detectors are modeled using either the data directly, or using a full GEANT Monte Carlo simulation. Track positions in the drift chambers are simulated using a Gaussian smearing of the true positions with a chamber resolution of 103 μm.

For the LKR calorimeter shower libraries based on a GEANT simulation are used. The outer and inner vessel and the internal structure with zig-zag ribbons and spacer plates are simulated. The detector response has been simulated for photons and electrons in an energy range of 2 GeV to 100 GeV.

Trigger and tagging effects are not simulated as they are treated more accurately using data directly. The same is true for the effect of accidentals.

The generated Monte Carlo events are reconstructed using the standard reconstruction. Pre-selected events are written to tape in Super-COmPACT data format. Events are selected using the same selection criteria as in the data with two exceptions:

1. The E/p selection is omitted. The E/p distribution is intrinsically identical for $K_\mathrm{S} \rightarrow \pi^+\pi^-$ and $K_\mathrm{L} \rightarrow \pi^+\pi^-$ decays for a given energy. On the other hand, the simulation of hadronic showers is difficult so that a Monte Carlo correction may result in a bias.

2. The Monte Carlo does not include the simulation of event times. Selections involving time constraints on the event are not used. This means, for example, that the AKS is simulated by the requirement that the decay must occur downstream of the true AKS position. The AKS efficiency is measured separately.

The resulting Monte Carlo sample is five times larger than the data sample.

As the analysis is done in bins of energy, differences in the energy spectrum do not matter as long as the variation within a 5 GeV bin is small. For completeness these distributions are shown. The energy distributions agree within 10% with the data (see Figure 52 and 53). This is sufficient for an analysis in energy bins of 5 GeV.

On the following pages (Figure 52 to Figure 58) data and Monte Carlo distributions are compared. As the Monte Carlo is used to correct small geometrical differences, mainly distributions sesitive to those are compared. Since the differences in the energy spectra between data and Monte Carlo can lead to different geometrical distributions, the comparison is performed for three energy bins.

The acceptance determined from the Monte Carlo is shown in Figure 59 for each of the four decay modes.

The resulting double ratio R of Monte Carlo events for each energy bin is shown in Figure 60. This leads to an overall correction to R of

$$\Delta R = (+28 \pm 11) \times 10^{-4}, \tag{8.43}$$

where the uncertainty is due to the limited Monte Carlo statistics. An additional systematic uncertainty of 6×10^{-4} is added in quadrature. This uncertainty is found using the following methods [Gra99]:

1. This acceptance correction is compared with one calculated using correlated Monte Carlo events, where K_{S} and K_{L} events are generated in pairs with identical energy, z-decay vertex position, and decay kinematics.

2. Changing the beam geometry.

3. Changing the vertex distribution.

4. Weighting of beam halo events.

5. Variation of the mass selection.

6. Variation of the radial cut at DCH 1 and the LKR.

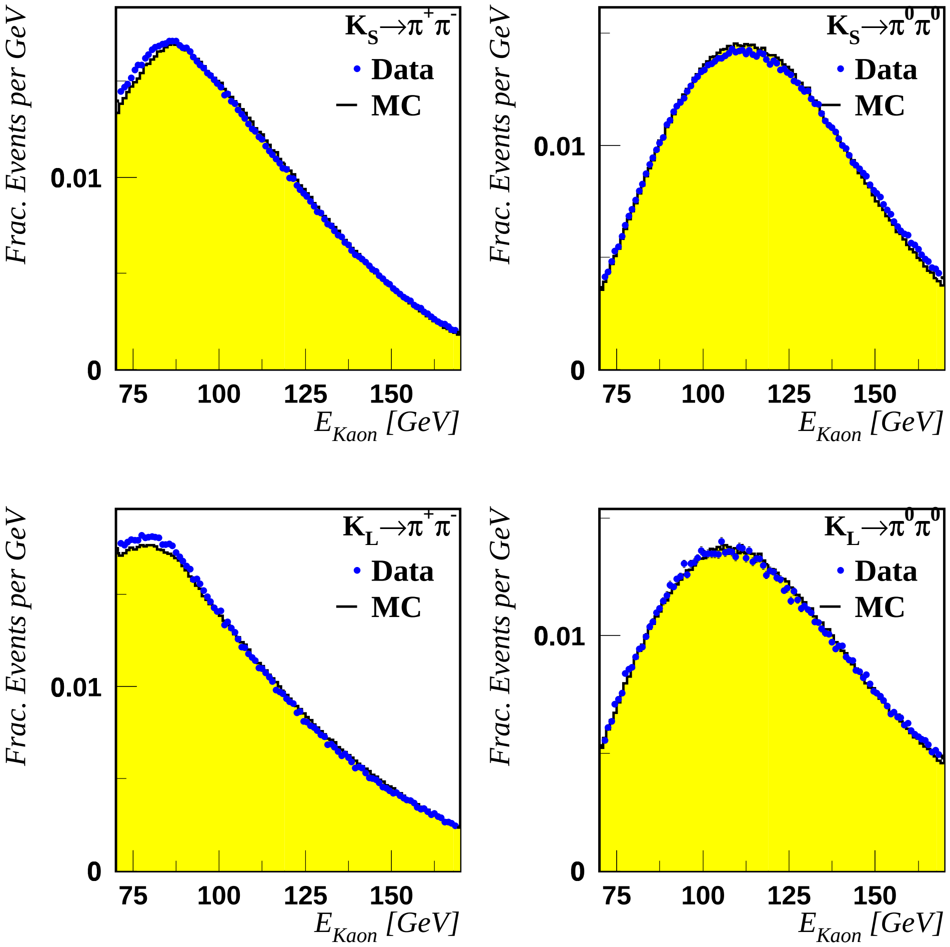

Figure 51: Comparison of the normalized energy distribution of data and Monte Carlo.

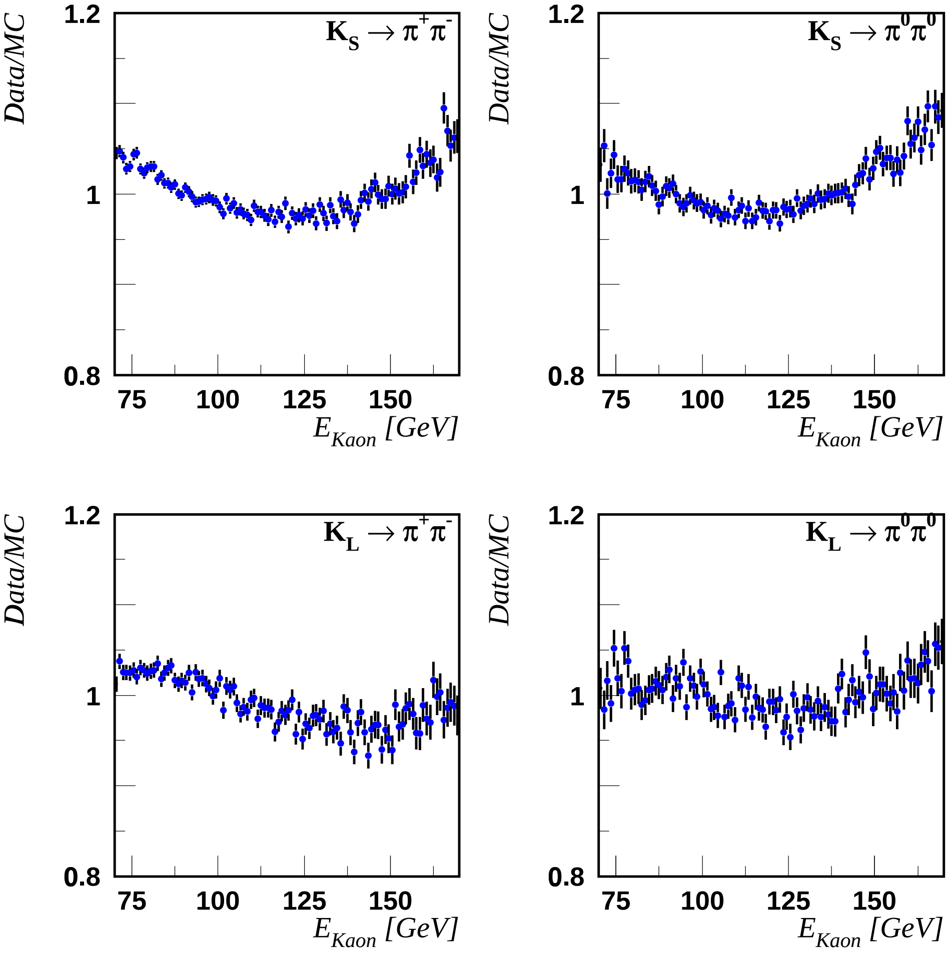

Figure 52: Ratio data/MC for the energy distributions of Figure 52.

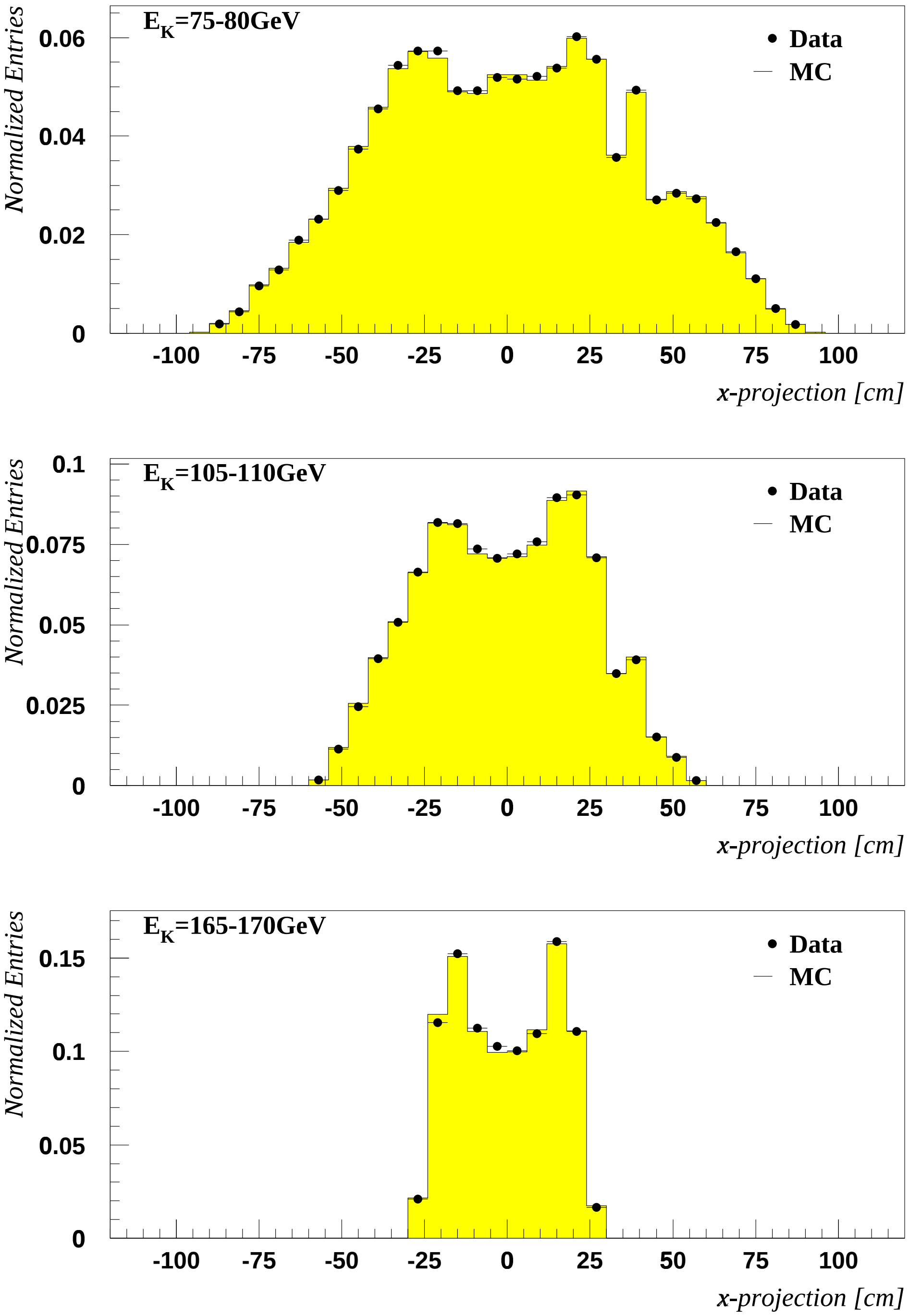

Figure 53: Comparison of the x-projection of track hits at DCH1 for K_S decays.

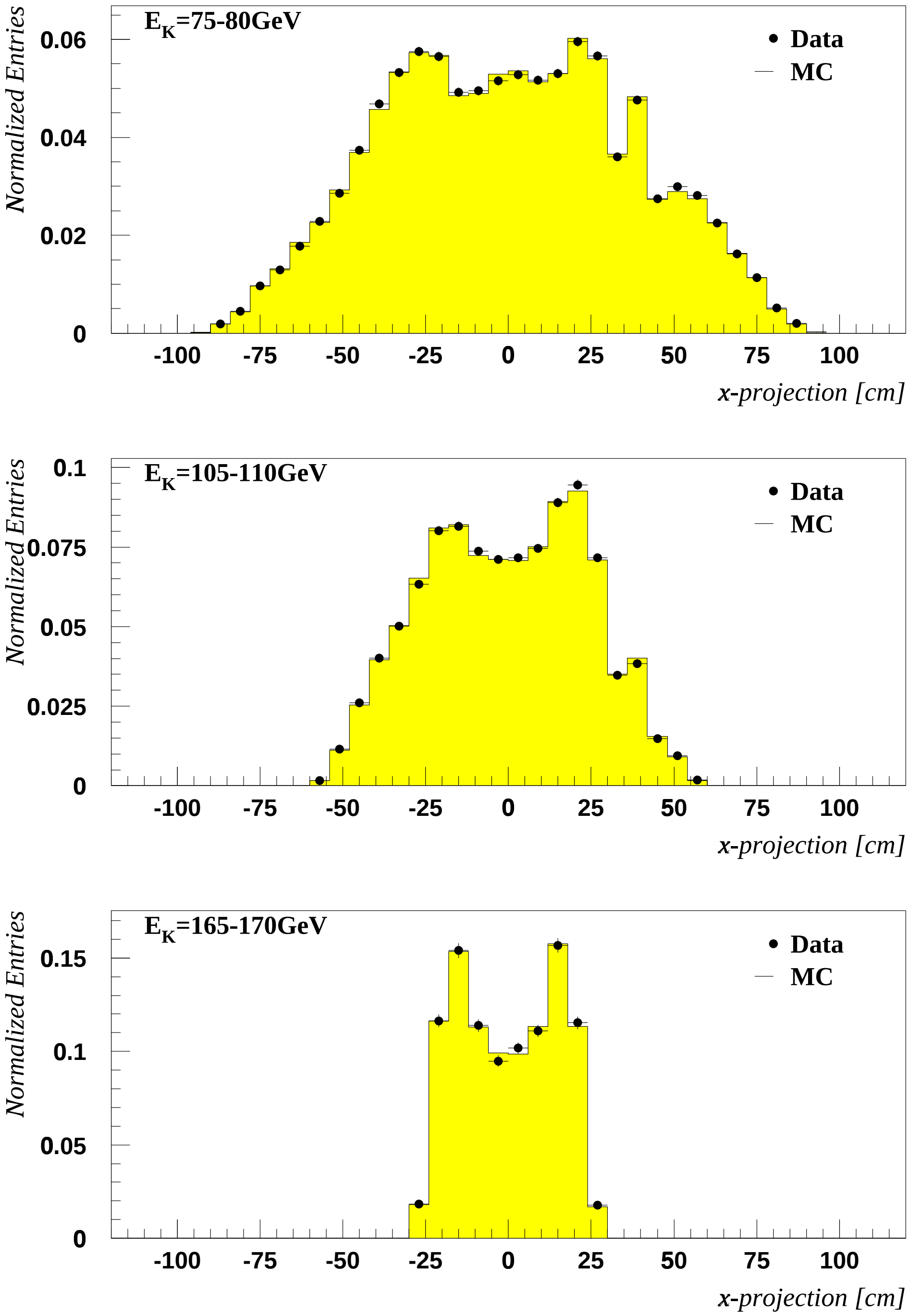

Figure 54: Comparison of the x-projection of track hits at DCH1 for K_L decays.

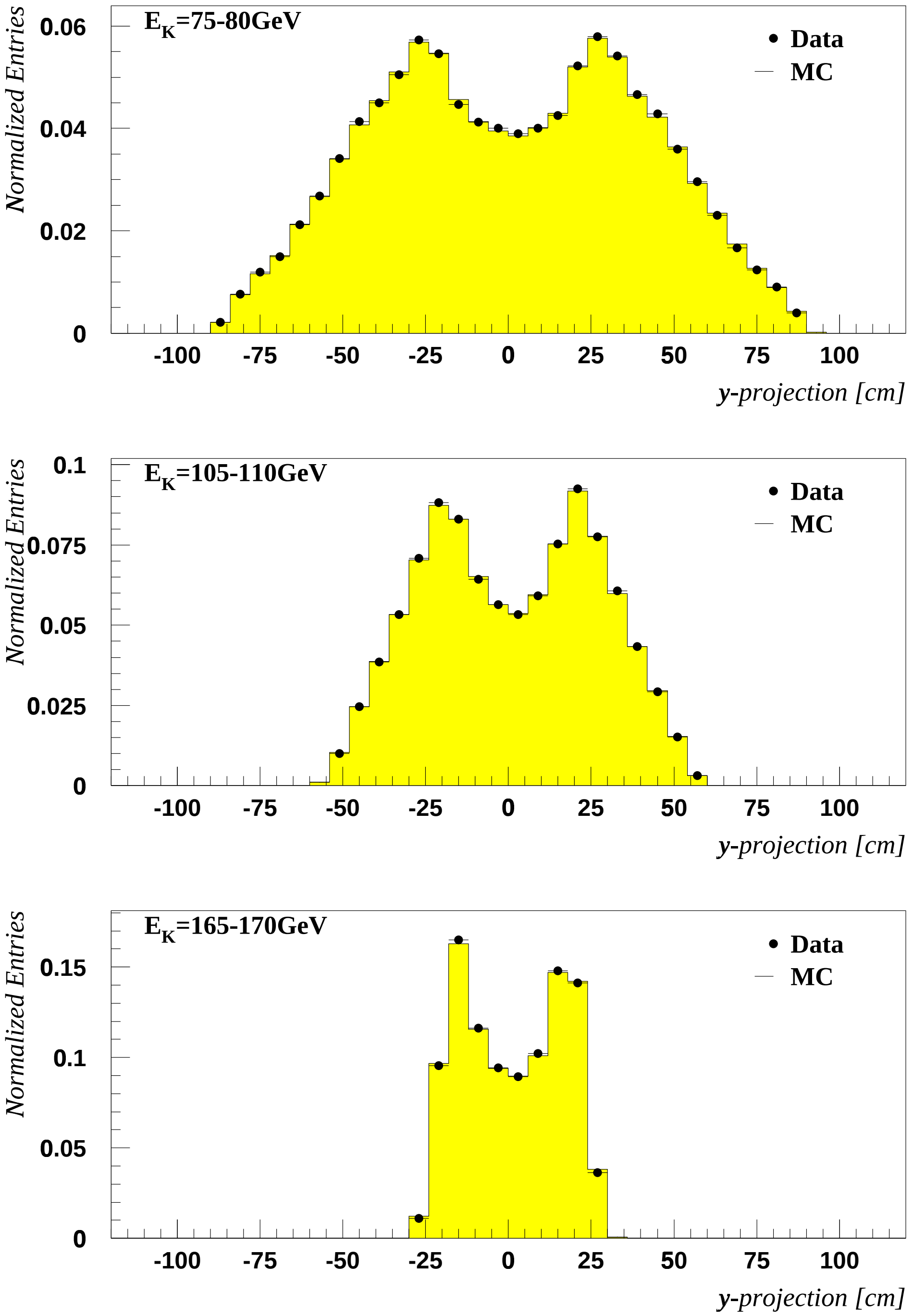

Figure 55: Comparison of the y-projection of track hits at DCH1 for K_S decays.

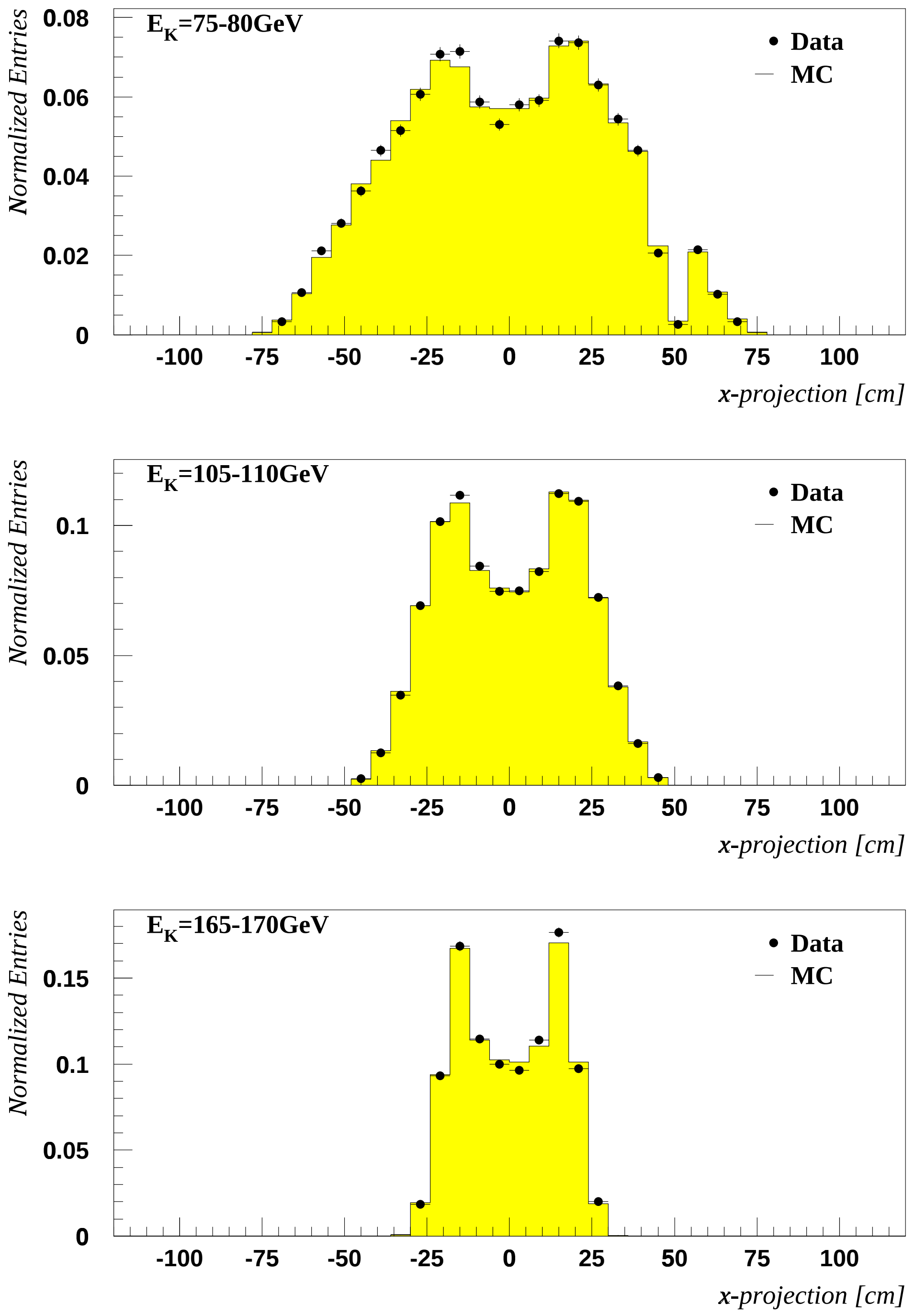

Figure 56: Comparison of the x-projection of the γ cluster which is closest to the beam pipe for K_S decays.

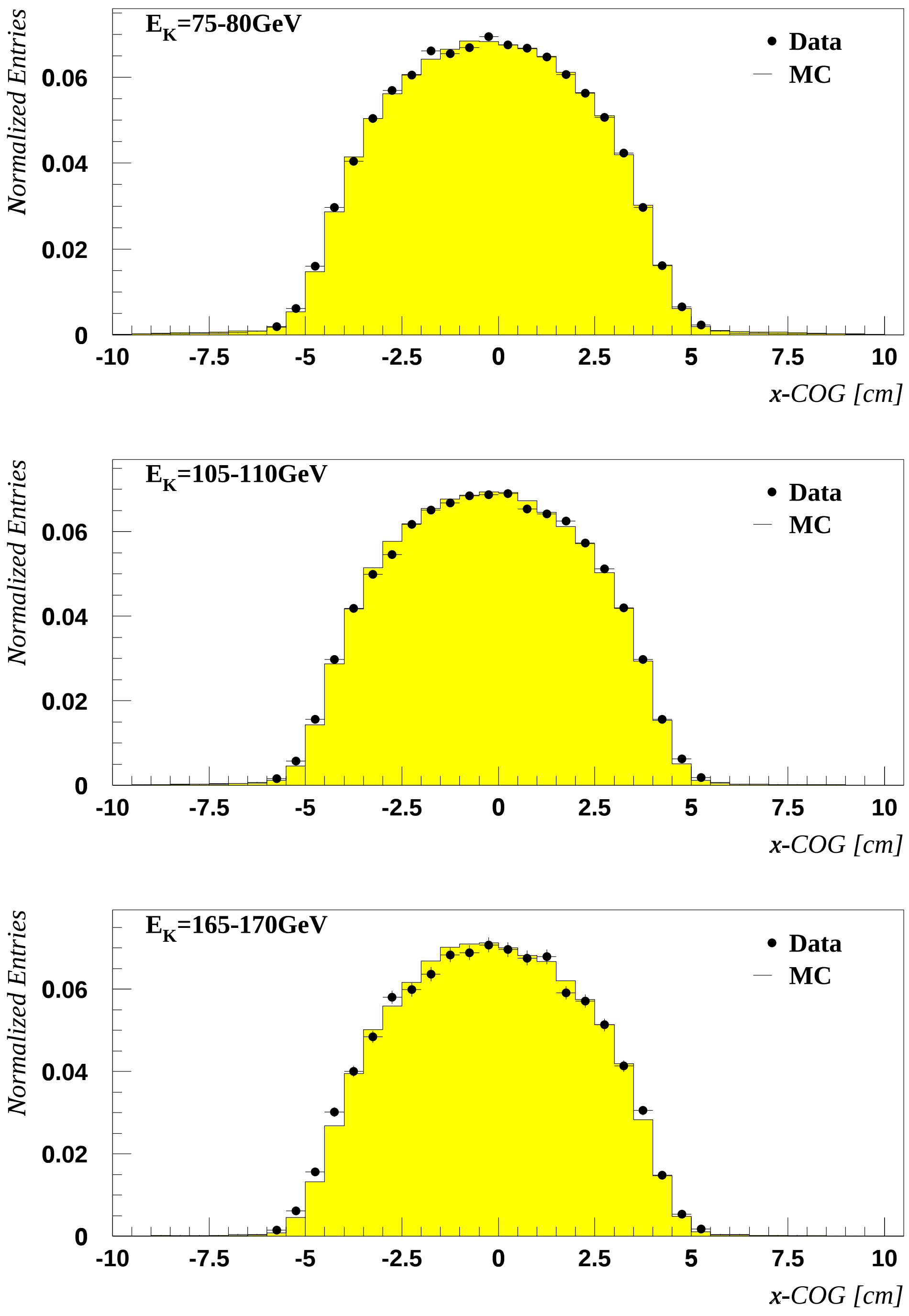

Figure 57: Comparison of the x-projection of the COG for the charged decay mode of K_S.

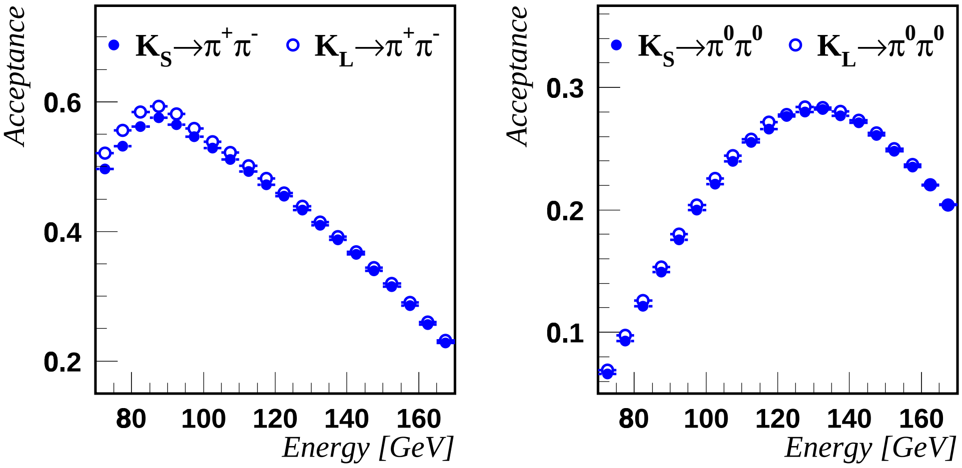

Figure 58: Acceptance for the four decay modes.

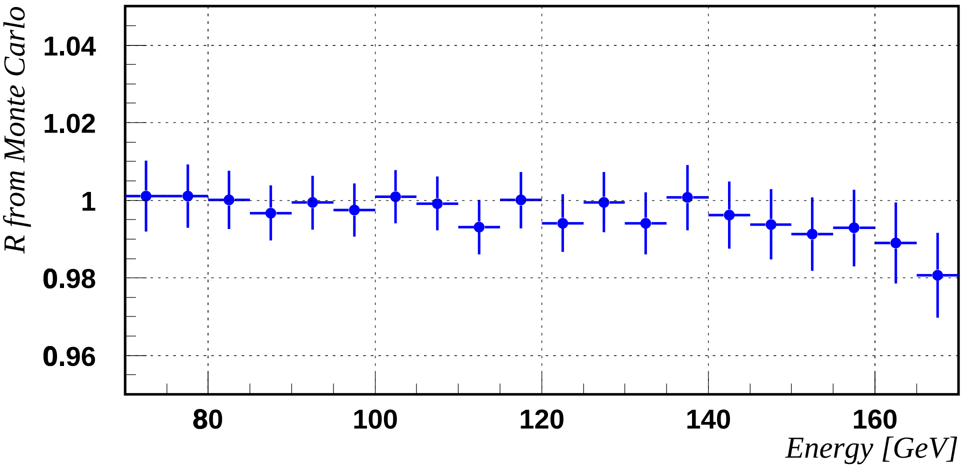

Figure 59: Double ratio R calculated from Monte Carlo events.

The main contribution in the uncertainty comes from the dead column of the LKR, as the acceptance correction becomes sensitive to geometrical variations.

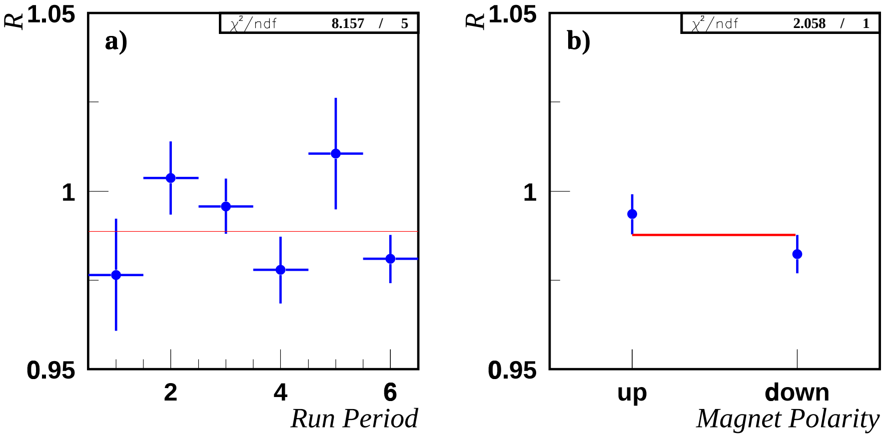

Figure 60: R for different run periods (a) and for both magnet polarities (b).

8.12 Additional Checks on Systematics

In order to investigate possible systematic effects, several checks have been made. Some of the systematic corrections are intensity dependent, for example the tagging dilution and the charged trigger efficiency. Dead-time and accidentals depend on the beam intensity. Unaccounted dead-time and accidentals, which affect K_{S} and K_{L} differently, may show as a dependency of R on the intensity. R is measured as function of the intensity of the beam derived from the K_{L} target and as function of the ratio of the intensity of the two beams. The intensities are measured with the K_{S} Monitor and with the K_{L} Beam Monitor, respectively. For each event the instantaneous K_{L} intensity and the intensity ratio is calculated. Figure 63 shows that there is no dependency of R on the beam intensity.

In order to be able to see effects due to the charged trigger, the data taking has been divided into six periods (Table 13), according to changes in the charged trigger or the magnetic field. The Massbox efficiency over the data taking is discussed in Section 8.5.2. R has been calculated separately for these 6 periods. Figure 61 shows that no systematic effect due to changes in the Massbox or the magnetic field can be seen.

Another possible effect could come from the accumulation of space charge in the LKR calorimeter during the burst. A correction for this effect is applied in the event reconstruction. To exclude any remaining effect, R is calculated for different times within a burst. Figure 62 shows that there is no dependency of R on the time within a burst.

R has also been calculated in the extended energy range from 65 GeV

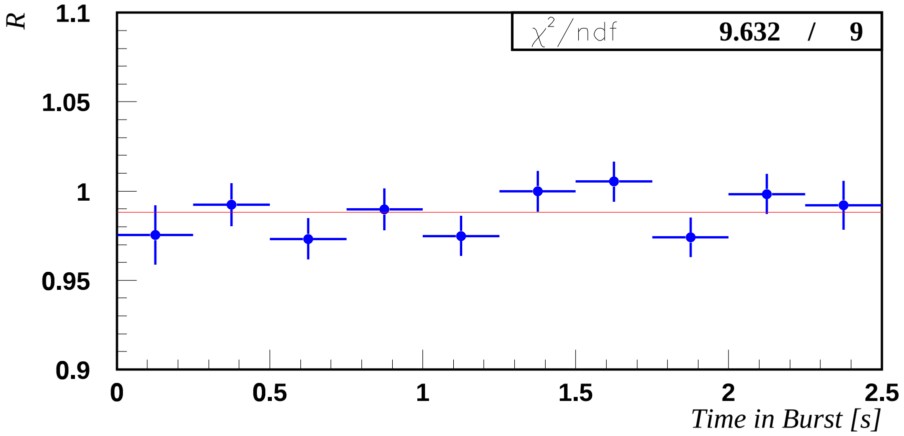

Figure 61: R as function of the time within the burst.

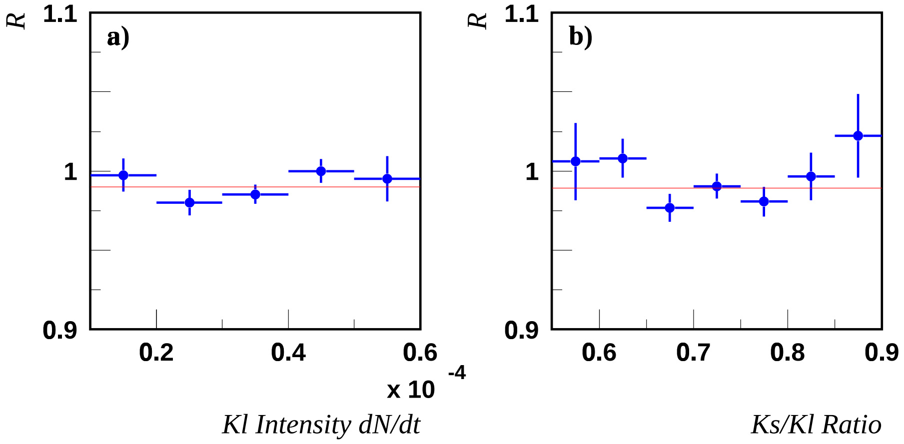

Figure 62: Dependency of R on the beam intensity. a) R as function of the instantaneous intensity measured with the K_L beam monitor. b) R as function of the ratio of the K_S and K_L beam intensity.

to 180 GeV. Figure 64 shows R in the extended area as open circles. These energy bins are more affected by the non-linearity of the LKR and other systematic effects. Therefore the previously defined energy range for the final result of R is not extended. However, these measurements are done to investigate a possible systematic dependency of R on the kaon energy. The data points in the extended region do not support a systematic dependency.

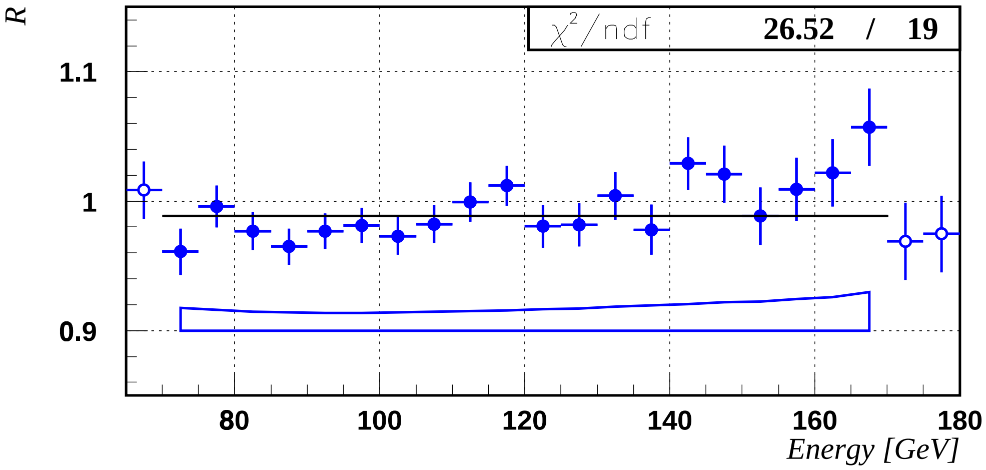

Figure 63: The final value of R per energy bin after all corrections. For the final result the energy interval 70 GeV - 170 GeV is used. The uncertainty in this region is shown as a band. Data points beyond this region are shown as open circles.

9 Result of the Measurement and Comparison with other Experiments

9.1 Result of this Measurement

The dilution correction, the Massbox efficiency correction, the background corrections, and the acceptance correction described in the previous Sections are applied separately for each energy bin. Their effect on the value of R and their uncertainties are summarized in Table 16.

Figure 64 shows R after applying all of the corrections per energy bin. The final result is based on the log-R estimator, combining the 20 measurements in the energy range 70 GeV - 170 GeV:

$$R_{\mathrm{corr}} = 0.9890 \pm 0.0044. \tag{9.1}$$

This translates into the following value of $\mathcal{R}e(\varepsilon'/\varepsilon)$:

$$\begin{aligned} \mathcal{R}e(\varepsilon'/\varepsilon) &= (18.3 \pm 4.6\ (\mathrm{stat}) \pm 5.8\ (\mathrm{sys})) \times 10^{-4}\ , & (9.2) \\ &= (18.3 \pm 7.4) \times 10^{-4}\ (\mathrm{combined}). & (9.3) \end{aligned}$$

Some of the systematic uncertainties are dominated by statistics and can be improved significantly in the future. The main contribution comes from

Corrections and systematic uncertainties on R

Source	Correction $[10^{-4}]$	Uncertainty $[10^{-4}]$	
Tagging $\alpha^{+-}_{\mathrm{L}S}$, $\alpha^{+-}_{\mathrm{S}L}$	+59	0	
Tagging dilution $\Delta\alpha_{\mathrm{L}S}$	+16	9	(stat.)
Tagging efficiency $\Delta\alpha_{\mathrm{S}L}$	0	6	(stat.)
Charged trigger	+11	22	(stat.)
Charged background	+20	5	
Beam scattering	-12	3	
Neutral background	-8	2	
Acceptance	+28	13	(MC stat.)
Accidental activity	-3	16	(stat.)
Reconstruction	-	3	
Energy scale, non linearity	-	12	
Charged vertex	-	5	
All	111	35	(stat.)

Table 16: Summary of the corrections applied to R and their systematic uncertainties. Some of the uncertainties are dominated by statistics.

the charged trigger. Although the Massbox efficiency can be as high as 96%, the average efficiency is 91% due to coincidence problems of the Q_x and E_{tot} trigger signals. The main contribution to the error on the efficiency measurement is statistical in nature. A large sample of down-scaled events is required to measure this efficiency precisely. To improve the situation, the Massbox has been upgraded for the data taking in 1998. The Level 1 Trigger has also been changed to improve the efficiency measurement.

The uncertainty on the measurement due to the effect of accidentals using the overlay technique is limited by the number of events which are overlaid. This procedure is computationally intensive so that only a fraction of events have been overlaid. An upgrade of computing power has allowed us to overlay all the candidate events from the 1998 data taking.

Other uncertainties will improve with increased statistics. The tagging dilution will be measured more precisely in the future.

This measurement is 2.5 standard deviations above 0 and constitutes additional evidence for the existence of direct CP violation. Within errors the result is compatible with Standard Model predictions. The data sample collected in 1997 is only 13% of the total available statistics. Thus the precision of the result will be improved significantly in the future.

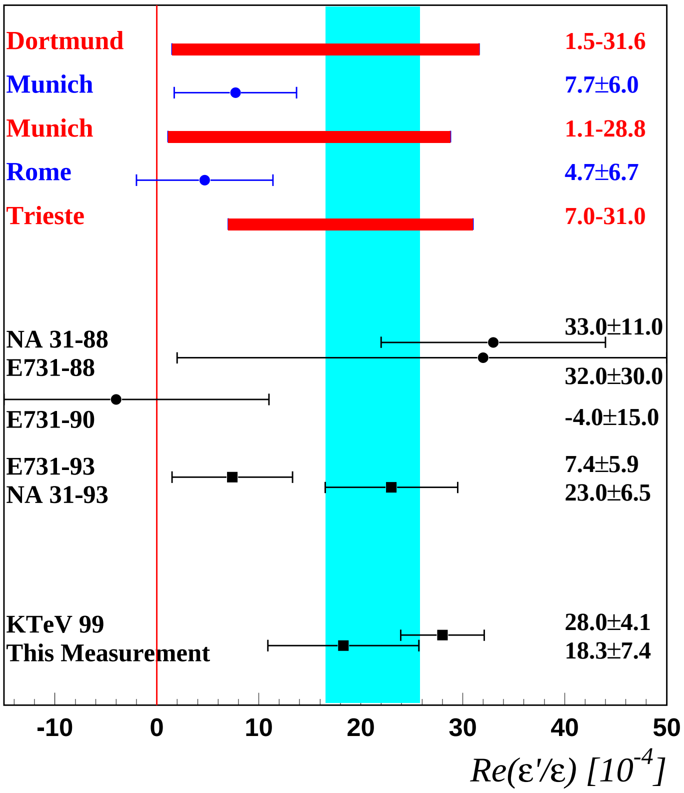

Figure 64: Comparison of the theoretical predictions and the various measurements of ε'/ε. The shaded area marks the grand average $(21.2 \pm 4.7) \times 10^{-4}$ of the four latest experimental results, combined following the description of the Particle Data Group. Theoretical estimates shown as bands are a result of a scanning of the input parameters.

9.2 Comparison with other Results

The first evidence for a non-zero value of $\mathcal{R}e(\varepsilon'/\varepsilon)$ was presented by the NA31 collaboration at CERN in 1988. Their result was $\mathcal{R}e(\varepsilon'/\varepsilon) = (33 \pm 11) \times 10^{-4}$ [B+88]. The Fermilab experiment E731 followed shortly after with the result $\mathcal{R}e(\varepsilon'/\varepsilon) = (32 \pm 30) \times 10^{-4}$ [W+88]. Both experiments published their final results in 1993: E731 found $\mathcal{R}e(\varepsilon'/\varepsilon) = (7.4 \pm 5.9) \times 10^{-4}$ [G+93], which is consistent with zero, whereas NA31 found $\mathcal{R}e(\varepsilon'/\varepsilon) = (23.0 \pm 6.5) \times 10^{-4}$ [B+93]. The latter constitutes clear evidence for direct CP violation with more than 3 standard deviations significance. The successor of the Fermilab experiment, KTeV, published its first result in 1999 [AH+99], this time clearly showing a non-zero value: $\mathcal{R}e(\varepsilon'/\varepsilon) = (28.0 \pm 3.0\ \text{(stat)} \pm 2.8\ \text{(sys)}\ (\pm\ 4.1\ \text{(comb)})) \times 10^{-4}$.

When combining the last three measurements with the result of this analysis, the grand average is $\mathcal{R}e(\varepsilon'/\varepsilon) = (21.2 \pm 2.8) \times 10^{-4}$. As the χ^2 per degree of freedom is 2.81, one may follow the procedure of the Particle Data Group and scale the errors of the single measurements by a factor of 1.68. The grand average then becomes:

$$\mathcal{R}e(\varepsilon'/\varepsilon) = (21.2 \pm 4.7) \times 10^{-4}. \tag{9.4}$$

The grand average is only in agreement with theoretical predictions when all of the input parameters are simultaneously close to their allowed limits. This is illustrated by the bands in Figure 65. When central values are used, the theoretical predictions are hardly in agreement with the experimental result.

The new measurements of $\mathcal{R}e(\varepsilon'/\varepsilon)$ have prompted some suggestions to improve the theoretical calculations. The Dortmund group sees an enhancement of ε'/ε, when investigating contributions of order $\mathcal{O}(p^2/N_c)$ to the operator Q_6 within the chiral expansion [HKPS99, HKPS00]. Combining results obtained with 3 different sets of Wilson coefficients (LO+NDR+HV), and using central values of the input parameters, they obtain $7.0 \times 10^{-4} < \varepsilon'/\varepsilon < 19.4 \times 10^{-4}$ assuming zero phases for the final state interactions. When they use phenomenological values for the phases of the final state interactions, they obtain $9.3 \times 10^{-4} < \varepsilon'/\varepsilon < 24.7 \times 10^{-4}$.

Effects of final rescattering of the two pions, which may enhance ε'/ε, have been discussed [PP99]. In [EMNP99] an enhancement of ε'/ε due to isospin breaking is proposed. The authors estimate contributions of $\pi^0 - \eta$ mixing in $\mathcal{O}(p^4)$ in χPT. Taking both effects together, an enhancement of the theoretical prediction of ε'/ε by a factor of 2.3 is obtained [EMNP99]. One of the assumptions used to calculate the dispersive correction factors is critisized in [BCF$^+$00]. Final state rescattering effects using a dispersion integral have also been studied in [Pas99]. Isospin breaking is also discussed in [GV99].

Possible contributions to ε'/ε from New Physics beyond the Standard Model are summarized in [Nie99]. Many of the alternative models contain new phases, which can lead to CP violating effects and to an enhancement of ε'/ε.

Improvements in the theoretical calculations of ε'/ε and more precise measurements of KTeV, DAΦNE, and NA48 can hopefully contribute to a better understanding of CP violation in nature.

A Appendix

A.1 Derivation of the Formula for the Dilution Difference

A more detailed look into the tagging dilution effects is given in [Cré98]. For this purpose we distinguish two samples:

1. A sample containing only events without accidental hit in the Tagger, thus only K_L decays which are tagged correctly. Quantities related to this sample have the index *tag*.

2. A K_L sample identified by the vertex tag containing only K_L events with accidental proton hit in the Tagger, thus containing the misidentified events. Quantities referring to this sample are indexed with *mis*.

We now define the following quantities:

α_tag	Probability of a proton hit from the window method with the sample of correctly tagged K_L.
α_mis	Probability of a proton hit from the window method with the sample containing only mis-tagged K_L.
P_W	Probability of a proton hit in window W for true K_L events (the tagged and mis-tagged sample). Therefore we have $P_W^{+-} = \alpha_{\mathrm{L}S}^{+-}$.
$P_{\overline{W}}$	Probability of a proton hit in a shifted tagging window $\overline{W}$ fort true K_L events.

Using the difference $d_{W\overline{W}}^{+-} = P_W^{+-} - P_{\overline{W}}^{+-}$ we get:

$$\alpha_{\mathrm{L}S}^{+-} = P_W^{+-} = P_{\overline{W}}^{+-} + d_{W\overline{W}}^{+-}. \tag{A.1}$$

We can now express the probability for a proton hit in the true K_L sample $P_{\overline{W}}^{+-}$ as sum of the probabilities in the tagged and in the mis-tagged subsample. For this we use $\alpha_{\mathrm{L}S}^{+-}$, which is the fraction of mis-tagged events:

$$P_{\overline{W}}^{+-} = (1 - \alpha_{\mathrm{L}S}^{+-})\alpha_\mathrm{tag}^{+-} + \alpha_{\mathrm{L}S}^{+-} P_\mathrm{mis}^{+-} \tag{A.2}$$

Using this relation we get from equation (A.1):

$$\alpha_{\mathrm{L}S}^{+-} = (1 - \alpha_{\mathrm{L}S}^{+-})\alpha_\mathrm{tag}^{+-} + \alpha_{\mathrm{L}S}^{+-} P_\mathrm{mis}^{+-} + d_{W\overline{W}}^{+-}. \tag{A.3}$$

We get the same equation for α_{LS}^{00} by changing the indices '$+-$' to '00'. Using $\Delta_{\mathrm{tag}} = \alpha_{\mathrm{tag}}^{00} - \alpha_{\mathrm{tag}}^{+-}$ and $\Delta_{\mathrm{mis}} = \alpha_{\mathrm{mis}}^{00} - \alpha_{\mathrm{mis}}^{+-}$ this results to:

$$\alpha_{\mathrm{L}S}^{00} = (1 - \alpha_{\mathrm{L}S}^{00})(\alpha_{\mathrm{tag}}^{+-} + \Delta_{\mathrm{tag}}) + (P_{\mathrm{mis}}^{+-} + \Delta_{\mathrm{mis}})\alpha_{\mathrm{L}S}^{00} + d_{W\overline{W}}^{00}. \tag{A.4}$$

Therefore we get for the difference

$$\Delta\alpha_{\mathrm{L}S} = \alpha_{\mathrm{L}S}^{00} - \alpha_{\mathrm{L}S}^{+-} \tag{A.5}$$

$$= \frac{1}{1 - P_{\mathrm{mis}}^{+-} + \alpha_{\mathrm{tag}}^{+-}} \times (\Delta_{\mathrm{tag}} + \alpha_{\mathrm{L}S}^{00}(\Delta_{\mathrm{mis}} - \Delta_{\mathrm{tag}}) + (d_{W\overline{W}}^{00} - d_{W\overline{W}}^{+-})). \tag{A.6}$$

In principle the terms $\alpha_{\mathrm{L}S}^{00}(\Delta_{\mathrm{mis}} - \Delta_{\mathrm{tag}})$ and $d_{W\overline{W}}^{00} - d_{W\overline{W}}^{+-}$ are very small. A measurement [IF98] gave the result:

$$\alpha_{\mathrm{L}S}^{00}(\Delta_{\mathrm{mis}} - \Delta_{\mathrm{tag}}) < (3 \pm 1) \times 10^{-4}, \tag{A.7}$$

$$d_{W\overline{W}}^{00} - d_{W\overline{W}}^{+-} = (3 \pm 4) \times 10^{-4}. \tag{A.8}$$

As both terms are consistent with zero, they are neglected in this analysis. This leaves:

$$\Delta\alpha_{\mathrm{L}S} = \alpha_{\mathrm{L}S}^{00} - \alpha_{\mathrm{L}S}^{+-} = \frac{\Delta_{\mathrm{tag}}}{1 - P_{\mathrm{mis}}^{+-} + \alpha_{\mathrm{tag}}^{+-}}, \tag{A.9}$$

with $P_{\mathrm{mis}}^{+-} = 0.1386$ and $\alpha_{\mathrm{tag}}^{+-} = 0.10507$.

References

[A$^+$80] H. W. Atherton et al. Precise Measurements of Particle Production by 400 GeV/c Protons on Beryllium Targets. Technical report, Cern Yellow Report 80-07, 1980.

[A$^+$98] S. Anvar et al. The charged trigger system of NA48 at CERN. *Nucl. Instr. Meth.*, A 419:686–694, 1998.

[AH$^+$99] A. Alavi-Harati et al. Observation of direct CP violation in $K_{\mathrm{S,L}} \to \pi\pi$ decays. *Phys. Rev. Lett.*, 83:22, 1999.

[AM98] R. Arcidiacono and E. Menichetti. The Level 1 Trigger Supervisor: past, present and future. Technical report, NA48 Note 98-11, 1998.

[Arc99] R. Arcidiacono. *Systematic effects on ε'/ε in the NA48 experiment at CERN: trigger efficiencies and correction due to accidentals.* PhD thesis, Dip. di Fisica Sperimentale, Univ. di Torino, 1999.

[B$^+$88] H. Burkhardt et al. First evidence for direct CP violation. *Phys. Lett.*, pages 169–176, 1988.

[B$^+$93] G. D. Barr et al. A New measurement of direct CP violation in the neutral kaon system. *Phys. Lett.*, B317:233–242, 1993.

[B$^+$96] G.D. Barr et al. Performance of an electromagnetic liquid krypton calorimeter based on a ribbon electrode tower structure. *Nucl. Instr. Meth.*, A 370:413–424, 1996.

[BBG$^+$99] S. Bosch, A.J. Buras, M. Gorbahn, S.Jäger, M. Jamin, M.E. Lautenbacher, and L. Silvestrini. Standard model confronting new results for ε'/ε. *hep-ph/9904408*, 1999.

[BCF$^+$00] A.J. Buras, M. Ciuchini, E. Franco, G. Isidori, G. Martinelli, and L. Silvestrini. Final State Interactions and ε'/ε: A Critical Look. *hep-ph/0002116*, 2000.

[BCLM97] A. Bizzeti, M. Calvetti, M. Lenti, and A. Michetti. The NA48 K_{S} Monitor. Technical report, NA48 Note 97-29, 1997.

[BDG$^+$98] C. Biino, N. Doble, L. Gatignon, P. Grafström, and H. Wahl. The simultaneous long- and short-lived neutral Kaon Beams for Experiment NA48. *NA48 Note 98-16*, 1998.

[Ber97a] J. Bernabeu. CP-violation. *hep-ph/9706345*, 1997.

[Ber97b] I. Bertanza, et al. (NA31 Coll.). Measurement of the K_S mean lifetime from $\pi^+\pi^-$ and $\pi^0\pi^0$ decays using K_L decays to determine the acceptance. *Z. Phys.*, C 73:629–632, 1997. D(p) has been determined by the NA31 collaboration under similar conditions. See this paper and references therein.

[BFE98] S. Bertolini, M. Fabbrichesi, and J.O. Eeg. Estimating ε'/ε. A review. *hep-ph/9802405*, 1998.

[Bii99] C. Biino. Technical report, Collaboration Meeting July 1998 and Contribution to the private news group from January 28th, 1999.

[Blü95] H. Blümer. The NA48 Beam Intensity Monitor - Status Report from 1994. Technical report, NA48 Note 95-08, 1995.

[Buc97] G. Buchalla. CP violation in K and B decays. *hep-ph/9707545*, 1997.

[Bur99] A.J. Buras. Theoretical status of ε'/ε. *hep-ph/9908395*, 1999. Kaon 99, Chicago.

[C+97a] P. Cenci et al. The charged Pretrigger System. Technical report, NA48 Note 97-26, 1997.

[C+97b] P. Cenci et al. The Fast Logic of Charged and Neutral hodoscopes. Technical report, NA48 Note 97-25, 1997.

[CCFT64] J.H. Christenson, J.W. Cronin, V.L. Fitch, and R. Turlay. Evidence for the 2π decay of the K_2^0 meson. *Phys. Rev. Lett.*, 13:138–140, 1964.

[Cha83] L.-L. Chau. Quark mixing in weak interactions. *Phys. Rep.*, 95:1, 1983.

[Cré98] S. Crépé. *Mesure du Temps des Désintégrations $K \rightarrow \pi^0\pi^0$ et Etiquetage des K_L et des K_S dans l'Expérience NA48 au CERN.* PhD thesis, Université Joseph Fourier de Grenoble, 1998.

[DGdC98] P. Debu and R. Granier de Cassagnac. 1997 Charged Trigger Efficiency. Technical report, NA48 Note 98-8, 1998.

[DGG96] N. Doble, L. Gatignon, and P. Grafstrom. A novel application of bent crystal channeling to the production of simultaneous particle beams. *Nucl. Instr. Meth.*, B119:181, 1996.

[DH96] P. Debu and P. Hristov. Mass Box Studies. Technical report, NA48 Note 96-6, 1996.

[EMNP99] G. Ecker, G. Müller, H. Neufeld, and A. Pich. $\pi^0 - \eta$ Mixing and CP Violation. *hep-ph/9912264*, 1999.

[F^+99] V. Fanti et al. A new measurement of direct CP violation in two pion decays of the neutral kaon. *Phys. Lett.*, B465:335, 1999.

[FC98] Gary J. Feldman and Robert D. Cousins. A unified approach to the classical statistical analysis of small signals. *Phys. Rev.*, D57:3873–3889, 1998.

[FHK^+98] H. Fox, K. Holtz, L. Köpke, S. Schmidt, and Y. Schue. Filter Cuts and Configuration for Reprocessing 1997 and 1998. Technical report, NA48 Note 98-28, 1998.

[Fis98] Günther Fischer. *Implementation, Calibration and Performance-analysis of a novel Trigger for $K^0 \rightarrow 2\pi^0$ of the NA48 CP-violation experiment.* PhD thesis, Institut für Kernphysik, Technische Universität Wien, 1998.

[G^+93] L. K. Gibbons et al. Measurement of the CP violation parameter $\mathcal{R}e(\varepsilon'/\varepsilon)$. *Phys. Rev. Lett.*, 70:1203–1206, 1993.

[Giu99] S. Giudici. LKR Energy Scale 1997. Technical report, NA48 Note 99-16, 1999.

[GKR99] F.J. Gilman, K. Kleinknecht, and B. Renk. The Cabibbo-Kobayashi-Maskawa mixing matrix. In PDG [PDG98]. Particle Data Group.

[Gor99] B. Gorini. *Measurement of $\mathcal{R}e(\varepsilon'/\varepsilon)$ with a new calorimetry technique.* PhD thesis, Scuola Normale Superiore, Pisa, Italy, 1999.

[Gra99] G. Graziani. *Measurement of direct CP violation with the NA48 experiment at CERN.* PhD thesis, Universita degli studi di Firenze, Italy, 1999.

[GV99] S. Gardner and G. Valencia. Additional Isospin-Breaking Effects in ε'/ε. *hep-ph/9909202*, 1999.

[H^+98] B. Hallgren et al. The NA48 LKr calorimeter digitizer electronics chain. *Nucl. Inst. Meth.*, A 419:680–685, 1998.

[Hay96] B. Hay. *Determination of the Branching Ratio* $K_{\mathrm{L}} \to \pi\mu\nu / K_{\mathrm{L}} \to \pi e\nu$ *and a Study of* $K_{\mathrm{L}} \to \pi^+\pi^-\pi^0 / K_{\mathrm{L}} \to$ *all charged.* PhD thesis, University of Edinburgh, Great Britain, 1996.

[HKPS99] T. Hambye, G.O. Köhler, E.A. Paschos, and P.H. Soldan. Analysis of ε'/ε in the $1/N_c$ expansion. *hep-ph/9906434*, 1999.

[HKPS00] T. Hambye, G.O. Köhler, E.A. Paschos, and P.H. Soldan. Analyzing ε'/ε in the $1/N_c$ expansion. *hep-ph/0001088*, 2000.

[IF98] L. Iconomidou-Fayard. Technical report, NA48 analysis meeting, October 5th, 1998.

[Kle76] K. Kleinknecht. CP violation and K^0 decays. *Ann. Rev. Nucl. Part. Sci.*, 26:1, 1976.

[Kle89] K. Kleinknecht. CP Violation in the K^0 anti-K^0 System. In C. Jarlskog, editor, *CP Violation*, pages 41–104. World Scientific, 1989.

[KM73] M. Kobayashi and T. Maskawa. CP-violation in the renormalizable theory of weak interaction. *Prog. Theor. Phys.*, 49:652–657, 1973.

[Len99] M. Lenti. Neutral Tagging Efficiency in 97 Data: An Alternative Way. Technical report, NA48 Note 99-03, 1999.

[Lüd57] G. Lüders. *Ann. Phys.*, 2, 1957.

[LY56] T. D. Lee and C. N. Yang. Question of Parity Conservation in Weak Interactions. *Phys. Rev.*, 104:254–256, 1956.

[Mar99] G. Martinelli. $\mathcal{R}e(\varepsilon'/\varepsilon)$ from Rome 1999. *http://hep.uchicago.edu/kaon99/talks/martinelli/*, 1999. Talk given at Kaon 99, Chicago.

[Mas94] A. Masiero. CP violation for pedestrians. In *European School of High-energy Physics Zakopane, DFPD 94 TH 16*, 1994.

[MWS99] I. Mikulec and I. Wingerter-Seez. 1997 and 1998 $\mathcal{R}e(\varepsilon'/\varepsilon)$ compact filters run at CERN. Technical report, NA48 Note 99-24, 1999.

[Nie99] U. Nierste. Theoretical status of ε'/ε. *hep-ph/9910257*, 1999.

[Pal96] Sandro Palestini. An Electromagnetic Calorimeter Based on Liquid Krypton with Tower Read-Out Structure. Technical report, NA48 Note 96-24, 1996. Presented at the *1996 IEEE Nuclear Science Symposium.*

[Par98] Helen Parsons. *A Study of the CP Violation Parameter ε'/ε*. PhD thesis, University of Edinburgh, 1998.

[Pas99] E.A. Paschos. Rescattering Effects for $(\varepsilon'/\varepsilon)$. *hep-ph/9912230*, 1999.

[Pau55] W. Pauli. Niels bohr and the development of physics. *McGraw Hill*, 1955.

[PDG98] Review of Particle Physics. *Eur. Phys. J. C*, 3, 1998. Particle Data Group.

[PP99] E. Pallante and A. Pich. Strong Enhancement of ε'/ε Through Final State Interactions. *hep-ph/9911233*, 1999.

[Sak67] A. D. Sakharov. Violation of CP invariance, C asymmetry, and baryon asymmetry of the universe. *Pisma Zh. Eksp. Teor. Fiz.*, 5:32–35, 1967.

[Sch96] V. Schönharting. NMC Users Guide. Technical report, NA48 Note 96-17, 1996.

[Una95] G. Unal. Neutral Reconstruction. Technical report, NA48 Note 95-10, 1995.

[Una98] G. Unal. Reconstruction program for the Lkr. Technical report, NA48 Note 98-1, 1998.

[Vat98] D. Vattolo. Neutral Tagging Efficiency With 1997 Data. Technical report, NA48 Note 98-07, 1998.

[W$^+$88] M. Woods et al. First Result on a New Measurement of ε'/ε in the Neutral Kaon System. *Phys. Rev. Lett.*, 60:1695, 1988.

[WAH$^+$57] C. S. Wu, E. Ambler, R. W. Hayward, D. D. Hoppes, and R. P. Hudson. Experimental Test of Parity Conservation in β Decay. *Phys. Rev.*, 105:1413, 1957.

[Wol64] L. Wolfenstein. Violation of CP invariance and the possibility of very weak interactions. *Phys. Rev. Lett.*, 13:562–564, 1964.

[Wol83] Lincoln Wolfenstein. Parametrization of the Kobayashi-Maskawa matrix. *Phys. Rev. Lett.*, 51:1945, 1983.

[WW93] Bruce Winstein and Lincoln Wolfenstein. The Search for direct CP violation. *Rev. Mod. Phys.*, 65:1113–1148, 1993.

List of Figures

List of Tables

Acknowledgements

I wish to thank Prof. L. Köpke, who was always open for discussions and a source of valuable information. Prof. K. Kleinknecht made this work possible. I am especially indebted to him for the possibility to participate at the Summer School Ustron 99, which was a great experience.

The work together with Dr. M. Velasco was very impressing. She seemed to have an endless resource of energy and Coke-Light. I also want to thank the rest of the colleagues at CERN, with whom I worked closely together: Dr. B. Gorini, V. Martin, and T. Gershon.

I owe many thanks to the team of the Level 3: Dr. M. Sozzi, Dr. P. Calafiura, Prof. L. Köpke, S. Schmidt, Y. Schue and K. Holtz. Dr. B. Panzer-Steindel and G. Wirrer from the Central Data Recording were always willing to solve our problems during data taking - day and night. Working with them on the 'online' software was a great plesure. I had also very fruitful discussions with Dr. S. Luitz and M. Wittgen, who took care of the data acquisition.

S. Hohmann helped me a lot with all administrational matters, as well as K.-H. Geib with all technical problems. I also thank R. Casper for his immediate help.

Life at CERN would have been much less interesting without the colleagues and friends I shared my house and my spare time with: G. Dell, M. Eppard, R. Hofmann, K. Holtz, A. Peters, Y. Schue, A. Winhart, and M. Wittgen. I would also like to mention A. Huber, Dr. A. Kalter, Dr. U. Koch, V. Martin, O. Melzer, I. Pellmann, Dr. M. Velasco. I learned a lot (not only about cooking) from Dr. G. Fischer and Dr. S. Luitz.